NASA Contractor Report 4309

# Free Wake Analysis of Hover Performance Using a New Influence Coefficient Method

Todd R. Quackenbush, Donald B. Bliss,
Daniel A. Wachspress, and Ching Cho Ong

CONTRACT NAS2-12148
JULY 1990



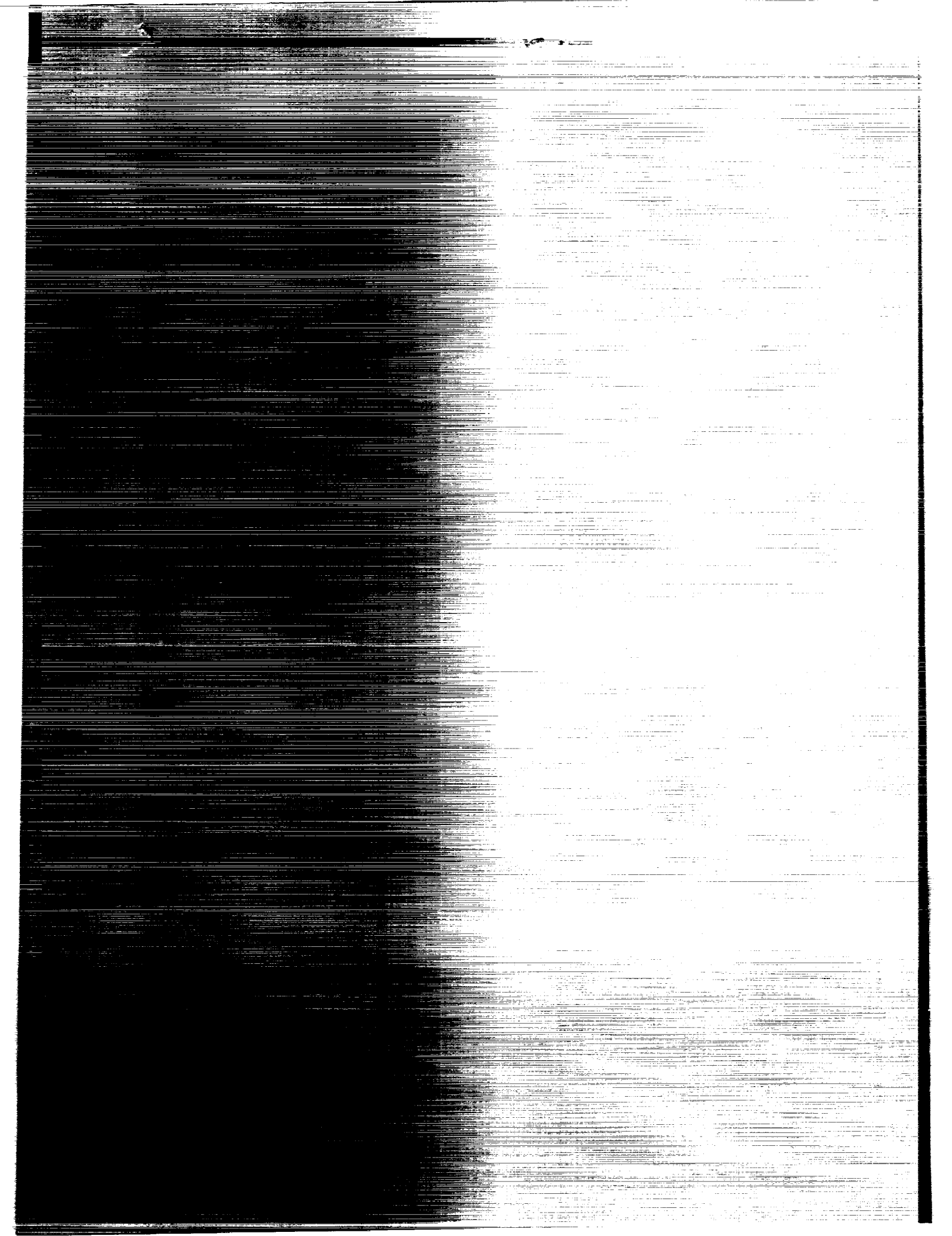

NASA Contractor Report 4309

# Free Wake Analysis of Hover Performance Using a New Influence Coefficient Method

Todd R. Quackenbush, Donald B. Bliss,
Daniel A. Wachspress, and Ching Cho Ong
*Continuum Dynamics, Inc.*
*Princeton, New Jersey*

Prepared for
Ames Research Center
under Contract NAS2-12148

National Aeronautics and
Space Administration
Office of Management
Scientific and Technical
Information Division

**1990**

TABLE OF CONTENTS

TABLE OF CONTENTS (Cont'd)

## Acknowledgments

The authors would like to thank Mr. Fort F. Felker of NASA Ames Research Center, Technical Monitor for this effort, for his help in supplying data to support the correlation studies performed herein. Similar thanks are due to Dr. D.R. Poling and Mr. H. Rosenstein of the Boeing Vertol Company.

## SUMMARY

A novel free wake method for evaluating the performance of helicopter rotors in hover and axial flight is described. The new method features a wake relaxation scheme using influence coefficients and has been incorporated in a performance prediction program known as EHPIC (Evaluation of Hover Performance using Influence Coefficients). This new approach avoids the convergence problems associated with previous time-stepping analyses. Several model problems are presented that show excellent correlation with experimental performance data and also demonstrate the flexibility of the method.

# 1. INTRODUCTION AND BASIC PRINCIPLES

## 1.1 A New Approach to the Hover Problem

The determination of the wake of a hovering rotor poses a particularly challenging computational problem. Numerical solutions for the free wake of a hovering rotor (Refs. 1-5) have experienced stability and convergence problems. The instability encountered causes the wake to depart from an idealized, smoothly contracting helical form. Reference 1 describes the instability in some detail, noting that it is characterized by a tendency of wake turns beyond the extreme near wake to distort and orbit one another. The same behavior is also described in Ref. 4, and was even encountered using the significantly different computational method in Ref. 5. This behavior leads to residual unsteadiness in the downwash velocity at the rotor blade, and if left unchecked this instability may lead to uncontrollable divergence of the solution.

The fundamental difficulty lies in the fact that the wake of a hovering rotor actually is unstable, as is also confirmed by experiment. The instability can be viewed as the first step in the evolution from an orderly flow structure near the rotor to a turbulent jet far below. The common feature of the free wake hover analyses cited above is that they seek to find the solution through time marching schemes. Starting with an incorrect initial wake configuration, the subsequent wake motion is computed in the hope that it will progress to the desired hover solution. However, because of the wake instability, it is not possible to obtain an equilibrium solution for the wake structure using a time marching approach. Thus, the computed wake should not be expected to completely settle down. In fact, numerical simulations often seem to exhibit a greater degree of instability than the physical reality, probably due to the finite size of the free wake. The quality of the solution may actually deteriorate over time.

Researchers have tried to circumvent this stability problem by artificial suppression of the instability. Methods of suppression include periodically smoothing and imposing symmetry on the wake, and the introduction of substantial amounts of numerical damping. Unfortunately, such approaches may effectively impose forces on the wake, leaving open the question of whether equilibrium free motion conditions are really being satisfied. Depending on the type of suppression used, long computer run times may still be required to obtain convergence or to compute time-averaged results if some residual instability remains.

In order to circumvent the limitations of the traditional approach, a new method for finding solutions to the hover problem was proposed several years ago (Ref. 6). The new method avoids the difficulties just described and offers a number of advantages. This new approach is based on the proposition that the free wake hover problem possesses a self-preserving steady solution when viewed in blade fixed coordinates. A self-preserving steady vortex flow is one in which the velocity the vorticity field induces on itself exactly preserves the shape of the vorticity field. Viewed in an appropriate

coordinate frame, the solution appears steady and unchanging. In the case of the hover problem, the appropriate reference frame is fixed to the rotating blades.

The self-preservation property of this ideal solution is not to be confused with its stability; in fact it has been demonstrated to be unstable. Nevertheless, the average aerodynamic properties of a hovering rotor can be obtained from this ideal steady solution. It is this solution about which the wake instability develops. Because of the wake instability, the desired solution cannot be found by the usual time marching approach. However, as described later, the solution can be found by an influence coefficient method which does not involve temporal evolution, and can be used even though the solution itself is unstable.

Previous work (Ref. 6) demonstrates the new solution method for a simple tip vortex wake trailed from blades with prescribed circulation. The present report deals with the application of this method to the development of a complete analysis of the full-span hover wake coupled to a blade aerodynamics analysis. The resulting code is capable of predicting the aerodynamic performance of rotor configurations and, as will be seen, gives excellent agreement with experimental data for a variety of rotors.

Before embarking on a detailed description of this code, it should be noted that Appendix A includes a discussion of instructive model problems that may provide useful preliminary information on the analysis method used here. The examples shown there illustrate the use of relaxation methods to find self-preserving solutions for vortex-dominated flows that are similar in many respects to the hovering rotor problems to be discussed below.

## 1.2 The Influence Coefficient Solution Method

The wake of a hovering rotor possesses a self-preserving solution when viewed in a coordinate system rotating with the blade. This solution for a wake composed of a single tip vortex is sketched in Figure 1. In this case, the bound and shed vorticity, plus the background rotating field, induce velocity components along the free wake that exactly preserve its shape. In the rotating frame this ideal solution remains stationary in the absence of disturbances to the flow. As stated earlier, a time marching numerical scheme cannot be used to find this solution because it is unstable. In fact, Ref. 5 used a time dependent scheme in the rotating reference frame and encountered the usual wake instability also sketched in Figure 1. This wake instability develops about the steady self-preserving solution and it is really from this standpoint that the instability should be studied.

It is important to find the ideal steady solution, not only to improve the fundamental understanding of the fluid mechanics of rotor wakes, but also because this solution can be used to predict the steady performance of a hovering rotor. The development of an instability in the contracting helical wake below the rotor involves the vortex turns undergoing motions around the ideal solution. These motions are of secondary importance for the prediction

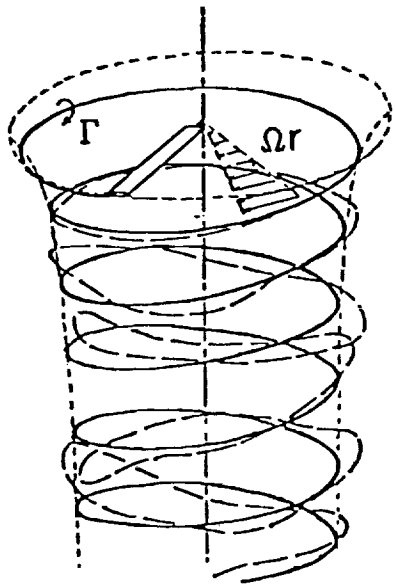


Figure 1. Ideal rotor wake solution (solid line) versus typical wake instability (dashed line).

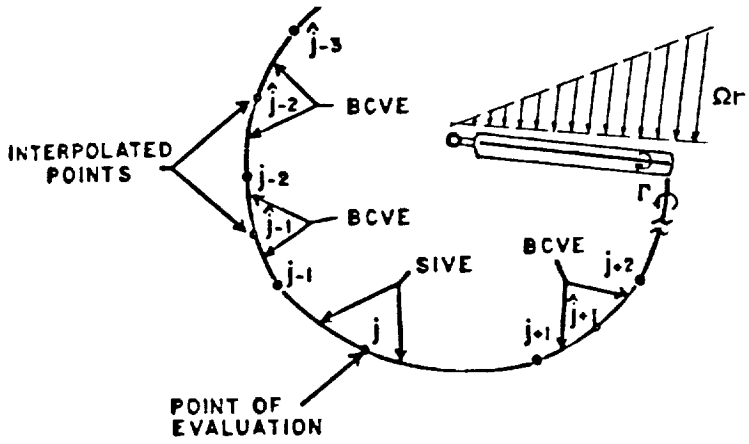


Figure 2. Typical arrangement of elements to calculate the velocity at a point in the wake.

of average performance characteristics, even though they have been a major impediment to previous calculation schemes. It is the possibility of finding an ideal self-preserving solution that allows the hover problem to be approached from a new point of view.

From the standpoint of performance prediction, the problem is to find the wake solution which is self-preserving and stationary in blade fixed coordinates. This requires that the appropriate equilibrium conditions be satisfied by the self-preserving steady wake solution. At each point in the wake, the velocity contributions due to all effects must be such that there is no convection to change the wake shape. For each trailed vortex filament, the net velocity contributions must be such that the velocity at each point is locally tangent to the vortex filament curve. Any velocity component in a plane normal to the filament curve would convect the vortex to a new position, thereby changing the filament shape. The desired solution can be obtained by a mathematical procedure which requires that each vortex filament satisfy the condition that the wake shape be self-preserving.

In practice, the solution must be obtained numerically which means that the wake must be modelled using discrete vortex elements, just as in a traditional free wake analysis. The tip vortex location is defined by a set of collocation points which connect the vortex elements. The wake shape is modified by changing the locations of these points. To find the desired solution, it is necessary to locate the collocation points so that the net velocity vector at each point is tangent to the vortex filament curve passing through this point.

The vortex induced velocity field is obtained by evaluating the Biot-Savart integral over both the vortex wake and the bound circulation on the blades. To model the wake, the curved vortex elements described in Refs. 5-7 are used. Actually, two types of curved elements are required. The Basic Curved Vortex Element (BCVE) is used to evaluate the velocity contribution at any point in the flow field not on the element itself (traditionally, straight-line elements have been used for this purpose). The Self-Induction Vortex Element (SIVE) is used to evaluate the velocity induced by a vortex on itself. Figure 2 shows how these two types of curved elements are used to represent a filament. The relatively smooth, closely spaced curves that describe the vortex shapes in hover are ideally suited for the use of curved elements. Furthermore, different size elements can be used together without discontinuities, thereby providing different degrees of resolution in different parts of the wake (see Section 3.2).

The BCVE is a parabolic arc element positioned between collocation points. The element orientation and curvature are established by requiring that it also pass through an interpolated point located between the collocation points. The interpolated point is determined from the positions of adjacent collocation points. The SIVE is a circular arc element passed through each group of three adjacent collocation points. This element determines the self-induced velocity at the middle collocation point. Once every wake filament has been modelled by vortex elements, the velocity induced at each collocation point, and at any other desired location, can be calculated.

From a given set of collocation point locations for each filament the local tangent, normal, and binormal vectors at each collocation point are determined. These vectors are derived from helical arcs passed through each set of three points. As mentioned, the desired solution is reached when the total velocity vector is tangent to the wake curve at every collocation point. This total velocity vector at any point includes the local self-induction effect (SIVE), the contributions from the rest of the wake (BCVE's), the velocity induced by the bound circulation on the rotor blades, and the swirl velocity component associated with the rotating coordinate system. The local normal and binormal vectors can be used to define a crossflow plane at each collocation point, as shown in Figure 3. If the total velocity at any point has a component in its crossflow plane, then the solution cannot be steady, since the vortex filament would then be convected in the crossflow plane.

The description of the wake in a rotating frame, with vortex displacements being described in local crossflow planes, differs significantly from the usual purely Lagrangian description of the collocation point locations in a stationary frame. It is useful to think of the calculation as taking place in curvilinear coordinates defined by the instantaneous wake shape. The locations of the collocation points form a computational mesh along the vortex filament, and thus the wake description is essentially Eulerian along the arc length. Only the displacements of the wake in the crossflow planes can be viewed as Lagrangian. In this coordinate frame the collocation points do not always represent the same vortical material, which is continually being swept down the filament by the background rotating velocity field. The collocation points simply mark the current position of the filament curve. It is also important to understand, as is generally true in curvilinear coordinates, that displacing the collocation points in the crossflow planes causes the positions and orientations of the planes themselves to change. This effect must also be accounted for when doing calculations in local crossflow coordinates.

The solution procedure, which involves a way to systematically reduce the crossflow velocity to zero at every collocation point, can now be described. Assume for the moment that the strength and location of each filament leaving the blade is held fixed; the coupling to the blade aerodynamics will be described later once the wake treatment is understood.

The effect of small displacements of each collocation point on the velocity at every other collocation point, and the displaced point itself, is first determined. For example, for a small displacement of the jth point in the local binormal direction, the resulting small velocity changes in the normal and binormal directions of every point (including point $j$) are computed. For sufficiently small displacements the effect is essentially linear, and a proportionality constant, or influence coefficient, relating each velocity perturbation to the displacement can be calculated. This process is repeated for the displacement of point $j$ in the local normal direction. The effect of any small displacements of point $j$ in the local crossflow plane can then be calculated at every other point. After repeating this process for all free wake points ($1 \leq j \leq N$) in both the normal and binormal directions, the effect of arbitrarily small displacements of every

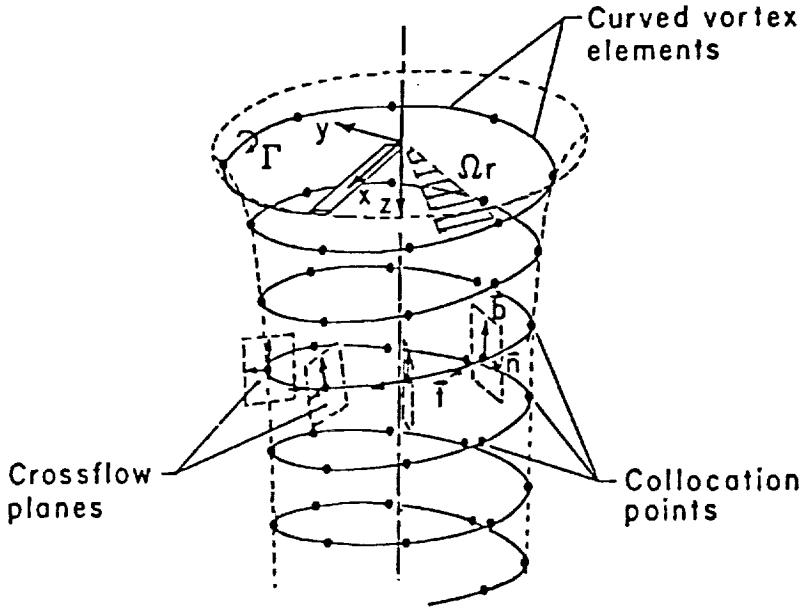


Figure 3. Tip vortex wake represented by curved vortex elements, showing the crossflow planes at collocation points.

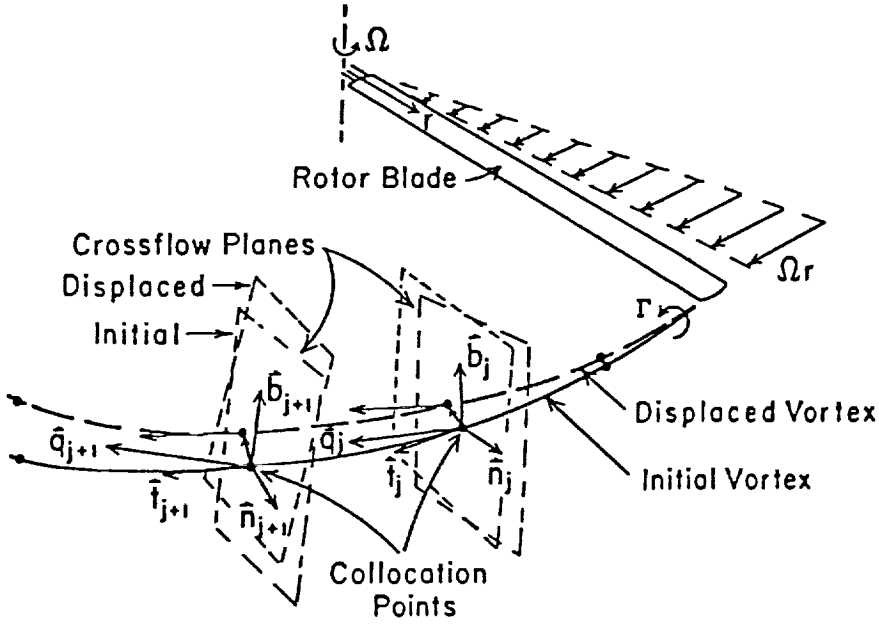


Figure 4. Method of displacing a vortex to eliminate velocity components in planes normal to the vortex curve. Equilibrium state is zero crossflow velocity in every plane.

point on every other point is known. More precisely, an influence coefficient matrix relating crossflow velocity perturbations to small displacements from a given wake configuration has been established.

For a given arrangement of the free wake collocation points, the net velocity in each crossflow plane can be computed. To move toward the desired solution, the collocation points must be displaced so as to reduce these crossflow velocities. This process is illustrated in Figure 4. The influence coefficient matrix can be used to predict the set of collocation point displacements which will reduce all the crossflow velocities. Mathematically, this procedure is essentially a multi-dimensional Newton-Raphson technique. The solution of a linear algebraic system for these point displacements is required. If the wake flow field problem were linear, only a single matrix inversion would be required to obtain the solution. Since the wake problem is actually nonlinear, the procedure involves a relaxation process in which the solution is reached through a series of quasi-linear steps.

It should be emphasized that the repeated application of the procedure described above does not correspond to time stepping. On the contrary, it is just a systematic way of moving toward the steady self-preserving solution in a quasi-linear manner. In this process, the collocation points are moved to reduce the crossflow velocities, rather than being moved in the directions indicated by the crossflow velocities. Thus, the successive displacements obtained from repeated applications of the influence coefficient method do not correspond to a physical motion of the wake. This is one reason why stability of the physical flow field is not a requirement for the influence coefficient method to work.

It should also be emphasized that the approach just described is restricted to cases where a steady self-preserving solution can be found. This restriction limits the applicability of the method to rotors in hover and axial flight. In these cases there is an ideal steady solution when the flow field is viewed in a coordinate frame rotating with the blades. This solution method is not applicable to forward flight since there is no reference frame in which the flow field can be made to appear steady. Converged forward flight solutions are periodic in time, rather than steady.

It might be noticed that there is a similarity between the method just described and lifting surface theory. In lifting surface theory, the positions of bound vortices are known but their strengths are unknown. A set of linear equations expresses the unknown strengths in terms of known downwash velocities at control points. These equations are also solved by matrix inversions. Because the problem is linear only a single matrix inversion is required.

Because of the similarity between the two methods, the wake solution method and a blade lifting surface theory can be combined and solved simultaneously. This is one of the great advantages of the present approach. The wake filaments can be extended to the blade and their strengths related to the strengths of the bound vortices. The unknowns in the problem are now the wake collocation point positions and the strengths of the bound

vortices on the blade (which also control the wake strengths). An extended influence matrix can be derived which accounts for wake-on-wake, blade-on-blade, wake-on-blade and blade-on-wake effects. The unknown vector, composed of both bound vortex strengths and wake positions, is linearly related through the influence matrix to the known blade downwash boundary conditions and the known conditions for force free equilibrium of the wake filaments. Inversion of the matrix leads to a solution for the unknown vector. Because the portion of the problem related to the wake is nonlinear, a relaxation procedure involving repeated inversions from updated wake positions is required to achieve convergence. In this process the blade aerodynamics and the wake aerodynamics are simultaneously brought to the final solution. An interesting property of this quasi-linear process is that it proceeds more rapidly and accurately as the solution is approached, i.e., as it becomes linearly close to the final solution. As a result, final convergence of the entire solution is unambiguous. Unlike other hover analyses, strict convergence criteria can be specified and satisfied throughout the wake. Section 3 discusses blade/wake coupling in more detail.

### 1.3 Treatment of Wake Filaments

This subsection describes the treatment of the individual wake filaments that make up the hover analysis wake. The first important point to be discussed is how strings of filaments are handled. Each filament is subjected to two important effects: the velocity induced by the Biot-Savart integration and the convection velocity associated with the free stream velocity and climb velocity (if present). The Biot-Savart contribution is elliptic in nature with every portion of the wake influencing every other portion. However, the convection terms produce only an upwind effect. This can be seen by imagining a rotor in climb with a tip vortex of zero strength. Then the "vortex" would just be a marker spiraling downward with the flow. There is no downwind influence on a point on this marker; only its upwind history is important. Only an upwind difference scheme will give a correct calculation of the marker motion.

Because of the strong convection effect, a second-order upwind difference scheme is used to compute the normal and binormal vectors that define the crossflow planes. This approach is essential to obtain accurate solutions and to assure robust convergence. In other words, if $j-2$ , $j-1$ and $j$ are three points successively further down a filament, the locations of these three points (and no others) are used to compute the normal and binormal vectors at $j$ , (see Figure 5). With this approach the bottom point of a filament requires no special boundary condition to determine its crossflow plane. However, the first and second points at the top require special treatment. In the present analysis the position of the top point is specified as being a filament release point at a given point on the blade. Since the position is given, the unknown quantity at this first point is the tangent vector to the filament. At the second point, and all subsequent points down the filament, the unknowns are the point coordinates. The second point is special only in that its normal and binormal are calculated using the position and slope of the first point, rather than the positions of two preceding

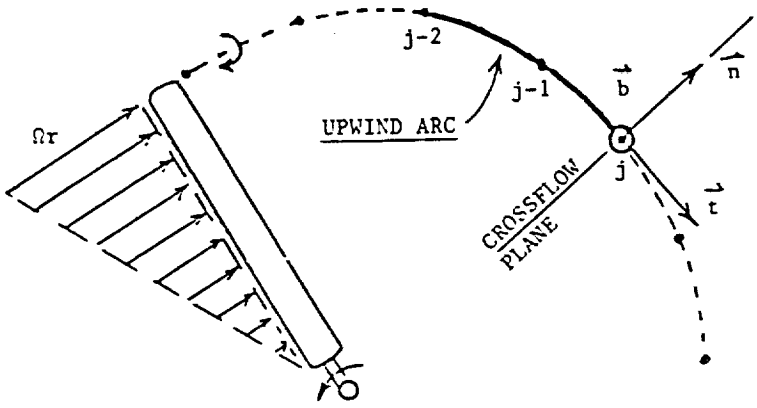


Figure 5. Upwind arc method to determine crossflow planes.

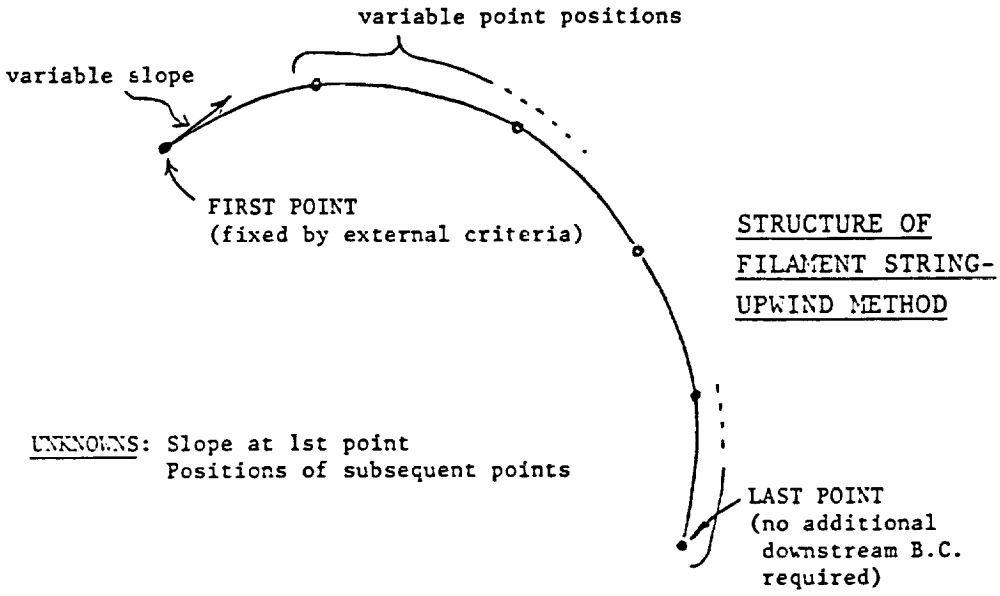


Figure 6. Structure of a multi-element vortex filament using the upwind method.

points. By using this approach each filament is a relatively self-contained entity (see Figure 6).

At this point a clarification regarding the use of an upwind scheme to determine filament geometry is appropriate. Upwind difference schemes have sometimes been used inappropriately in traditional numerical analysis, so it is important to understand how the present approach is different. The current scheme still contains full upward and downward influence at all points due to the Biot-Savart calculation. This calculation is in no way simplified or reduced by the present scheme. The vortex induced velocity field always acts on all collocation points at every step through the solution procedure, as is physically correct. It is for this reason that the present approach is not an upwind scheme of the type traditionally encountered in numerical methods. Only the crossflow plane orientation is determined by an upwind scheme, and this is a matter of geometry alone. As mentioned earlier, the correctness of this approach can be seen by setting the filament circulation to zero, so that the filament is only a marker (i.e., smoke) in the fluid. The strong convective velocity dominated by the rotating frame then carries the marker away. Clearly, a given collocation point only experiences upwind influence. The present approach thereby incorporates the strong upwind convective effect, but still retains the full influence of the vorticity field through the Biot-Savart law.

The second-order scheme used to determine the normal and binormal at the downwind point is itself of interest. Initially circular arcs were passed through each set of three points. This approach was particularly convenient because the curved vortex element calculation already computed these arcs during the determination of element properties. However, it was found that planar arcs cause a significant torsion error. The normal and binormal vectors have an orientation error because the torsion of the actual helical wake filament is not taken into account. This error leads to wake solutions with incorrect pitch. The problem was particularly serious when large curved elements were used.

In order to remedy this problem, the calculation of the local tangent, normal and binormal vectors utilizes curves that are inherently torsional, thereby minimizing the torsion error in the first place. A "helical" curve fit is used through each set of three adjacent points. Specifically, the wake curves are written in global Cartesian coordinates as

$$x = R(\psi)\cos\psi \quad , \quad y = R(\psi)\sin\psi \quad , \quad z = Z(\psi) \qquad (1)$$

where $R(\psi)$ , $\psi$ , $Z(\psi)$ are cylindrical coordinates of a point in the wake. An important feature of this approach is that the trigonometric functions $\cos\psi$ and $\sin\psi$ are retained explicitly. The choices $R$ = constant and $Z = k\psi$ recover a right circular helix having constant torsion. In contrast, the circular arc method entailed a torsion error even for this case. The

functions $R(\psi)$ and $Z(\psi)$ are determined to assure the correct values for each set of three points at $\psi_{j-2}$, $\psi_{j-1}$ and $\psi_j$ and are represented as quadratic functions of $\psi$. These quadratic functions are interpreted as Taylor series expansions and the first and second derivatives of $R(\psi)$ and $Z(\psi)$ at point $j$ may be determined accordingly. The overall position vector $\vec{r} = x\vec{i} + y\vec{j} + z\vec{k}$ can be repeatedly differentiated with respect to arc length to obtain formulas for the local tangent, normal and binormal vectors on the filament curve. The tangent vector found in this manner has second-order accuracy, thereby guaranteeing an accurate prediction of the crossflow plane orientation. The treatment differs somewhat for the special first and second points on the filament, where the slope variable must be introduced. Careful tests of the use of helical arcs to calculate the wake geometry have shown that this approach renders the torsion error insignificant, even for large arcs.

## 1.4 Free Wake Implementation

A free wake analysis necessarily involves only a finite number of turns of free vortex. Beyond the free wake region, the wake must be continued using a far wake model if the solution is to be physically correct. The present subsection deals only with the free wake region and the far wake model is described later. This free wake region is composed of a number of filaments trailed from the primary blade to simulate the tip vortex, inboard sheet, and the root vortex. Other blades and their wakes are assumed to have the identical configuration, since the ideal solution will have blade-to-blade symmetry, and are handled by an equivalent image system.

As explained earlier, the new solution method involves determining influence coefficients that relate perturbation velocities at free wake collocation points to the displacements of these points. These influence coefficients are used to predict how the collocation points should be moved in order to reduce the velocity components in crossflow planes along the wake curve. When these crossflow velocities are reduced to zero, the condition for a steady self-preserving flow is satisfied, and the desired solution is obtained. The problem is analyzed in a coordinate frame rotating with the rotor. The purpose of this section is to describe the implementation of this method in somewhat greater detail.

Because of the complexity of the problem, the influence coefficients for wake effects must be calculated numerically rather than analytically. The numerical calculation of the influence coefficients, although straightforward in principle, is in fact a fairly complex and intricate process. A number of interrelated calculations must be made, and it is important to do this as efficiently as possible. Conceptually, it is easiest to think of displacing a collocation point and doing all the velocity calculations associated with this displacement. The influence coefficients relating the velocity perturbations at every point to this displacement can then be calculated. In practice, it is much more efficient to do all the calculations associated with a particular curved vortex element at the same time. This means that a particular element's contributions to all the influence coefficients are being acquired

at once. The influence coefficients are completely determined only after all these calculations have been completed for every element. Although this approach is more efficient, the programming logic is more complicated.

At the beginning of each solution cycle, the wake is defined by the positions of the collocation points. In order to locate the Basic Curved Vortex Elements (BCVE's), interpolated points midway between the collocation points must be generated. In Ref. 7, the interpolated points were found by an overlapping arc method which uses information from the four nearest collocation points. This is basically a central difference scheme. A four-point method is unnecessarily complex in the hover case where it is known that the wake shape will be a relatively smooth curve (with slowly varying curvature) centered about the rotor axis. For the hover analysis, the interpolated points were found by an external interpolation scheme that used only two collocation points with the upwind helical arc scheme described previously. Actually, these interpolated points must be found not only for the basic wake configuration, but also for each configuration change due to a collocation point displacement. An important consequence of this simpler scheme is that displacing a collocation point changes the positions of only the two adjacent BCVE's, rather than four BCVE's. As a result, the programming logic is greatly simplified and the computing time is substantially reduced.

The normal and binormal vectors, and hence the crossflow plane orientations, must be determined at each collocation point location. Helical arcs are passed through each set of three adjacent collocation points using an upwind scheme to find the normal and binormal vectors at the downwind point. At the same time, the Self-Induction Vortex Element (SIVE) contribution is also found for the center point. Once the normal and binormal vectors have been determined, the directions of the collocation point displacements are known, and the geometry of the wake displacements can be established.

For each BCVE, seven calculation loops are then required. These seven loops involve finding the velocity induced by the BCVE at all the wake points not touching the end of the element and at all control points on the blade. Three of these calculation loops determine the velocities at collocation points in their original positions and when displaced in their normal and binormal directions. The other four calculation loops are required to find the effect of the BCVE at all other points when each of its two endpoints are independently displaced normally and binormally. Because of the way the BCVE analysis is formulated, all calculations must be made in local element coordinates and then transferred to a global reference frame on the rotor.

For each SIVE, six calculation loops are required at each collocation point. The SIVE contribution at a point changes when any of the three points determining its shape are displaced in the normal and binormal directions. In addition to the self-induction effect, these six displacements each produce changes in the normal and binormal directions at the element's points. This effect must also be included in the final determination of the influence coefficients.

In addition to the above, calculations are also required for the far wake vortex elements located beneath the free wake (see Figure 7), and for the wakes from additional blades. The far wake has an effect on the influence coefficients for two reasons. First, displacing collocation points in the nonuniform velocity field of these parts of the wake produces a contribution. Second, as explained later, the configuration and location of the far wake changes as the free wake distorts and as the net rotor thrust changes.

For the multiple blade case, the fact that the desired solution will be symmetric from blade to blade is used to define the locations of the other blade wakes in terms of the location of the primary wake. Furthermore, symmetry allows the effect of another wake on the primary wake to be expressed in terms of the corresponding effect of the primary wake on another wake. Therefore, the effects of other wakes can be handled as additional BCVE calculations for each element. The calculation procedure to account for the effects of all the various multiple wake displacements, in the appropriate normal and binormal directions, is an intricate process. Because symmetry has been invoked, the multiple blade case does not introduce more free wake points and does not raise the order of the influence coefficient matrix. However, the length of the process to calculate the influence coefficients increases directly with the number of blades.

The various calculations described above must be modified to account for certain exceptional cases that arise. The most important of these is the treatment of the first free wake point which involves changes in the tangent vector rather than changes in the point position. Special considerations associated with joining the wake to the blade are covered later in Section 3.

In addition to the wake effects described above, it is necessary to include the velocity contributions due to the lifting surface bound circulations on the rotor blades, any axial (climb) velocity component, and the rotating frame velocity magnitude $\Omega r$ . Once all the different effects have been computed and summed, the resultant velocity vectors at each collocation point are expressed in the blade fixed reference frame. These resultant vectors are dotted with the local normal and binormal vectors to obtain the crossflow velocity components and their changes associated with point displacements. The velocity changes can then be normalized by the point displacement magnitudes to obtain the influence coefficients. These coefficients give the influence of displacing each wake collocation point normally and binormally on the crossflow velocity at every other free wake point and at the lifting surface control points on the blade. Corresponding coefficients must also be determined for the influence of changes in blade bound circulations on the wake crossflow velocities, and the downwash velocities at the blade control points. This process is more straightforward.

The mathematical form of the wake relaxation is now discussed. For the purposes of illustration, the case of a wake composed of a single constant-strength vortex filament is considered (i.e., the coupling to the blade aerodynamic load is ignored). The more general case of a multiple-filament case with explicit coupling to the blade load is discussed in Section 3.

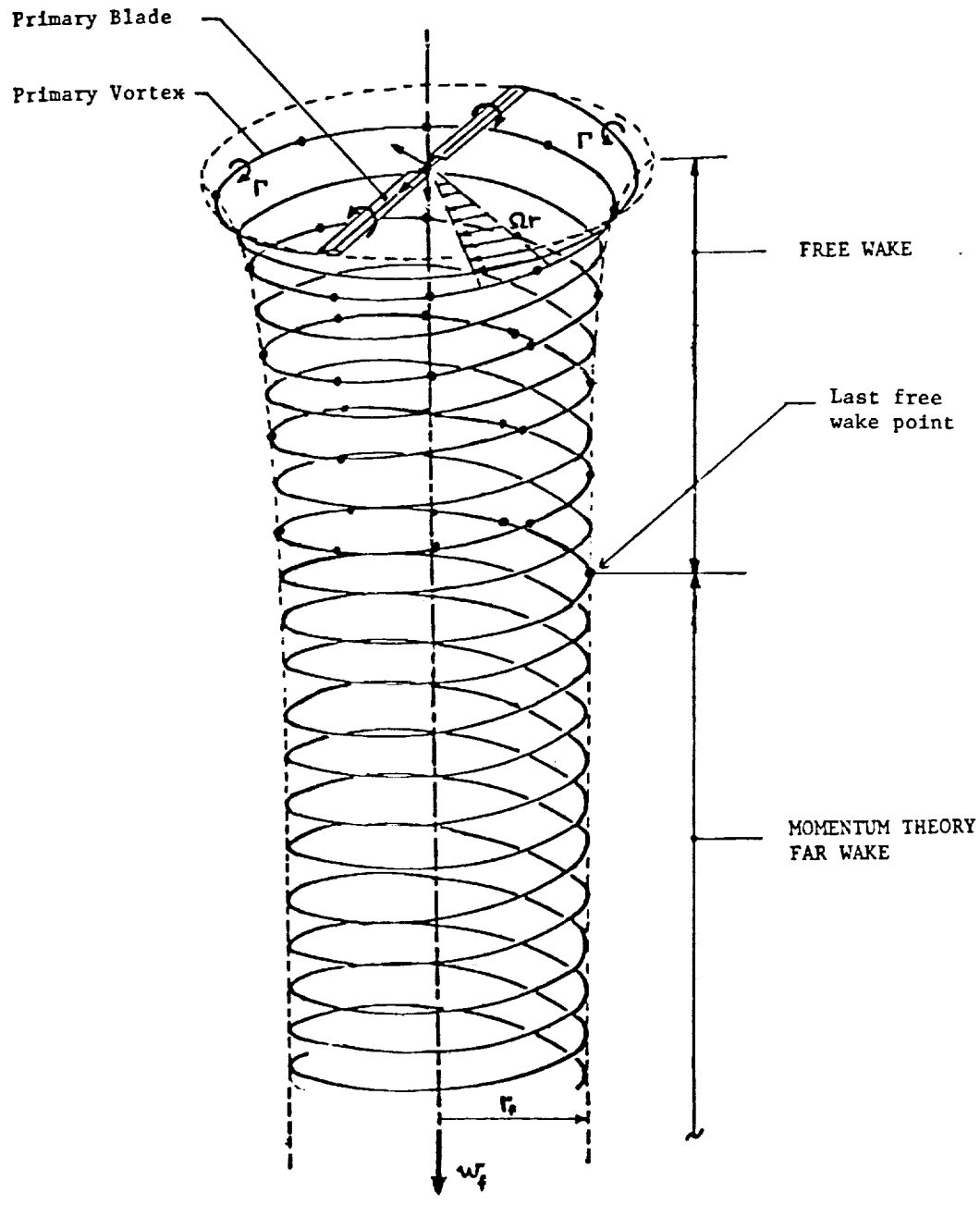


Figure 7. The two-part wake structure for the hover analysis.

Given that $q_n$ and $q_b$ denote the normal and binormal components, respectively, of the velocity field at the wake collocation points, the linearized derivatives or influence coefficients associated with the single-filament wake can be expressed as follows:

$$
\begin{aligned}
Q_{nn}^{ij} &= \frac{\partial q_{n_i}}{\partial n_j} \\
Q_{nb}^{ij} &= \frac{\partial q_{n_i}}{\partial b_j} \\
Q_{bn}^{ij} &= \frac{\partial q_{b_i}}{\partial n_j} \\
Q_{bb}^{ij} &= \frac{\partial q_{b_i}}{\partial b_j}
\end{aligned}
\qquad (2)
$$

for $1 \leq i \leq N$ and $1 \leq j \leq N$, where $N$ is the number of free wake points. Note that these coefficients denote the effect of displacing the $j^{\underline{th}}$ point on the velocitied at the $i^{\underline{th}}$ point. Although not obvious in this notation, the effect of changing normal and binormal vector directions is also included in the numerical calculation of these influence coefficient.

The corresponding influence coefficient matrices are defined as

$$
\begin{aligned}
Q_{nn} &= [Q_{nn}^{ij}] \\
Q_{nb} &= [Q_{nb}^{ij}] \\
Q_{bn} &= [Q_{bn}^{ij}] \\
Q_{bb} &= [Q_{bb}^{ij}]
\end{aligned}
\qquad (3)
$$

Now define change of displacement vectors

$$
\begin{aligned}
\vec{\Delta n} &= (\Delta n_1, \Delta n_2, \ldots\ldots, \Delta n_N) \\
\vec{\Delta b} &= (\Delta b_1, \Delta b_2, \ldots\ldots, \Delta b_N)
\end{aligned}
\qquad (4)
$$

and velocity change vectors

$$\Delta\vec{q}_n = (\Delta q_{n_1}, \Delta q_{n_2}, \ldots\ldots, \Delta q_{n_N})$$

$$\Delta\vec{q}_b = (\Delta q_{b_1}, \Delta q_{b_2}, \ldots\ldots, \Delta q_{b_N}) \qquad (5)$$

The velocity change vectors are related to the change of displcement vectors through the influence coefficient matrices, namely

$$\tilde{Q}_{nn}\Delta\vec{n} + \tilde{Q}_{nb}\Delta\vec{b} = \Delta\vec{q}_n$$

$$\tilde{Q}_{bn}\Delta\vec{n} + \tilde{Q}_{bb}\Delta\vec{b} = \Delta\vec{q}_b \qquad (6)$$

To obtain zero net crossflow velocity, it is necessary to choose the point displacements so that the velocity changes cancel the net crossflow velocity. First define vectors based on the crossflow velocity components

$$\vec{q}_n = (q_{n_1}, q_{n_2}, \ldots\ldots, q_{n_N})$$

$$\vec{q}_b = (q_{b_1}, q_{b_2}, \ldots\ldots, q_{b_N}) \qquad (7)$$

In order to cancel these crossflow velocity vectors, it is necessary that

$$\Delta\vec{q}_n = -\vec{q}_n$$

$$\Delta\vec{q}_b = -\vec{q}_b \qquad (8)$$

Equations (6) and (8) can now be solved simultaneously for the change of displacement vectors $\Delta\vec{n}$ and $\Delta\vec{b}$ . The results are

$$\vec{\Delta b} = [\tilde{\tilde{Q}}_{nn}^{-1}\tilde{\tilde{Q}}_{nb} - \tilde{\tilde{Q}}_{bn}^{-1}\tilde{\tilde{Q}}_{bb}]^{-1}(\tilde{\tilde{Q}}_{bn}^{-1}\vec{q}_b - \tilde{\tilde{Q}}_{nn}^{-1}\vec{q}_n)$$

$$\vec{\Delta n} = -\tilde{\tilde{Q}}_{nn}^{-1}\vec{q}_n + \tilde{\tilde{Q}}_{nn}^{-1}\tilde{\tilde{Q}}_{nb}\vec{\Delta b} \qquad (9)$$

The collocation points are displaced by $\vec{\Delta b}$ and $\vec{\Delta n}$ to obtain a new wake shape. Since the wake problem is nonlinear, this process must be repeated several times. Convergence to the final answer proceeds in a multi-dimensional Newton-Raphson manner. The numerical calculation of the influence coefficient matrices must be repeated each time. Although 2N displacements are calculated, the above formulation involves inverting only an NxN matrix. The matrix inversion process is essentially an N-squared computation in terms of computer time.

Having outlined all the steps in the solution procedure it is now possible to estimate the computer time required for this wake-only case. The computer time is dominated by the calculation of the influence coefficients, and in particular the calculations involving BCVE's. Let $T_c$ be the time to do a single BCVE calculation. The total number of BCVE's composing a single tip vortex is $N_T$, which includes the free wake, the intermediate prescribed wake, and the first two turns of the far wake (as explained later). The total number of tip vortices equals the number of blades, B. In the current scheme, seven calculation loops are required for the influence coefficient calculations involving BCVE's. These calculations must be made for $N_F$ free wake points. These factors lead to a estimated time per calculation cycle of $(7BN_T)T_cN_F$. To obtain a solution, a few such calculation cycles are required. Denoting the number of calculation cycles by $K_I$, the total computer time to converge a solution by the influence coefficient method is roughly

$$t_I \sim K_I 7 T_c B N_F N_T \qquad \text{(influence coefficient method)} \qquad (10)$$

The time required to converge a time stepping routine can also be estimated. Again the BCVE calculations dominate. The time for one calculation cycle is now $T_c(BN_F)(BN_T)$, assuming every blade wake is now free to move independently (to assure real physical motions). To "converge" a time marching scheme requires more time steps than the number of free wake points, say $K_cN_F$. Therefore, the convergence time for a time stepping routine is approximately

$$t_{TS} \sim K_c T_c B^2 N_F^2 N_T \qquad \text{(time stepping methods)} \qquad (11)$$

Comparing the two convergence times, the influence coefficient method is faster whenever $N_F > 7K_I/K_cB$ . As a conservative example, suppose $K_I = 8$ , $K_c = 2$ and $B = 2$ . Then for a calculation involving more than about 14 free wake points, the influence coefficient method is faster.

The above convergence times can also be compared for calculations involving very large numbers of free wake points. In this case, $N_T$ can be replaced by $N_F$ for estimation purposes. For the influence coefficient method, the convergence time is then proportional to $BN_F^2$ , whereas for a time stepping scheme it is proportional to $B^2N_F^3$ . Thus, the time to do calculations by the influence coefficient method increases less rapidly as the number of blades and the number of free wake points increase. These conclusions also hold for cases in which the blade is explicitly coupled into the overall relaxation.

To sum up this discussion, the influence coefficients show the effect of linearly small changes in wake displacements on all the collocation points. In a linear sense, the changes in displacements required to null wake crossflow velocities can be found by solving this linear system. It is important to note, however, that since the system is not truly linear, the solution process must be repeated a number of times using updated velocities and influence coefficients. Also, as alluded to above, a fully consistent solution is achieved only if the blades aerodynamics load distribution is explicitly included in the calculation. Following a description of the lifting surface aerodynamic analysis in Section 2, Section 3 will discuss how the linearized system described above is augmented to include the effects of changes in the bound circulation.

It is important to realize, however, that repeated application of this process starting from an initial wake shape is not the most efficient or reliable way to converge the solution, unless the initial shape is very close to the correct answer. Instead, it is better to relax the solution in quasi-linear steps from a known solution. One such solution is the wake of a rotor in axial motion with zero thrust and zero circulation, whose geometry is determined solely by kinematics. In this case, the "wake" is just a marker in the fluid that traces out a known constant radius helix for each wake filament. Conceptually, the blade in this case can be thought of as being perfectly porous. In a series of steps, the rotor climb velocity is decremented to zero while the rotor blade becomes increasingly impervious to normal velocity in corresponding steps. To achieve this, the downwash boundary condition at the blade control points is stepped up to its final value in increments. Each increment is sufficiently small that only a single application of the solution procedure is required to get very close to the next intermediate solution. At each of these steps the far wake is also adjusted in an appropriate manner. In the current computer program, using ten to fifteen of these relaxation steps is usually adequate. At the end of the process, a few additional inversions are also required to finish converging the solution. During the incrementing process, it is desirable to control the displacements of the wake vortices to keep the individual relaxation steps as linear as possible. This was done by using momentum theory to relate the initial climb velocity to the final downwash velocity in a way that keeps the

vertical positions of the vortex turns relatively constant during the relaxation process. The best convergence results are obtained by using an initial climb velocity somewhat higher than the final downwash velocity. This approach keeps the wake more spread out during the convergence steps and reduces the sensitivity of the solution.

One very important and instructive aspect of the influence coefficient matrix associated with the converged solution is that its eigenvalues contain information on the temporal stability of the final wake geometry. Appendix B summarizes the results of a representative model problem featuring a single-bladed rotor with a constant-strength tip vortices. The results clearly show the underlying instability alluded to above that undermines convergence in time-marching analyses of rotor wakes.

Finally, it is appropriate to comment on an other interesting feature of the influence coefficient scheme regarding convergence. At each step, both the influence coefficients and the wake crossflow velocities are recalculated. Great care has been taken to use formal, fully consistent calculations of the influence coefficients. This ensures that in the linear regime, the predicted wake displacements will yield zero crossflow velocities at each wake point. This is the case once the wake is linearly close to the final converged answer. An advantage of formulating the scheme in this manner, encountered repeatedly during code development, is that the influence coefficient evaluations are effectively self-checking. Whenever a fundamental error was made in coding the influence coefficient routines, the code would reveal this error by failing to converge. Unlike many numerical schemes which will converge to the wrong answer if they contain an error, any significant coding mistake in the influence coefficient routines will prevent convergence. Therefore, if the code converges, any coding mistakes related to influence coefficients must be insignificant.

## 1.5 Far Wake Model

It is necessary to continue the free wake region with a far wake model. It is important to understand the role of the far wake in the overall wake solution. A converged wake solution is intended to be a good approximation to the solution of the equations of motion for flow over a rotor. This being the case, it is possible to consider a large spherical control volume centered at the rotor hub. If the wake were truly in free motion, the only internal force acting on the fluid in the control volume would be the rotor thrust. If the control volume is very large, the fluid at its boundary will be at the ambient static pressure everywhere, and there will be no net pressure force on the boundary. The net momentum flux through the boundary will be associated with the far wake. In the absence of external pressure forces, and with the rotor in steady state operation, the net far wake momentum flux must equal the rotor thrust. If this condition is not satisfied, there must be other internal forces within the control volume. These internal forces can arise as Kutta-Joukowski forces on the fixed vortices used in the wake model below the free wake region, since this part of the wake is effectively composed of bound vortices. If the far wake model is poorly executed it will exert a net thrust

which alters the free wake structure and interferes with the rotor. In short, the far wake model must be as realistic and as force free as possible. It is also desirable to extend the free wake fairly far below the rotor to reduce any residual adverse effects.

The far wake model used in the hover analysis code is an idealized extension of the free wake. The free wake filaments are continued as ideal discrete helices into the far wake. Viscous and turbulent diffusion of momentum are not accounted for in this model. Although these real flow factors do alter the transport of vorticity away from the rotor, the excellent agreement with data obtained by the present method suggests that this effect must be small.

An important aspect of the far wake treatment is actually part of the free wake solution. The variable element size capability of the code is used to extend the free wake father downward for the same total number of elements. Very large elements are used near the bottom of the free wake providing a variable resolution of the wake. This approach is quite acceptable since nearly all the contraction occurs in the first couple of wake turns. Farther down, the wake behaves in a very smooth fashion. As a result, the wake properties are essentially unchanging at the far wake attachment point. Furthermore, extending the free wake with larger elements moves the far wake attachment point farther from the blade, so that any residual effects are less important. By taking this approach, the far wake attached to each filament can be viewed as the final, largest element in a variable resolution scheme to treat the wake. Because the far wake is attached after the wake contraction is complete, and because it utilizes properties of the free wake solution, it should be very nearly force free.

In some of the test cases to be shown later, it will be noted that the free wake/far wake junction is not absolutely smooth. This was, in most cases, due to the use of a relatively small amount of free wake for the purpose of executing efficient sample calculations. As will be discussed later, conservative choices of free wake length (i.e., extending the free wake roughly one diameter below the rotor) will minimize or eliminate any mismatch. Also, by using a long free wake, the effect of any such residual inconsistency in the far wake geometry is also minimized because of the exponential decay of the far wake influence on the rotor blades.

The far wake is composed of semi-infinite helical filaments (see Figure 7). There is one such far wake filament attached to each free wake filament trailed from the principal blade, with appropriate accounting for the corresponding filaments from other blades. Each helix has the same radius as the last free wake point on that filament. The helix pitch (turn-to-turn spacing) is determined from a momentum theory calculation of the wake downwash using the value of net rotor thrust coefficient. In hover, the tip vortex helix descends at half the momentum theory downwash value because it is on the wake boundary, and the inboard filaments descend at the full value.

The vortex elements making up the far wake helices are summed as vertical arrays. The first few elements, corresponding to the first few turns, in each

array, are summed as discrete BCVE's. At least two wake turns of BCVE's are summed in this manner; more turns may be added at the user's discretion. The rest of each semi-infinite element array can be represented by a special summation procedure. Reference 7 shows that semi-infinite arrays, or stacks, of curved elements can be summed approximately. It is necessary to know only four quantities: the velocities induced by the first two curved elements in the stack at the point of evaluation; the vector distance from the first element in the stack to the point of evaluation; and the vector that defines the array orientation and spacing. The derivation in Ref. 7 covers stacks of arbitrary orientation. Here, the stacks are vertical, so the magnitude of the spacing vector is simply the distance between far wake turns.

Using only the two spacing vectors cited, two scalar quantities can be derived that multiply the induced velocity vectors to give the summation of the array. These scalar multipliers contain infinite sums that can be approximated by known integrals after the first few turns. Thus, the velocity contribution of this entire semi-infinite helical structure can be calculated very efficiently.

In terms of the influence coefficient method, the motion of the last free wake point produces a change in the entire far wake, as well as a change in the last free wake BCVE. This effect is included in the influence matrix accounting for the effect of this displacement on other wake collocation points and on the blade control points.

# 2. LIFTING-SURFACE ANALYSIS AND BLADE LAYOUT

## 2.1 Vortex Quadrilateral, Lifting-Surface Analysis

In order to calculate the average performance characteristics of the rotor blade, a lifting-surface analysis of the blade circulation distribution has been included in the solution method. Flexibility has also been provided in the specification of the rotor blade geometry. This flexibility allows the investigation of the effect of various blade-geometry parameters (sweep, taper, twist, anhedral, camber) on both the flow field and the rotor performance.

Panel methods have been widely utilized in the computation of flow around aircraft of complex configurations (Refs. 8-17). These methods use a distribution of sources, doublets or vortices, or different combinations of these entities arranged in a variety of geometrical forms. The rotor blade is represented in the present work by a surface consisting of vortex quadrilaterals. In the case of a vortex quadrilateral panel, four constant strength straight-line vortices form the sides of a quadrilateral. At the trailing edge of the blade, a modified vortex quadrilateral without the downstream line vortex is used. The sides of the modified vortex quadrilaterals are extended in curved vortex elements which represent the near wake. These "horseshoe" trailers are discussed later in the near wake treatment (Section 4.2). The directions of the vortices point in the same sense around each quadrilateral loop; the positive direction is taken to be clockwise around the perimeter of the quadrilateral when looking at the upper surface. The quadrilaterals are not necessarily planar.

The vortex quadrilateral method has been employed by Maskew (Ref. 11) to compute steady, incompressible flow about arbitrary lifting configurations and by Tulinius (Ref. 13) to compute the perturbation velocity induced by a fanpod and fuselage in the vicinity of a pylon, nacelle and thick wing. Other panel methods, similar in spirit and general approach, have been used by Kocurek and Tangler (Ref. 14), Summa and Clark (Ref 15) and Summa and Maskew (Ref. 16). These approaches use either flat or curved doublet panels as the fundamental "building block" of their models. Such doublet-based models have an advantage in computational efficiency over vortex quadrilateral methods, but both produce fundamentally the same model of a given thin surface. For example, a vortex quad in the current analysis produces a velocity field identical to a constant-strength doublet panel covering the same area.

No attempt has been made to rigorously compare and examine the various panel methods. The vortex quadrilateral method was chosen because it appears to have several desirable features within the framework of the current work. First, the unknown circulations of the vortex quadrilaterals can be solved for using the influence coefficient approach which has been employed for calculating the wake. In this way, the lifting-surface and free wake problems are easily combined into one calculation and can be solved simultaneously. This is obviously a highly advantageous scenario as it avoids the need for any artifical numerical iteration between the two solutions. Also, the vortex

quadrilateral representation is readily integrated geometrically into the existing trailing vortex filament model of Ref. 6. At present, each trailing vortex filament is attached to the control point of a modified vortex quadrilateral at the trailing edge of the blade (see also Section 3 below). This is convenient because the blade-induced velocity at this point is known exactly from the lifting-surface calculation.

The vortex quadrilateral method has several limitations shared by all the panel methods of Refs. 8-17. The method is based on potential flow theory for an incompressible flow. Approximate subsonic compressibility corrections have been added to account for subcritical compressibility effects (see Section 5.1.3). Viscous effects have also been approximated by including two-dimensional drag coefficients (see Section 5.1.2). The present formulation is inadequate for treating leading edge and blade-tip separations.

## 2.2 Blade Specification and Lattice Construction

The present blade model was selected for its realistic representation of a typical helicopter rotor blade, as well as for its ease of use by the user of the computer program. The blade consists of several segments each having its own anhedral, sweep, taper and twist. The blade segments have no thickness. Camber heights can be specified over the entire length of the blade. The blade is defined within a right-handed Cartesian xyz reference frame (Figure 8). The z-axis is positive downward along the rotor shaft. The x-axis is positive radially outward along a given blade in the plane normal to the z-axis. The x-axis passes through the 1/4-chord point of the root chord of the blade. For blades with neither sweep nor anhedral, the x-axis is the 1/4-chord line of the blade. The y-axis is the vector cross product of the z and x axes which means it is positive toward the blade's trailing edge when viewed from above. The blade radius is the x-value at the blade tip. Chord lines are laid out in the y-direction (even for swept blades). Chord lines will acquire z-components through twist or camber and x-components if these are combined with anhedral.

The following list describes the input parameters that must be supplied by the user. Helpful comments concerning the selection of these input parameters can be found in Section 3.2 of the CDI-EHPIC Users Manual which describes the procedure for specifying the blade geometry.

1) The distance CUTOUT.

2) The number of spanwise segments.

3) The length of each segment, measured along the quarter-chord.

4) The chord lengths at the root, at the segment junctions, and at the tip of the blade.

5) The sweep angle of each segment, defined to be the angle between the x-axis and the quarter-chord line before any anhedral angle is applied (Figure 9).

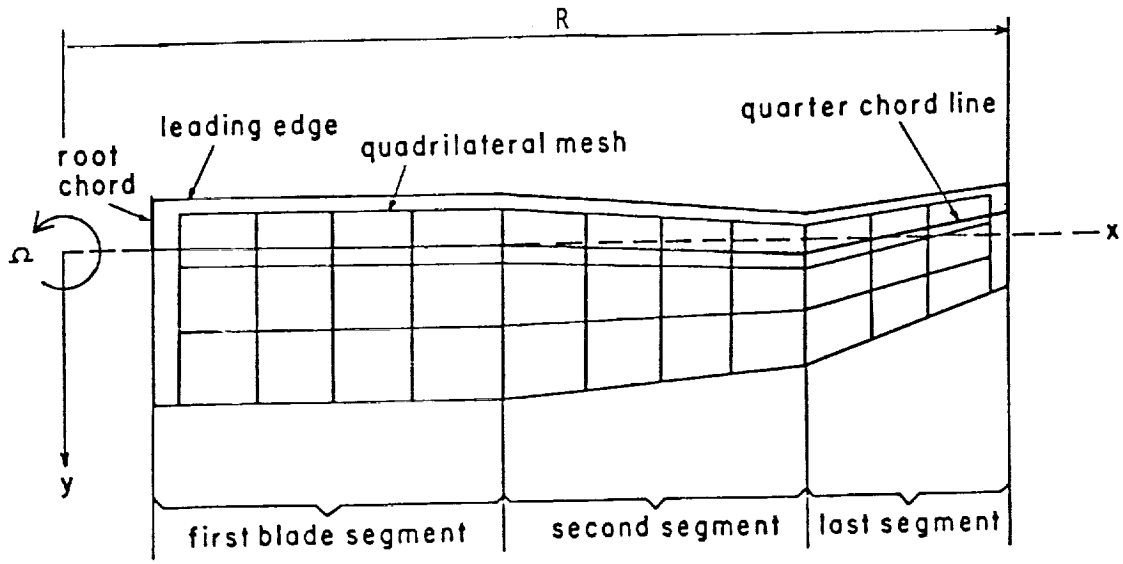


Figure 8. Typical blade layout, showing coordinate axes (the z axis is directed into the page).

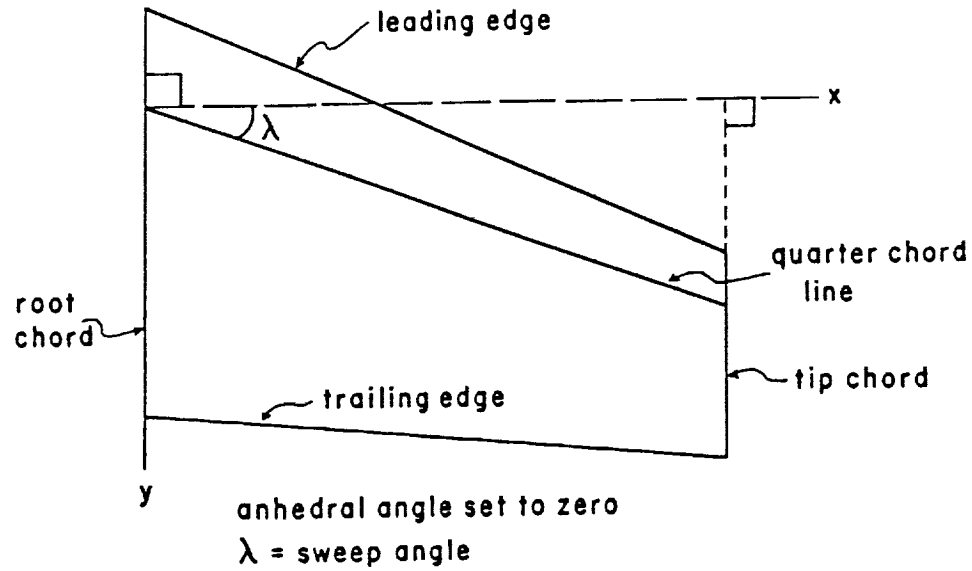


Figure 9. Definition of the sweep angle.

6) The twist angle at the root and the total change in twist angle over the span of each segment. The twist angle (Figure 10) is defined to be the angle between the local chord and the xy-plane before any anhedral angle is applied; it is positive if the trailing end of the chord is lower than the leading end. At present, the twist distribution is assumed to be linear over any segment.

7) The anhedral angle (droop) is the angle any perpendicular, drawn from the quarter-chord line to the y-axis, makes with the xy-plane. It is positive if the z-coordinate of the quarter-chord point on the segment tip is larger than that of the segment root (Figure 11).

8) The camber distribution is given in terms of a chordwise distribution of height above the plane defined by a chord and a segment's quarter-chord line (Figure 12). The corresponding height above any chord is in the direction normal to this plane. (Note: camber has been neglected in all runs documented in this report. The camber option has been created with future code development in mind and should not be invoked until a structural model is included that will account for torsional deflection.)

Upon receiving these parameters, the computer program takes the following steps when constructing the blade. These steps are performed segment by segment, starting from the first.

1) The specified root and tip chords of each segment are placed on the xy-plane normal to the x-axis such that their 1/4-chord points are at the specified distance apart and the 1/4-chord line is swept back by the specified sweep angle from the x-axis, toward the trailing edge. The root end of the 1/4-chord line is placed at the origin to simplify the blade construction. A straight line is drawn to join the leading edge points of the root and tip chords, and another is drawn to join the trailing edge points (Figure 9). The length of any intermediate chord is the distance between the leading and trailing edges, measured normal to the x-axis and in the xy-plane.

2) From the specification given in the previous section, the twist angle for any given chord can be found. Starting from the chord at the root of the segment, the twist angle for each chord is set to the desired value by rotating the chord around an axis which passes through its 1/4-chord point, parallel to the x-axis (Figure 10). A twist angle is positive if it rotates the chord clockwise when viewed in the positive x-direction.

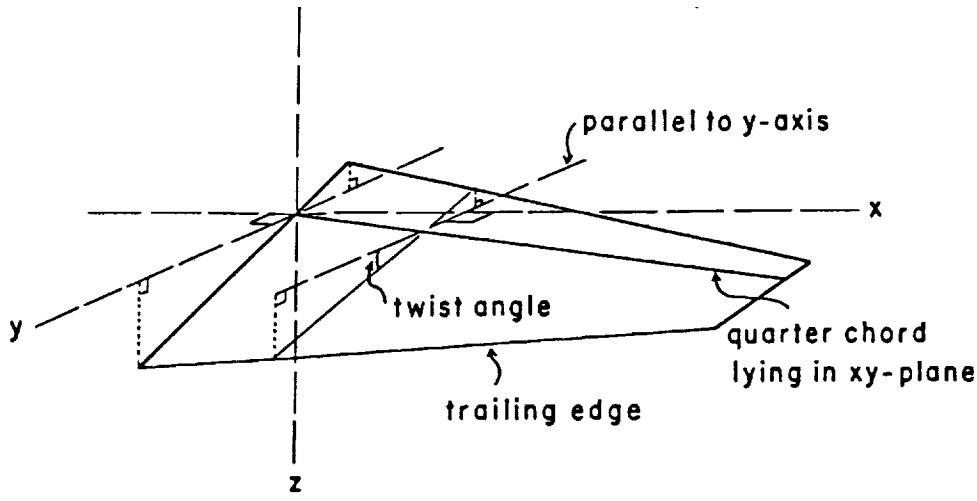


Each chord is perpendicular to the x-axis.
Anhedral angle is set to zero.

Figure 10. Definition of the twist angle.

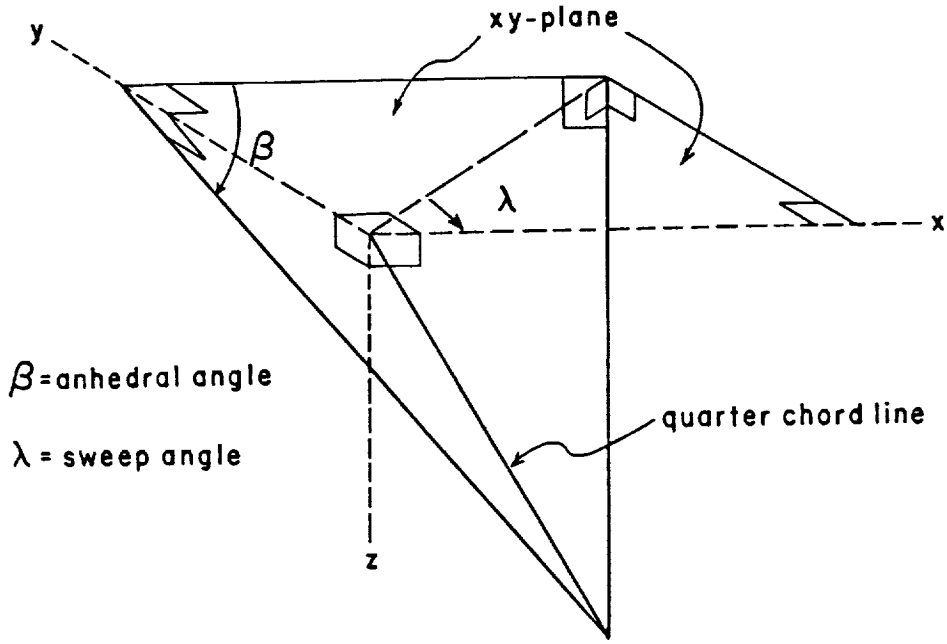


Figure 11. Definition of the anhedral angle.

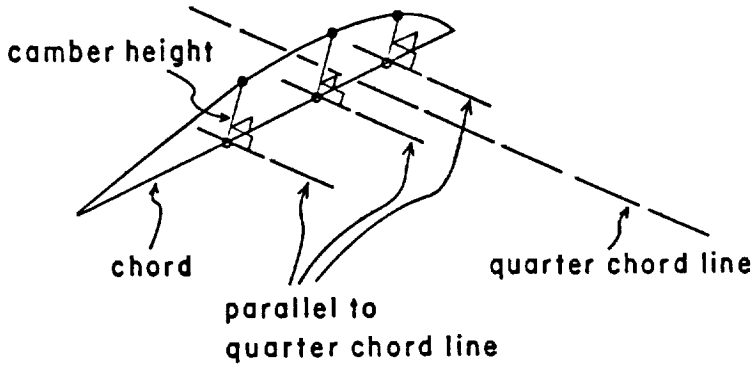


Figure 12. Schematic of camber distribution.

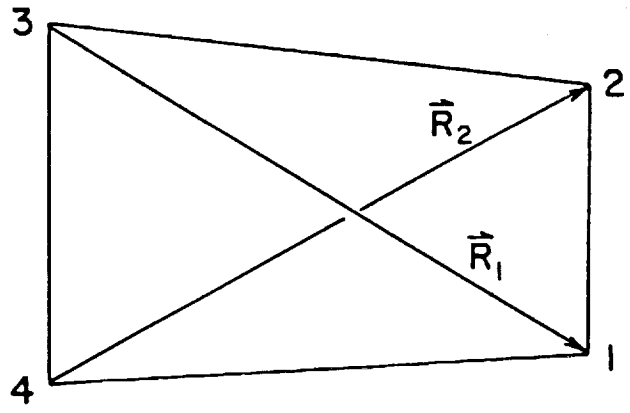


Figure 13. Typical vortex quadrilateral, showing the corner indices and diagonal vectors.

3) The anhedral angle for the segment is attained by allowing the blade to rotate through an angle beta about the y-axis (Figure 11). A positive anhedral droops the segment tip in relation to the segment root.

4) The blade is then cambered as follows. Each specified point along a chord is moved by the amount specified by its camber distribution, in the direction normal to the plane defined by the chord and the segmental 1/4-chord line (Figure 12). This operation is repeated for each chord such that the distance moved, nondimensionalized by the local chord, is identical for corresponding points on all chords of all segments.

5) The first segment is translated from its present temporary location on the xy-plane, without any rotation, until its 1/4-chord point on the root chord is located at (CUTOUT, 0, 0). Each additional segment is put through a pure translation until the 1/4-chord point of its root chord coincides with the 1/4-chord point of the tip chord of the previous segment.

The angles shown in Figure 11 have been greatly exaggerated for the purpose of illustration. Careful inspection will indicate that the anhedral angle is the angle between the x-axis and the projection of the quarter-chord line on the xz plane. In the absence of sweep, it is the angle between the x-axis and the quarter-chord line itself.

## 2.3 Vortex Quadrilateral Lattice Specification and Construction

In addition to the blade geometry parameters, the user also specifies parameters that define the vortex quadrilateral lattice used in the lifting-surface analysis. The user enters the number of chordwise and spanwise intervals along each segment of the lattice along with their chordwise and spanwise lengths (nondimensionalized by local chord and segment span, respectively). The quadrilateral lattice is laid out one segment at a time and then combined in a manner analogous to the blade layout procedure discussed in the previous section. The lattice segments correspond to the blade segments for the following three adjustments.

1) The vortex quadrilateral lattice is displaced 1/4 the chordwise length of the leading edge quads away from the leading edge of the blade segment. For the case of one chordwise interval, this structure places the leading edge of the vortex quadrilaterals at the 1/4-chord line and the blade control points at the 3/4-chord line of the true blade.

2) The root segment is inset from the blade root a distance of 1/4 the width of the quadrilaterals adjacent to the root.

3) The tip segment is inset from the blade tip a distance of 1/4 the width of the quadrilaterals adjacent to the tip.

Once the vortex lattice is assembled, each chord is stretched according to local Mach number in order to transform the compressible problem into the equivalent incompressible problem (see Section 5.1.3). The stretching is in a manner that preserves the airfoil section shape if camber has been specified.

For each quadrilateral, the control point is taken to be the mean of its corner points, and the unit normal at the control point is given by the vector product $\vec{R}_1 \times \vec{R}_2$ of the diagonal vectors (Figure 13). Vector $\vec{R}_1$ goes from corner 3 to corner 1, and vector $\vec{R}_2$ goes from corner 4 to corner 2; the corners are numbered counter-clockwise when viewed from above (in the z-direction), starting at the lower right-hand corner.

## 2.4 Vortex-Lattice Spacing

The issue of the spanwise and chordwise spacing of the bound vortex quadrilaterals is of particular concern when discussing the accuracy that can be achieved in the resolution of loads on the blade. The application of vortex-lattice methods to fixed-wing aircraft has been studied for many years (Refs. 8 and 17), and it has been found that a solution for the loads can be found with essentially arbitrary distributions of vortex quadrilaterals. However, spacing distributions of an arbitrary nature do not lead to smooth convergence as the number of quadrilaterals is increased.

Vortex-lattices with uniform spacing in the chordwise and spanwise directions do exhibit smooth convergence. A drawback of using a uniform-spacing scheme, however, is that the resolution of loads near blade tips or near leading edges sometimes requires a fine mesh of quadrilaterals. When uniform spacing is used, the need to resolve such regions leads to computional inefficiency, since a fine mesh is used even on areas of the lifting surface where the loads vary gradually. "Cosine" spacing has been developed (see, for example, Ref. 8) as a way to avoid this conflict. Cosine spacing distributes the vortex quadrilaterals (and their associated control points) densely near the edges of the lifting surface and then coarsens the spacing away from such regions. The functional form of this spacing rule is such that smooth convergence of the loads is still obtained despite the nonuniform spacing.

The cosine rule was considered for application to this analysis, but it was found that an acceptable balance of accuracy and efficiency could be obtained by relying on uniform spacing. The data correlation runs in Section 5 will provide evidence for this conclusion. Cosine spacing remains a valid option for application to future versions of this analysis.

# 3. SPECIAL FEATURES OF THE WAKE MODEL

## 3.1 Blade/Wake Coupling and Treatment of Multifilament Wakes

The results of Ref. 6 demonstrated that converged free wake geometries could be found for hover wakes with single, fixed-strength trailing filaments; no attempt was made in that work to calculate loads on a rotor blade or to allow the strength of the trailing filaments to evolve during the calculation. Section 1 discussed how this could be done in principle. One of the most significant accomplishments of this effort has been the successful inclusion of these effects in the wake calculation. The code currently has the capability to calculate the blade load that is compatible with a particular wake geometry, given the constraints of the vortex quadrilateral method outlined in Section 2. In this calculation, the wake geometry that satisfies the free wake condition is found while the blade bound circulation adjusts to satisfy the flow tangency condition at each of the selected control points. The wake and blade solutions proceed simultaneously as a single unified calculation.

The remainder of this subsection will discuss how the relaxation procedure in Ref. 6, summarized in Section 1, has been augmented to couple in the effect of blade loads. Some details of the manner in which the blade/wake coupling effects are handled will be provided, as will a discussion of the method chosen for joining the wake to the blade. Finally, the major issues pertaining to the treatment of multiple-filament wakes will be outlined, and some sample results will be presented.

### 3.1.1 Problem Formulation

Section 1 discussed how the relaxation process proceeds for a single, constant-strength filament. To couple in blade aerodynamics, we start with the following general formulation:

$$\vec{q} = f(\vec{x},\vec{\gamma}) \qquad \vec{w} = g(\vec{x},\vec{\gamma}) \tag{12}$$

where $\vec{q} = (\vec{q}_n,\vec{q}_b)$ , the vector of normal and binormal velocities at the wake collocation points, and $\vec{w}$ represents the vector of downwash velocities at the blade control points. The vectors representing the independent variables in the problem are $\vec{x}$ and $\vec{\gamma}$ , the collocation point positions and the bound circulation values, respectively. As discussed previously, The objective of the calculation is to find the values of $\vec{x}$ and $\vec{\gamma}$ for which the dependent variables, $\vec{q}$ and $\vec{w}$ , are nulled.

The desired solution is to be found by successive relaxations; for each relaxation step a matrix of linearized influence coefficients must be found. The linearized influence coefficients include all the effects necessary for the solution scheme to converge in one relaxation step once the wake points and bound circulation values are linearly close to the final answer. This means that making the wake-point position adjustments and the vortex-quadrilateral strength adjustments determined by the influence coefficients will yield the exact answer (if the solution is linearly close). In the current work, the influence coefficient matrices include not only the wake-on-wake effects, discussed in Section 1, but also the effects of the mutual interaction of the wake and the blade. The form of the matrices is as follows:

$$\begin{bmatrix} \\ \Delta\vec{q} \\ \\ \hline \\ \Delta\vec{w} \\ \\ \end{bmatrix} = \begin{bmatrix} \Delta\vec{q}_n \\ \hline \Delta\vec{q}_b \\ \hline \Delta\vec{w} \end{bmatrix} = \begin{bmatrix} Q_{nn} & Q_{nb} & Q_{ng} \\ \hline Q_{bn} & Q_{bb} & Q_{bg} \\ \hline Q_{wn} & Q_{wb} & Q_{wg} \end{bmatrix} \begin{bmatrix} \Delta\vec{x}_n \\ \hline \Delta\vec{x}_b \\ \hline \Delta\vec{\gamma} \end{bmatrix} \qquad (13)$$

Note that Eq. (13) represents a set of linearized equations relating perturbations about some initial state. In Ref. 6, only the submatrices $Q_{nn}$ , $Q_{nb}$ , $Q_{bn}$ and $Q_{bb}$ were calculated since the blade bound circulation values were not degrees of freedom; their introduction requires the calculation of the remaining submatrices. Each of the added submatrices represents a new set of physical effects introduced by the blade/wake coupling. The following discussion focuses on illustrating the nature of these effects on a one-filament/one-blade system. The extension of this method to a system of several blades with multiple trailers is described later.

The submatrices, $Q_{ng}$ and $Q_{bg}$ , represent the changes in normal and binormal velocity at the wake collocation points due to the influence of the blade as noted in Section 1. In Ref. 6, the blade was modelled by a constant-strength bound vortex. Now, as outlined in Section 2, the blade is modelled as a set of vortex quadrilaterals, and for vortices passing near the blades the velocity field will be substantially different. The submatrices, $Q_{ng}$ and $Q_{bg}$ contain the change in crossflow velocities in the wake due to variations in the strength of the individual quadrilaterals. It is easy to see that if the strength of a quadrilateral is altered, the velocity field around the blade will change and there will be a direct influence on the calculated coefficients. There is also another effect that must be included due to the fact that the circulation strength of certain vortex quadrilaterals are also used to determine the circulation strength of the trailing filament (see Section 4). Altering the strength of these quads will alter the strength of the filament which will in turn alter the induced velocities at wake-collocation points during the next step.

The submatrices, $Q_{wn}$, and $Q_{wb}$ represent the effects of perturbations of the wake collocation point positions on the downwash velocities at the blade control points. These are found in very much the same way as the wake-on-wake influence coefficients, the principal difference being that points of evaluation for the influence coefficient computations are not on the filaments themselves, which has the effect of simplifying the programming logic.

The final new submatrix, $Q_{wg}$, contains the changes in downwash at the blade control points due to changes in the blade circulation strengths. This submatrix has two principal contributions: a blade-on-blade component and a wake-on-blade component. The blade-on-blade effects simply reflect the influence of the blade quadrilaterals on the control point downwash; these blade-on-blade influence coefficients are fixed once the geometry of the blade is specified, i.e., they do not have to be updated during the calculation. The wake-on-blade effects are again due to the fact that the blade circulation strengths affect the wake filament strength. These portions of $Q_{wg}$ do need to be updated, since the evolution of the wake geometry will cause the downwash to vary.

### 3.1.2 Blade/Wake Junction

The discussion above is a broad outline of the functioning of blade/wake coupling. One of the particular issues of interest is the precise manner in which the trailing vortex filament is to be joined to the blade. The blade is currently represented by a set of vortex quadrilaterals with the last row of quads lacking a trailing edge vortex line (i.e., the final row consists of truncated horseshoe vortices - see Figure 14). In a conventional vortex lattice treatment, such as might be used in a fixed-wing application, the trailing filaments would be attached to the legs of the horseshoe vortices. Here, however, a different choice is suggested by the requirements of the geometrical scheme with which the first wake element is set up. As noted in Section 1, using the upwind difference scheme to orient the crossflow planes requires that two points (the point of contact with the blade and the first free wake point) and a vector (the velocity vector at the point of contact) be used to set up the first wake element. It was observed that a significant simplification could be achieved if the point of contact with the blade was chosen to be a control point in the last row of blade quads; since the velocity at all control points is found as a matter of course, no special calculations would have to be carried out to set up the geometry of the first arc.

The scheme just described has the drawback of including a very abrupt, nonphysical truncation of the near wake. The actual treatment of this region is substantially more refined, as will be discussed in Section 4.2. However, the truncated lattice model is adequate for the current purpose of illustrating the functioning of the coupled blade/wake analysis.

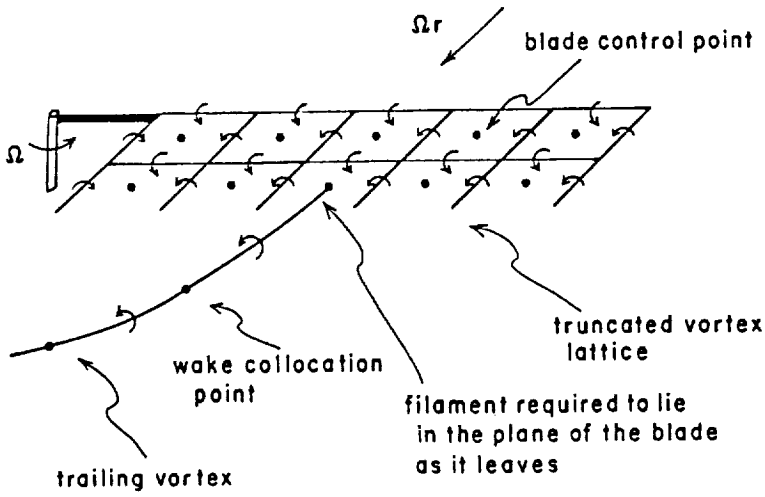


Figure 14. Schematic of the blade/wake junction with a single trailing filament.

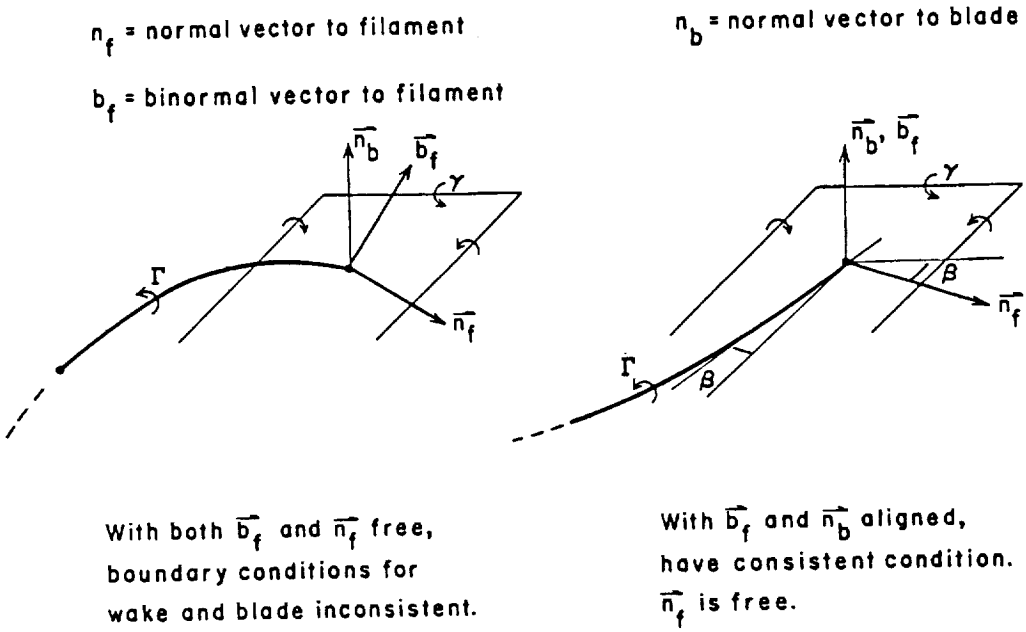


Figure 15. Local geometry of the blade/wake junction.

The choice for the junction of the wake and the blade has a significant effect on the influence coefficient matrix. Note that the point of contact is now both a wake point and a blade control point. The blade boundary condition is that the flow normal to the blade must be zero at every control point; if the control point is the end of a wake filament, it must then be true that the binormal velocity at the first wake point must also be zero (see Figure 15). The effect of these specifications is that a vortex filament must leave the trailing edge in the plane of a blade, but that its inclination to the trailing edge in that plane remains a degree of freedom.

In the formal mathematical treatment, this choice for the juncture between the blade and the wake has removed one degree of freedom from the system; at the juncture control point the velocity normal to the blade and the velocity binormal to the wake filament are one in the same quantity. One of the two must be removed as a degree of freedom from the relaxation analysis. If there are $N$ wake points and $M$ blade quadrilaterals, this has the effect of reducing the dimension of the influence coefficient matrix from $2N + M$ to $2N + M - 1$.

### 3.1.3 Multifilament Wakes

The discussion above is phrased to treat a case in which the wake is modelled by single wake filaments, each trailing from the tip of a different blade. The case of blades having multiple filaments is not fundamentally different, except that the programming logic becomes more involved and the influence coefficient matrix expands significantly. With $K$ filaments per blade, the dimension of the matrix becomes $2KN + M - K$ (note that each junction of a filament with the blade leads to one "redundant" velocity).

The results of some sample problems will demonstrate the success of the multifilament treatment. The calculations to be presented will show converged wake geometries for both one-bladed and four-bladed rotors trailing seven filaments. For each case, three turns of free wake are used, along with two turns of prescribed wake. The inboard filaments use constant 60° segments, while the tip filament trails three 15° arcs followed by constant 45° arcs over the remainder of the free wake (the use of variable arc lengths is discussed in Section 3.2). The root vortex employs a diffused core with a radius of 0.2R, while the other inboard filaments use 0.1R, and the tip filament features 0.02R. In each case, the blades are assumed to be untwisted, with a 6.7 m (22 ft) radius, 0.61 m (2 ft) chord, 7° collective pitch, and a 2.4 m (8ft) cut-out. The vortex layout features 15 quads spanwise and three chordwise, all uniformly spaced. These parameters were chosen for the purpose of performing representative calculations; succeeding sections will address the proper choices to be made for actual rotors.

Many of the major features of typical hover wakes appear in the one-bladed wake geometry results shown in Figure 16. First, note that the

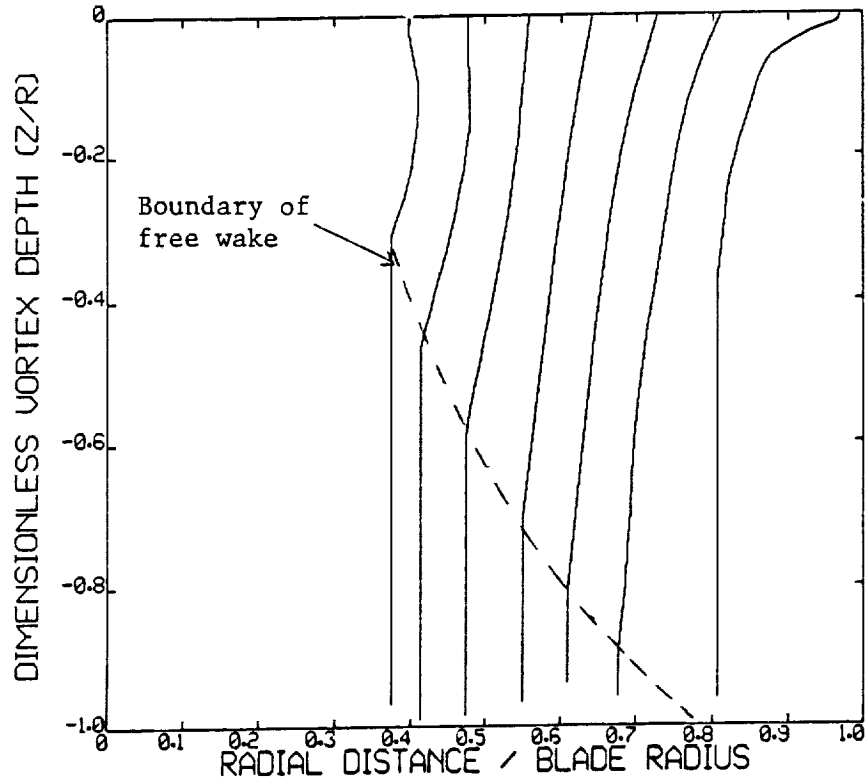


Figure 16. Wake geometry of a representative one-bladed rotor.

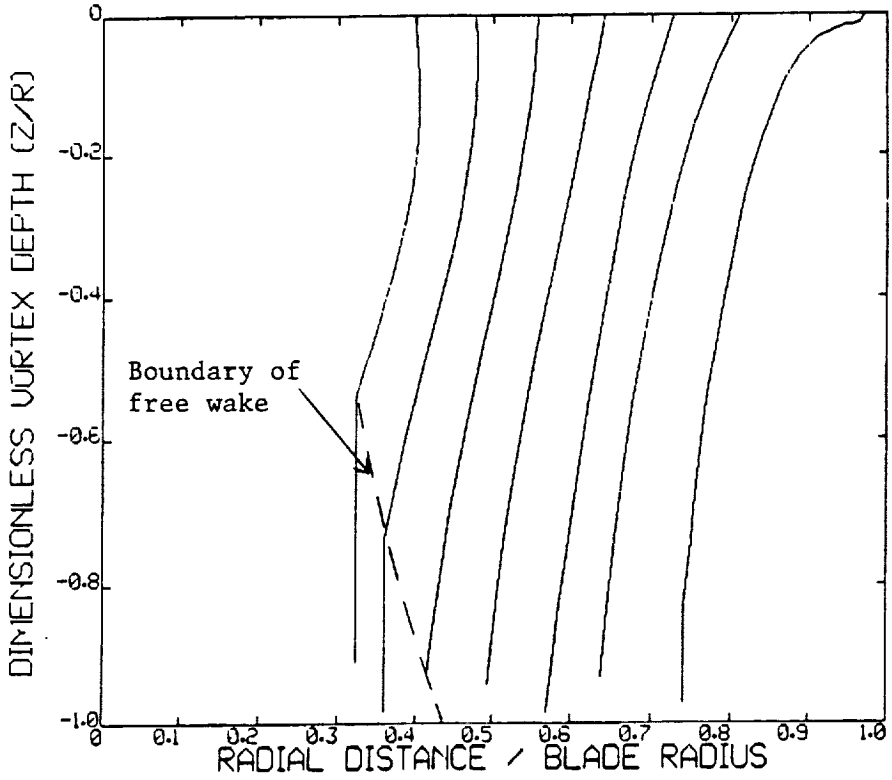


Figure 17. Wake geometry of a representative four-bladed rotor.

wake contracts at the root as well as at the tip. This is to be expected, inasmuch as the behavior of the wake of the blade is likely to be similar to that observed in fixed-wing wakes, which also feature contraction at both wingtips. Also notice the increase in downwash in the wake reflected by the tendency of the last free point in the wake to be washed down farther for outboard filaments; the maximum downwash occurs for the filament just inboard of the tip.

Replacing this one-bladed rotor with a rotor with four blades yields a qualitatively similar result (Figure 17). Notable differences include a higher general level of downwash, as well as somewhat higher contraction near the tip and root, a trend consistent with the higher thrust on the four-bladed rotor.

## 3.2 Azimuthal Variation of Arc Size

As was noted in the discussion of fundamental principles earlier, the wake relaxation in this solution method proceeds in what is essentially an Eulerian frame defined by curvilinear coordinates along each filament. In these calculations, the collocation points are not associated with any particular fluid particles, unlike the Lagrangian time-stepping approach used in many previous free wake analyses (Refs. 1 and 2).

This circumstance also opens up a new set of possibilities for the relaxation approach used here. In Lagrangian calculations, the azimuthal spacing of the particles is rigidly tied to the time step chosen for the calculation. One vortex element is trailed from the blade at each time step, and there is strong computational motivation to minimize the number of steps around the azimuth so as to minimize the computation time. However, large time steps lead to coarse wake structure that is incapable of resolving fine-scale events like blade-vortex interaction. Lagrangian methods thus have a built-in conflict between computational efficiency and accuracy of resolution of the flow.

The relaxation method used here enjoys far more flexibility. Because of the independence of the method from any fixed time step, the collocation points may be laid out in unequal azimuthal spacings. This circumstance permits points in the wake to be closely spaced near the rotor blades, where detailed resolution of the wake structure is likely to be important, while far wake turns use very coarse spacing (as few as four elements per turn) to minimize CPU time.

Two simple but representative model problems suffice to illustrate the potential importance of this capability. Figure 18 shows the trajectory of a tip filament from a simple one-bladed rotor. In this example, the blade was given only two free filaments, with the tip filament having two turns of free wake consisting initially of sixteen 45° curved elements. This baseline run was then modified by subdividing the first arc into smaller sub-arcs: first, two 22.5° arcs; then, three 15° arcs; and finally, four 11.25° segments. In each case, the rotor collective pitch was adjusted to keep the thrust

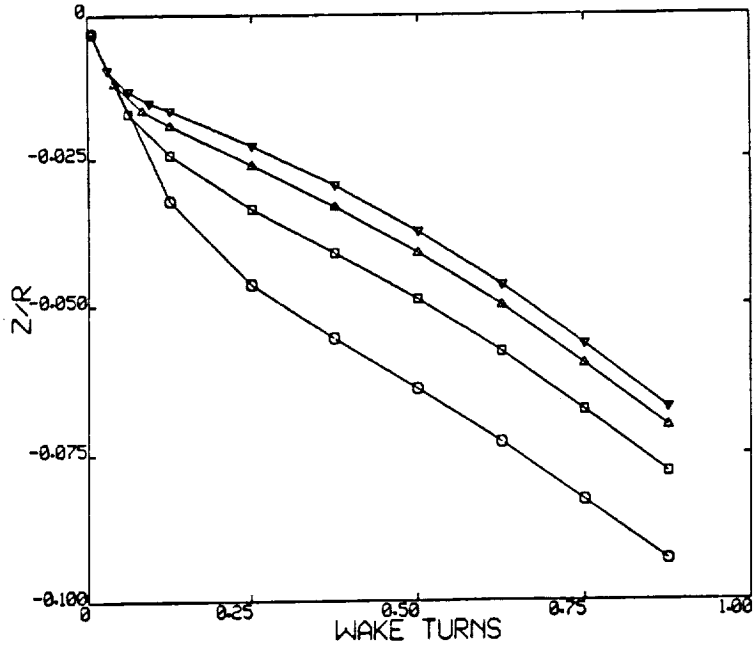


Figure 18. Tip vortex trajectory using refined modelling of the first trailing element (calculations performed on a one-bladed rotor; thrust held fixed).

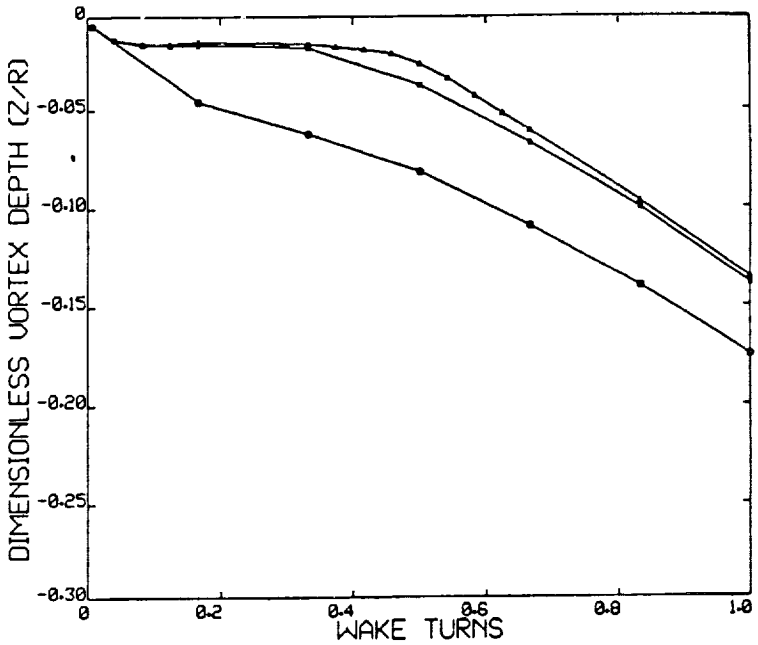


Figure 19. Tip vortex trajectory using refined modelling of elements near the following blade (calculations performed on a two-bladed rotor; thrust held fixed).

coefficient on the rotor constant. The required changes in collective pitch were never more than a tenth of a degree, so the flow tangency condition at the blade/wake connection points did not vary significantly between cases. As Figure 18 shows, the trajectory of the tip filament moves upward as the first element is refined. As is evident, the filament converges to a final position as the number of sub-arcs increases. The total vertical displacement in this refinement process is only a few percent of rotor radius, but this is a significant fraction of the original displacement below the rotor plane. In rotors with large numbers of blades where blade vortex interaction is an issue, such refinement can have an important effect on blade load predictions.

The fundamental phenomenon at work here is that the vortex experiences a steep gradient in downwash as it moves away from the blade. The velocity induced by the bound circulation falls off rapidly, but if the filament is modelled with large arcs, it will be "thrown down" in a direction tangent to the chord line of the blade section from which it is trailed. As is clear from the baseline case in Figure 18, the entire filament will be displaced downward. As smaller arcs are introduced just aft of the blade, the downwash gradient will be resolved and the filament will relax smoothly to its proper trajectory.

Clearly, the proximity of filaments to following blades is an issue of great importance in resolving blade-vortex interaction. For this reason, it is desirable to use a large number of arcs on those portions of filaments passing near blades. An example of this procedure is shown in Figure 19. Here, a two-bladed rotor has been used, again with only two filaments trailing from each blade. The baseline case for the tip filament uses 45° arcs; subdividing the first element into four arcs as above shifts the filament upward. Then, the filament is further refined in the vicinity of the following blade by subdividing the two elements immediately adjacent to the blade. As is evident, the trajectory in the vicinity of the blade changes significantly, though it converges once again to the unrefined arc trajectory as it moves further downstream. This sample problem again demonstrates the power and flexibility inherent in the relaxation solution method used in this effort.

### 3.3 Optimization Possibilities and Accuracy Studies

In the course of developing the hover wake analysis, various schemes for optimizing the wake velocity calculations were explored. This investigation was deemed necessary because the code is very computationally intensive, with a large portion of the calculation being spent on wake vortex element velocity calculations. A very promising, and relatively simple approach was identified to improve efficiency. However, in the end, this effort was not actually implemented due to limitations of time and cost, and because other areas associated with guaranteeing good performance of the basic code were deemed to have higher priority.

The need for high accuracy in the hover problem dictates that all filaments near the point of evaluation be curved vortex elements (BCVE's). In

a full wake representation in hover the important nearby elements are all associated with nearly the same azimuthal location, being on filaments immediately above and below, and to either side, and those elements on the same filament adjoining the point of evaluation. Curved elments properly account for close proximity position and curvature effects which are particularly important in the delicate velocity balance that controls the filament positions in hover. Of the total number of elements used in the wake calculation, relatively few of these are in this region near the point of evaluation, and curved elements are already an efficient way to handle this region. Therefore, the significant opportunities for optimization involve how the remaining large majority of elements in the far field of the point of evaluation are handled.

Two possible optimization strategies were studied. The first involves the use of much larger curved elements in the far field of a given element. Although this approach appears to have potential for traditional Lagrangian time-marching calculations, its implementation in the hover code would be extremely difficult, and might well require the reformulation of the entire logic structure of the code. The problem centers on the fact that the far field of every element is different and requires a different set of far field elements. To locate larger elements would require selectively skipping some collocation points while using others further apart to define the larger elements. To do this would make the already complex logic of determining the influence coefficients far more complicated. Furthermore, as discussed in Section 3.2, variable collocation point spacings are being used in the code to provide higher resolution in certain regions (e.g., close blade/wake interactions) and lower regions in others (e.g., farther down in the wake). This practice, which is desirable for many other reasons, would cause even greater difficulty in properly implementing large curved far field elements. For these reasons, the possibility of using large curved far field elements to improve efficiency was abandoned.

A second possible approach to improving efficiency is to use the same number of elements, but utilize a simpler element model for the far field region. At distances of several element lengths away, the accuracy advantage of curved elements becomes inconsequential, particularly in terms of the cumulative effect of many such elements for which the residual errors may largely cancel. Timing studies show that straight-line elements may be as much as three times faster than curved elements, and vortex particles may be as much as six times faster. In a previous study (Ref. 7), the accuracy and efficiency of straight-line elements relative to curved elements was studied, and the accuracy of an individual vortex particle relative to a straight-line element was also investigated briefly. For the present consideration, the vortex particle was chosen as the primary focus of study.

Vortex particles are attractive for several reasons. They are functionally the simplest possible vortex element and they offer the greatest advantage in computational speed. Because of their functional simplicity, spatial derivatives of the vortex particle velocity field are still relatively simple analytical functions (unlike curved vortex elements). This fact raises the possibility that the influence coefficient calculations might be done in

large part analytically, rather than by purely numerical means. The use of a faster far field element, and the potentially significant simplification of the influence coefficient calculations, could substantially improve the efficiency of the hover analysis code.

A study of the accuracy of filaments composed of vortex particles was undertaken (Ref. 18). Vortex ring and linear filament configurations were studied. In this work the vortex particles were located at collocation points with their direction vectors tangent to the filament; rather than positioned in the lines between collocation points. It was found that a filament composed of vortex particles produced significantly lower net errors than the particles taken individually. Typically at a distance from the filament equal to the particle spacing, errors of no more than a couple of percent of swirl velocity were encountered. At larger distances the accuracy improves very rapidly. At a distance equal to half the particle spacing, errors of about 10% of swirl velocity are encountered, and these get worse very rapidly at closer distances. At the distances cited the errors are a minimum directly over a vortex particle spacing and are largest roughly halfway in between.

In previous work (Ref. 7), the out-of-plane velocity component above a vortex ring was found to be a sensitive indication of vortex element accuracy when comparing straight-line and curved vortex element. The out-of-plane velocity component is important for the vertically stacked filament turns in the wake of a hovering rotor. The same ring accuracy tests were performed for a ring of vortex particles. Remarkably, vortex particles perform significantly better than straight-line elements in this regard, typically better by almost a factor of ten. This occurs because the effective interpolation of the Biot-Savart integrand by the vortex particle method is more accurate for this velocity component than is the linear geometric interpolation provided by straight-line elements. Vortex particles actually capture much of the local curvature effects that straight-line elements completely miss.

The main conclusion of this study is that vortex particles work remarkably well for vortex filament velocity calculations. Because their accuracy is quite good except very near the filament they are an appropriate choice for efficient far field elements. A hybrid representation using a BCVE near field and a vortex particle far field would lead to a substantial savings in computer time.

Interestingly, there seems to be little justification for using straight-line elements for vortex filament calculations. Previous work has shown that the treatment of filament curvature effects provided by curved vortex elements is necessary to evaluate the velocity field to a consistent level of accuracy on and near the filament. Straight-line elements cannot account for the curvature effect when relatively near the filament. On the other hand, vortex particles are quite accurate at distances somewhat greater than an element length from the filament, and do a good job picking up residual curvature effects. The velocity field can be computed accurately and efficiently by the combination of a few sophisticated curved elements in the near field and a large number of the simplest possible elements representing the remainder of

the vortex elements. Straight-line elements are inaccurate in the near field and inefficient in the far field.

Given these interesting results, a related study was undertaken to examine the accuracy of discrete filaments in representing vortex sheets. A discrete filament representation is certainly accurate when the distance from the sheet to the point of evaluation exceeds the local spacing between filaments. The question is how close can the point of evaluation be and still get good results without going over to a continuous sheet model. Since the local sheet contribution is essentially two-dimensional at points close to the filament, accuracy simulations were performed using two-dimensional point vortices to simulate a continuous two-dimensional sheet.

The simulation of a flat sheet of infinite extent with an infinite row of point vortices shows that if the point of evaluation is located one vortex spacing above the sheet the resulting error is very small, typically less than 1%. When the point of evaluation is located at one half of the vortex spacing, the errors are 10% or less. Tangential velocity errors are greatest directly over a point vortex or midway between two vortices; the errors at these locations are nearly equal but of opposite sign. The vertical velocity error is a maximum at the one-quarter and three-quarter locations between the vortices; the error is zero directly over a vortex and over the midpoint between vortices. The percentage errors quoted should be considerably smaller for a hover wake because many additional sheets and vortices are present whereas the error is a velocity increment of fixed size associated with the nearest few discrete point vortices. In the hover flow field this velocity increment will be a much smaller percentage of the overall velocity due to the many additional sheets and vortices. The conclusion is that a continuous sheet correction is not needed to account for the interaction between inboard sheets, provided each sheet is represented by enough filaments so that the point of evaluation is more than half a filament spacing away from the sheet. This is not a serious restriction since a reasonable number of filaments are needed to resolve the shape of the vortex sheet. However, for the point of evaluation on the sheet or filament (self-induction case) a different approach involving a cut-off distance is used (see Section 4.2). Since it turns out that the logic of the influence coefficient solution method would be considerably complicated by cross-coupling between filaments, it is fortunate that the sheet correction can be confined to the case of vortex sheet self-induction. This simplicity also improves the efficiency of the overall code. Part of the reason this can be done involves the nature of the ideal hover solution itself, where the sheets are regularly spaced and do not intertwine. The same simplification would not be possible for a forward-flight analysis.

Finally, as a point of interest, some other work on modelling filaments and sheets with simple discrete elements (such as vortex particles) is mentioned (Ref. 18). This work involves building in core or shear layer velocity distributions into these discrete elements and thereby avoiding singularities. The denominator of either the vortex particle or point vortex expressions can be grouped to contain the variable $r^2$, where $r$ is the distance from the element point to the point of evaluation. Replacing $r^2$

with $r^2 + \varepsilon^2$ in the denominator produces a realistic vortex core or shear layer velocity field in the vicinity of the filament or sheet provided the element density is sufficiently high. For the filament, $\varepsilon$ is the length scale for a realistic vortex core size and a relatively realistic velocity distribution results. This velocity distribution gives solid body rotation at the core center. For the sheet, the shear layer thickness is several times larger than $\varepsilon$, with a linear shear profile near the centerline. To resolve these core or shear layer regions with good accuracy requires an element spacing equal to, or just slightly smaller than, the quantity $\varepsilon$. When the spacing equals $\varepsilon$, the velocity errors are typically less than 20%, with errors this large occurring only when the point of evaluation is in the relatively unimportant low velocity region near the center of the core or shear layer. These results suggest a simple way in which protection from singularities during close encounters can be built into these simple element models.

# 4. SPECIAL ISSUES IN WAKE TREATMENT

The discussion to this point has focussed on the broad principles of the current analysis and has left open several issues of considerable importance. A description of these features has been postponed to this point since the topics to be discussed in this section are interrelated and are best presented together. The topics to be discussed are: the determination of the strength and release points of the free filaments in the analysis, the modelling of the near wake immediately downstream of the blade, and the selection of the core properties of the free filaments, i.e., the core radius and the cutoff distance.

## 4.1 Strength and Release Points of Free Filaments

As discussed in the previous sections, the current analysis models the wake of a hovering rotor as a set of curved vortex filaments. In reality, the wake leaves the blade as a continuous vortex sheet, though the tip region typically begins to roll-up rapidly a short time after being trailed. The ideal approach to the simulation of the wake and its roll-up would be to use freely distorting, curved sheet elements that could smoothly merge into the appropriate trailing wake. In practical terms, however, the only realistic tools for use in this type of hover analysis are vortex filaments. Local sheet corrections for such filaments are possible, but they have not been implemented in the current version of this code.

Given that filaments must be used, it appears desirable to use a large number of them so that the full sheet would be correctly modelled in the limit. However, the problems attending the use of a large number of point vortices to simulate a two-dimensional sheet have been well documented (Ref. 19). The analogous difficulties in three dimensions are: first, very short elements must be used to resolve the roll-up of the vortices, leading to long computation times; and second, that the individual filaments must be smoothly amalgamated as roll-up proceeds. These issues, particularly the second, cannot currently be resolved except by ad hoc approximations.

In the face of these difficulties the traditional approach, and the one adopted here, has been to use a relatively small number of discrete filaments (no more than 10) to model the wake of each blade. Fortunately, the typical wake structure of conventional rotors is well suited to this approximation. As suggested by Figure 20, drawn from Ref. 20, the wake of most rotor blades resolves itself into a strong tip vortex and a more diffuse inboard sheet which can be successfully modelled by several discrete filaments with appropriately chosen cores (see Section 4.3 for more discussion of this issue). When using such models, care must be taken to choose the filament strengths and release points so as to preserve as much of the original character of the continuous wake sheet as possible.

In terms of the wake strength, the first imperative here is to conserve circulation in the trailing wake. In the hover analysis this is accomplished

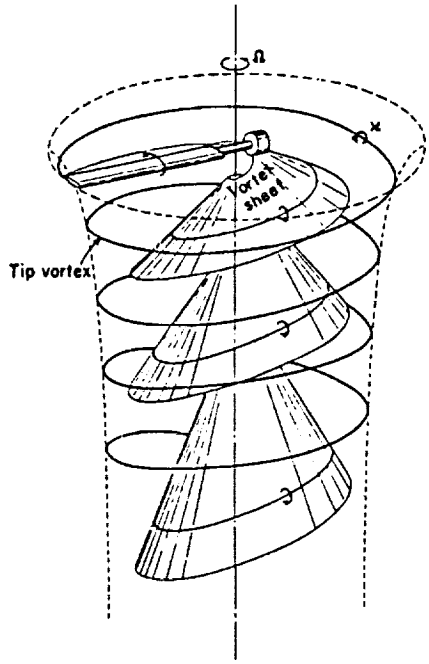


Figure 20. Schematic of the typical wake structure of a hovering rotor

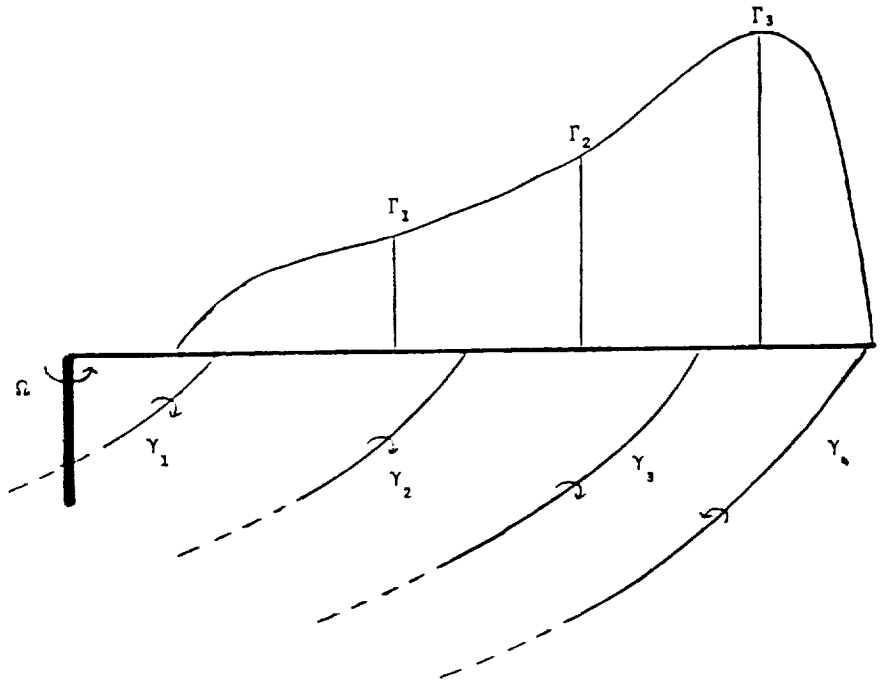


$$\gamma_1 = -\Gamma_1 \qquad \gamma_2 = \Gamma_1 - \Gamma_2 \qquad \gamma_3 = \Gamma_2 - \Gamma_3 \qquad \gamma_4 = \Gamma_3$$

Figure 21. Scheme for the calculation of the strength of trailing vortex filaments from the bound circulation.

by following a few simple rules in defining the filament strengths, rules which are best illustrated by example. Figure 21 shows a schematic of a typical load distribution on a rotor blade and a wake assumed to consist of four free filaments. In practice, the user has the option of choosing the boundaries of circulation zones 1-4. The strengths of the filaments trailing from these regions are then defined as shown in the figure.

In general, this approach leads to a wake with a single strong tip vortex, several relatively weak inboard filaments, and a strong root vortex. There is some degree of arbitrariness available to the user in such cases in the choice of the circulation zones. For example, capturing the maximum blade bound circulation in the tip vortex (a feature observed in many experimental wake surveys) relies on the user selecting the correct boundary for the tip region. This can be done reliably for most conventional rotor designs after some exposure to typical spanwise circulation distributions.

The selection of vortex-filament release points does not present a serious difficulty for most conventional rotor designs. Untapered rotors with moderate twist usually have a distribution similar to that sketched in Figure 21, with a peak between 0.8R and 0.9R. Tip vortices may be trailed from near the tip itself, and wake solutions tend to be relatively insensitive to the locations from which the inboard filaments are trailed. In several important cases, the positioning of trailers is not so straightforward. As will be shown in Section 5, rotors with tapered, highly twisted blades often feature circulation distributions which peak much farther inboard than conventional designs (as far in as 0.5R - 0.6R). The absence of a sharp bound circulation peak near the tip on such rotors implies that a different treatment of the trailing wake is required for these designs.

To provide a consistent physical basis for the choice of trailer locations, approaches similar to that described for fixed-wing wakes in Ref. 21 may be used. In this reference, a model originally developed by Betz (Ref. 22), is described that conserves the centroid of vorticity in the trailing wake during the roll-up of wingtip vortices. Though this particular conservation law is strictly applicable only to two-dimensional flows, the velocity fields generated by such a wake model have been shown to yield good agreement with experiment. Positioning the rolled-up wake in accordance with the demands of centroid conservation removes a degree of arbitrariness from the process of locating the wake filaments.

An appeal to analogous principles may be made for the rotary wing hover calculations performed here. Assume, for a moment, that the wake of a rotor blade can be treated as an uncontracting helical sheet of small pitch. If it is desired to take a strip of this sheet and model it as a discrete vortex, it is important to know where to locate this filament. Consider taking just the first turn of this helical strip; the question can be posed in terms of finding the radius of the vortex ring that best represents this individual turn (this assumes that the vertical gap between the ends of the turn of wake can be safely neglected).

Batchelor, on p. 521 of Ref. 23, derives an integral invariant for axisymmetric distributions of vorticity. He shows that if $\sigma(r)$ describes the radial distribution of vorticity in an axisymmetric field, then the quantity $\sigma(r)r^2$, integrated radially, is invariant over time. Applying this principle in a piecewise manner to the helical strip described above, it is clear that the radial centroid will be conserved if the strip is replaced by a filament of radius $\bar{r}$ and strength $\Gamma$, where $\bar{r}$ and $\Gamma$ are determined as follows:

$$\Gamma = \int_{r_1}^{r_2} \sigma(r)dr \tag{14}$$

$$\bar{r}^2 = \frac{1}{\Gamma} \int_{r_1}^{r_2} \sigma(r)r^2 \, dr \tag{15}$$

In the context of the hovering rotor problem, the bound circulation distribution is divided into sections by the user, as shown in Figure 21. The radial distribution of trailing vorticity from each section is the function $\sigma(r)$ shown in Eq. (14) above. The hover analysis assigns the filament strength based on Eq. (14) and also computes the centroid location $\bar{r}$. The user has the option of allowing filament release points to move toward the appropriate centroids during the calculation. Since the motion of filament release points can retard convergence significantly, it is often better to fix the release points and then rerun the calculation if the chosen locations are too far from the final centroid locations. (For further details, consult the discussion concerning the input variable ICENT in Section 3.2 of the CDI-EHPIC Users Manual.)

## 4.2 Treatment of the Near Wake

In a performance analysis of this type, a careful treatment of the discrete representation of the blade/wake junction is required. It is essential that the relative positioning of the wake filaments and quadrilateral control points be such that both wake-on-blade and blade-on-wake influences are calculated correctly. In the present work, the filament was chosen to leave from a blade control point because this is the point where the blade induced velocity field is known in the vortex quadrilateral representation. The downwash must be correctly specified at the first point on the filament, in accordance with the upwind difference scheme described in Section 1, which includes the tangent vector at the first point as an unknown. This does not handle wake-on-blade effects correctly for two reasons: 1) most of the wake structure near the blade is omitted because a full vortex sheet is not in place; and 2) the blade sees filaments leaving

from control points rather than from the legs of the horseshoe vortices which are truncated. Some additional feature is required to ensure adequate treatment of near wake effects.

In this analysis, the blade/wake junction is handled with an overlap scheme. In this scheme, the wake-on-blade effects are accounted for by extending horseshoe trailers back into the near wake region and truncating them farther behind the blade. Beyond the truncated point the free wake filaments pick up the rest of the wake-on-blade contribution. The truncation point is far enough behind the blade that the transition between wake models is smooth and accurate. The wake-on-wake and blade-on-wake effects are left unchanged in the near wake. The wake filaments are extended up to the blade with the horseshoe trailers truncated at the blade trailing edge. Thus, two different wake representations are used in the same (overlap) region depending on whether the point of evaluation is located on the blade or in the wake. This approach has the added advantage of allowing the number of free wake filaments to differ from the number of horseshoe trailers behind the blade which greatly improves computational efficiency. A somewhat similar approach has been used successfully to merge a multi-filament forward flight wake with a blade loads code under commercial sponsorship.

The current overlap scheme extends the trailing legs of the vortex quadrilaterals on the trailing edge back along curved arcs, as shown in Figure 22. The overlap angle can be chosen by the user. The user may also choose the number of curved elements at the top of each free filament to be deleted from the wake-on-blade calculation to avoid double counting the near wake effects. It is recommended that the number of elements deleted be such that the azimuthal extent of the deleted free wake is equal to that of the extended trailers (i.e., with 15° of overlap and 15° elements on each free filament, one element should be deleted from each filament).

Experience with this analysis has indicated that it is important not to use an excessive amount of overlap if accurate performance predictions are to be obtained. The curved trailers that extend back from the blade remain at the radius from which they were trailed. Since wake contraction is neglected, large overlap angles will lead to inaccuracies in the wake-on-blade contributions. This is particularly true at high thrust, where contraction of the wake is rapid. For these reasons, it is recommended that no more than 7.5° to 15° of overlap be used. (See Appendix A for further discussion of the proper extent of the overlap region.) Such overlap regions have lengths of roughly two to five blade chords for typical rotor designs, and so provide an adequate buffer between the blade and the free wake for most operating conditions.

### 4.3 Cut-Off Distance and Core Size for Filaments

The vortex filament dynamics have been analyzed by integrating the Biot-Savart law over the vortex filaments. This integration is done numerically in the present analysis by breaking the filaments up into simpler vortex elements (BCVE's in this case) whose integrations can be done in closed form, and

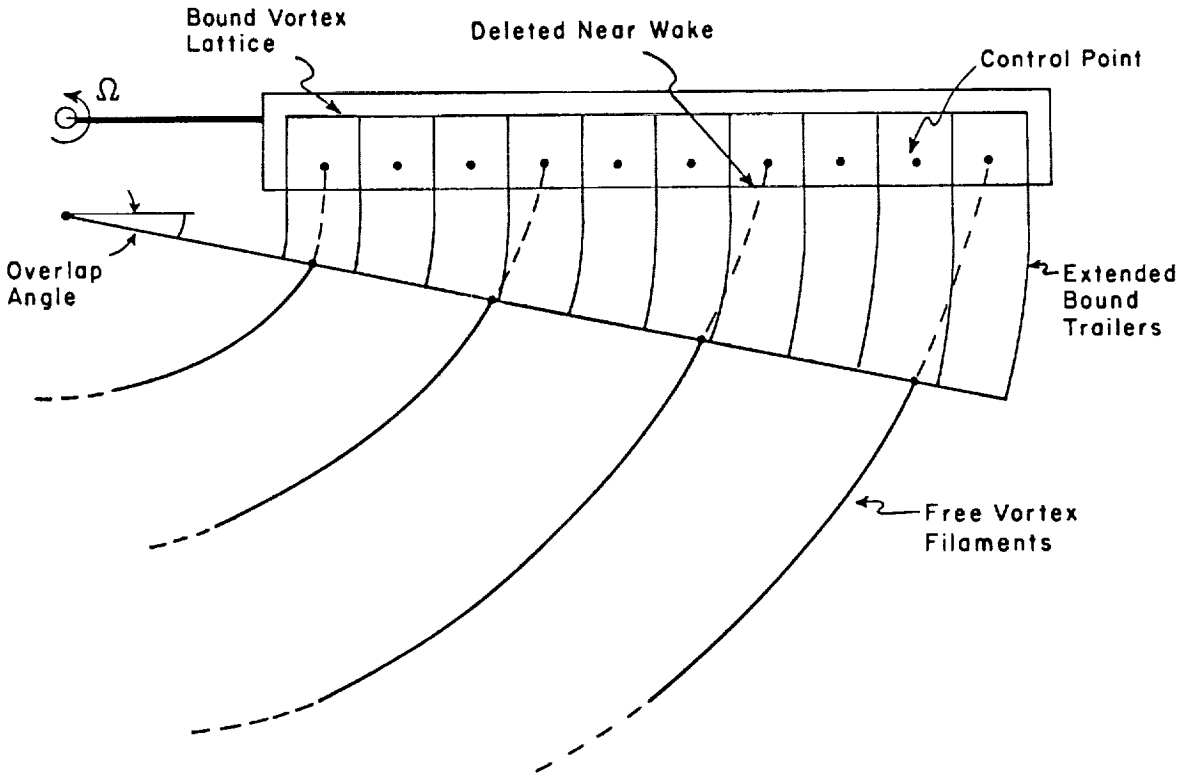


Figure 22. Schematic of the overlap treatment of the near wake.

summing all the element contributions. If a finite-strength infinitesimal vortex filament is used, then the Biot-Savart integration is logarithmically singular when the point of evaluation is placed on the curved filament itself. This logarithmic singularity of self-induced velocity is associated with the local curvature of the filament at the point of evaluation. This problem is avoided by stopping the integral at a cut-off distance on either side of the point of evaluation. This approach is handled by a special self-induction vortex element called the SIVE. The current choice of cut-off distance is obtained from an asymptotic analysis that gives results in terms of local core size (length scale) and the net swirl and kinetic energy content of the vortex core that must actually exist at the center of the filament. The energy content and core size can be obtained from a detailed knowledge of core structure or, in the case of a tip vortex, by a knowledge of the blade load distribution using a recently developed method (Ref. 24). In the current hover analysis a version of the latter approach is used.

The filaments leaving the blade of the hovering rotor will play one of two roles in the downstream wake structure. Filaments near the tip and root will roll-up into relatively concentrated tip and root vortices. Filaments in between will typically remain in a vortex sheet which may distort but does not roll up. The hover analysis finds the position of the resultant tip and root vortices and the sheet filaments, but does not handle the roll-up process itself.

There are several reasons for not resolving the roll-up process numerically in the present code. First, at least for relatively conventional rotors, there is no reason to resolve the roll-up in detail because the vortex is well formed by the time it passes the following blade. A more basic reason for not handling detailed roll-up within the context of the current analysis is that the resulting twisted braid of vortex filaments would not be extendable into the far wake region below the free wake. The far wake analysis needs simple helical filaments and cannot accommodate such filaments if a secondary intertwining structure is present. The amalgamation of a braid of tip vortex filaments into a single filament further down in the wake is a possibility, but would be very difficult with the current influence coefficient scheme. Other reasons for not resolving the roll-up numerically involve concerns about resolution accuracy, numerical efficiency, and robustness of convergence of the code.

It is believed that an analytical treatment of this process using a Betz roll-up type model provides the best results within the context of the current method. In this approach, each portion of the trailed vortex sheet is assumed to roll-up around the sheet centroid location (see Section 4.1). The portion of the sheet that rolls up into a tip vortex is determined by the location of the maximum circulation for most conventional rotor designs. The hover analysis uses the resultant filament having the strength defined by Eq. (4). This filament leaves the blade at the centroid location of this portion of the sheet. As discussed in Section 4.1, in the case of the hover flow field, the centroid radial location is calculated based on a circular sheet model rather than on a linear sheet model (as would be used behind a wing). The cut-off distance used for this resultant filament is based on the method of Ref. 24,

which utilizes blade loading information to define the cut-off distance parameters.

Two ways of relating cut-off distance for the tip vortex to blade loading are described in Ref. 24. In either case, the advantage of such an approach is that a knowledge of the detailed structure of the vortex core is not required. This simplification is achieved by a control volume application of integral conservation laws between the blade and the resulting vortex. Such an approach can be used because the cut-off distance really depends on integrated quantities. The cut-off distance can always be expressed in the form $\ell_c = Ks$, where $K$ is a constant, and distance $s$ is the width of the vortex sheet that rolls up to form the tip vortex. The constant $K$ is an integral quantity that can be expressed in either of two ways. It can be related to an integral of the circulation distribution in the vortex sheet or to the nondimensionalized net induced drag on the part of the blade within the distance $s$. At present, the results for $K$ are available only for the case of inviscid roll-up. Some work has been done to extend these results to include the effect of a turbulent core, but this work is not complete at the present time. Note that $K$ depends on the normalized distribution of drag or circulation, but not on the absolute amplitude. The amplitude effect is accounted for by the net tip vortex circulation which appears in the formula for the self-induction vortex element. For all elliptically loaded tips $K \simeq 0.13$; for linear tip loading $K = 0.15$. In practice, $K$ will be fairly close to the elliptical loading value.

The present version of the hover analysis uses the formula $\ell_c = Ks$. As the solution evolves, the changes in the tip sheet centroid position (which is the tip vortex release point) are calculated, and the user may specify that the tip filament be moved to follow it. However, the constant $K$ uses an assumed value, typically that for an elliptic distribution, as the solution evolves. There are several reasons for this simplification. The influence coefficient logic to determine changes in $K$ would add considerable complexity. Also, since $K$ is currently known only for inviscid roll-up, and its functional dependences in a more advanced real flow model are as yet unknown, the most reasonable approach is to leave this parameter as an external input. Once a solution has been converged, a new $K$ can be computed for the tip load distribution and a refined solution obtained using the new value. This can be done externally because the solution is fairly insensitive to changes in $K$, since only the logarithm of cut-off distance (with other terms added) appears in the SIVE velocity formula.

In terms of the tip vortex self-induction velocity, the most sensitive parameters are the length $s$ and the net circulation. The latter effect is included within the present solution framework. Currently, the distance $s$ is an input to this analysis; care must be taken that the calculated values of $s$ are consistent with the original input. If they are not, the computation may be rerun with the calculated value of $s$ to improve the consistency of the model.

The self-induced velocity of the inboard filaments is also handled by a cut-off distance approach, but in this case the cut-off distance is based on

the fact that the filaments represent a vortex sheet. It can be shown that a curved segment of vortex sheet experiences a self-induced velocity, similar in principle to that experienced by a vortex core. A planar, constant strength curved vortex sheet can be shown to have a cut-off distance equal to half the sheet width. The velocity computed using the SIVE element and this cut-off distance applies at the center of the sheet. If the sheet cross-section is rotated 90°, as if the sheet now lies on a cylindrical surface, then there is a change in the cut-off distance. However, the logarithmic dependence in the SIVE formula makes this change insignificant, particularly for the sheet orientations that actually occur in hover. Therefore, in the analysis, the half-width cut-off distance formula is used for inboard filaments. This sheet cut-off distance is quite a bit larger than the tip vortex cut-off distance, (roughly a factor of five). The self-induction of a strip of inboard sheet is, therefore, weaker than that of a tip vortex formed from a sheet of the same width and net strength. This is to be expected since a sheet is a more diffuse structure than a rolled-up tip vortex.

A choice for tip vortex core radius that is consistent with the approach for cut-off distance just described is to pick the radius to equal the distance from the inboard edge of the tip vortex sheet to the centroid of the trailing vortex distribution. Once again, an initial estimate of the tip vortex core size may be chosen and then checked against the calculated location of the centroid. For the inboard filaments representing the trailing sheet, the proper choice is half the width of the portion of the sheet that the filament represents (this coincides with the inboard filament cut-off distance). Uniform vorticity cores are assumed for all filaments.

# 5. PERFORMANCE ANALYSIS

## 5.1 General Outline of Performance Evaluation

### 5.1.1 Thrust and Induced Torque Evaluation

As described in the previous sections, the relaxation solution generates the appropriate bound circulation values to satisfy the flow tangency condition at each of the blade control points. Given these bound circulation values and a complete description of the velocity field at the blade, the Joukowski law may be used to compute the forces on the rotor. First, the local downwash is evaluated at the midpoint of each side of the vortex quadrilaterals on the blade. The orientation of each leg provides the direction of the local bound circulation vector, and taking the cross product of this with the local velocity (including the free stream) yields the force vector on the leg in question. This procedure is repeated for each quadrilateral on the blade, the results are summed and resolved to provide the thrust and induced drag.

The lifting surface analysis currently implemented includes no allowance for post-stall loss of lift. Thus, the analysis may generate unrealistically high lift coefficients on some portions of the blade in high thrust cases. For most blade designs, such overprediction will occur on the inboard portions of the blade, which are, in general, less important to the performance prediction than the tip regions. In future versions of the analysis, however, it may be desirable to include explicit limitations on the sectional lift; this topic is discussed further in Section 6.

The induced torque may be found by taking the force vector on each individual leg and crossing it with a vector from the rotor shaft to the midpoint of the leg. The component of the resulting moment vector parallel to the shaft represents the induced torque contribution, which is also computed for each blade quad and summed.

Thus, given the solution for the bound circulation and the downwash, the determination of thrust and induced torque is quite straightforward. However, this computation procedure is valid as described only for blades with no thickness immersed in incompressible, inviscid flow. Thickness effects on lift are neglected entirely in this calculation, and it is assumed that the effects of viscosity and thickness on drag can be successfully treated by using empirical, two-dimensional drag coefficients coupled with an appropriate look-up and interpolation scheme. The table look-up procedure used here is described in the next section, while the effects of compressibility on thrust and induced drag is treated thereafter.

### 5.1.2 Profile Drag Computations

During the computation of the thrust on the blade, the incremental thrust on each chordwise quad at a given radial station is summed to give the spanwise thrust distribution. The appropriate nondimensionalization yields the local lift coefficient at each section. Using the $c_\ell$ so obtained along with the local Mach number, two-dimensional airfoil section data are consulted to provide the local profile drag coefficient. In this manner, compressibility, viscosity and thickness effects are incorporated into the profile torque at each section.

Many rotor designs feature gradual transitions between different airfoil sections at different radial stations; in such cases, section properties at intermediate stations are found by interpolating in radius from the drag coefficients computed for each of the bounding airfoils at the specified lift coefficient and Mach number. The routine, as currently constituted, can accommodate up to five different airfoils on the blade, with drag coefficients for up to fifty $c_\ell$'s and ten Mach numbers.

Although this procedure is conceptually quite straightforward, and has been used in nearly all previous computational performance analyses for rotors, there are a number of limitations that must be clearly understood. A first and very practical constraint is that airfoil section data are often not available for the full range of lift coefficients and Mach numbers required for the calculation. Also, the lifting-surface analysis that yields the section $c_\ell$ does not include separation, and so will often produce unrealistically high lift coefficients. For most graphical lift/drag polars, lift coefficients above 1.0 are likely to produce separation and a dramatic rise in drag coefficient, especially at high subsonic Mach numbers. In such cases, it is difficult to define the appropriate drag coefficient for, say, a $c_\ell$ of 2.0 as generated by the lifting-surface analysis.

The procedure used to deal with this situation was as follows: for lift coefficients above stall (defined as the point where lift curve slope begins to decrease) an "effective angle-of-attack" was computed for the $c_\ell$ based on the lift curve slope below stall. Then, using separate $c_\ell$ vs $\alpha$ and $c_d$ vs $\alpha$ curves, an approximate $c_\ell$ vs $c_d$ polar for post-stall conditions was constructed. (The user must construct such $c_\ell$ vs $c_d$ tables for each of the airfoils to be used on the rotor; they become part of the input to the performance analysis.) This process is clearly an approximation though it does capture the gross trends in profile drag increase for large lift coefficients.

Another limitation of this approach is that it assumes that two-dimensional coefficients are applicable to what can be highly three-dimensional flow. For example, near the tip of a rotor, three-dimensional effects become quite pronounced, notably the well-documented phenomenon of compressibility drag relief. Consequently, profile drag is probably overstated in this region. This uncertainty regarding the applicability of two-dimensional coefficients for both the post-stall and near-tip regimes

may be a contributing factor to some of the performance correlation difficulties described in previous research, as well as later in this report. However, it appears that for many configurations of importance, this treatment is quite satisfactory even at high rotor loadings.

### 5.1.3 Compressibility Effects

Compressibility has an important effect on rotor performance at tip Mach numbers above roughly 0.5. Some of this effect is captured by the inclusion of Mach number dependence in the look-up tables used for profile drag coefficients. However, compressibility also has a significant impact on the lift generated by airfoils at specified angles of attack, and so its influence on thrust and induced power must be considered as well.

For two-dimensional thin airfoils, treatments like the Prandtl-Glauert correction to lift curve slope are acceptable methods for including Mach number effects. However, when handling three-dimensional lifting-surface calculations, transformations that are similar in spirit but more elaborate in detail must be invoked. Kocurek, in Ref. 25, uses a transformation of the entire space surrounding the rotor in generating a correction for compressibility. Here, a more restricted transformation of the blade geometry is used, one based on the local Mach number at the radial stations along the span.

It is assumed that the flow around a given blade section can be found using the compressible potential equation

$$\beta^2 \phi_{xx} + \phi_{yy} + \phi_{zz} = 0 \qquad \beta^2 = 1 - M^2 \qquad (16)$$

where $M$ represents the local Mach number at a particular radial station. (For this discussion, $x$ denotes the streamwise flow direction (positive downstream); $y$ lies along the radius (positive out); and $z$ is positive up.) Using a transformation whereby $x$ is replaced by $\beta x_i$, $y$ by $y_i$, and $z$ by $z_i$ changes the above equation to:

$$\phi_{x_i x_i} + \phi_{y_i y_i} + \phi_{z_i z_i} = 0 \qquad (17)$$

This equation governs the incompressible flow around a transformed blade in which the blade chord is stretched by a factor of $\beta^{-1}$ (note that $\beta$ varies along the radius). The transformed blade is used in the relaxation analysis to find the converged wake geometry and the associated loads on the blade. Then, the loads must be corrected in accordance with the geometrical transformation to obtain the thrust and torque on the rotor in compressible flow.

The transformation outlined above leaves the bound circulation, the downwash on the blade, and the dimensional lift per unit span the same for both the compressible and incompressible problems. Thus, the thrust and induced power computed for the transformed, incompressible problem are the same for the original, compressible problem. However, because of the stretching of the airfoil chord, the lift coefficient for any section for the compressible problem is greater by a factor of $\beta^{-1}$ than the lift coefficient in the incompressible problem. The $c_\ell$ found in the relaxation solution must be increased by this factor before entering the drag coefficient look-up table.

### 5.1.4 "Performance Sweep" Calculations

A very useful feature of the relaxation solution method used in this analysis is that once a converged solution has been achieved for a given collective pitch, solutions for other values of collective may be obtained without restarting the entire calculation. The analysis has the ability to introduce changes in collective (or in blade twist) into converged solutions and then to re-relax the coupled wake/blade system from that point. The re-relaxation usually only requires four or five steps, which is roughly one third of the initial relaxation time for a typical calculation. In most cases, a collective increment of roughly 1° is acceptable. Using this approach, the entire operating curve of a given design can be determined in roughly one-third of the time required for the same number of individual calculations. Twist distributions can also be altered in a similar manner to explore the possible effects of design changes or torsional deflection of the blade on performance. In sum, the ability to carry out such "performance sweeps" is not only a useful feature that enhances efficiency, but also foreshadows applications to such issues as systematic perturbations in design to optimize performance.

## 5.2 Representative Model Problems for the Coupled Solution

The inclusion of the features described above completed the basic development of the EHPIC (Evaluation of Hover Performance Using Influence Coefficients) computer code. This section presents a brief summary of results of representative model problems that demonstrate the functioning of the major features of the EHPIC code. It is of interest to see how the possible choices of input parameters affect the performance results. For current purposes, the discussion will focus on three major options: the choice of chordwise and spanwise spacing for the vortex lattice on the blade; the number of trailing filaments in the free wake; and the extent (i.e., the number of turns) of free wake used. The sample calculations to be presented in discussing these points cannot be construed to give definitive guidance in the choice of these parameters for all possible rotor configurations. However, they serve to narrow the range of such choice considerably while illustrating the major features of the performance evaluation at work.

The numerical experiments will be conducted using a "generic" rotor, featuring untapered blades with 8° of linear twist. The blade's aspect ratio was chosen to be 15, and the rotor is assumed to be operating in incompressible flow. Single-bladed rotors are used for several of the demonstration calculations, though multiple-bladed rotors are also used to demonstrate the breadth of applicability of the code.

The baseline case chosen was a run featuring four free filaments with two turns of free wake on the inboard filaments and three on the tip filament. The initial vortex lattice used 30 quadrilaterals spanwise and one chordwise. The overlap region was chosen to be 15° of azimuth, and, unless otherwise specified, only one-bladed runs were performed.

### 5.2.1 Vortex-Lattice Spacing

As noted in the discussion in Section 2, several previous researchers have used lifting-surface models for rotorcraft applications. No hard-and-fast rules have emerged from that work to define the quadrilateral density needed to achieve a specified accuracy. Kocurek (Ref. 25) noted that for representative calculations, acceptable convergence of the predicted load was achieved with two chordwise quadrilaterals, along with 30 spanwise segments. To investigate this issue with the current analysis, the generic rotor described above was set at a collective pitch of 12° and its performance was calculated using 30 uniformly spaced, spanwise quads with from one to four chordwise quads, also uniformly spaced. Then, the number of chordwise quads was fixed at one and the spanwise quads were run up from 10 to 50 in steps of 10.

Figures 23 and 24 show the convergence trends of the performance of the generic rotor. These results are representative of the trends observed in simulations of practical rotor designs. Figure 23 shows that for blades with thirty spanwise quads, the blade loads are essentially converged with four chordwise quads. However, the solution for one chordwise quad is within 1% of the converged result in both thrust and torque, indicating that good accuracy may be achieved with relatively simple lattices, at least for untapered blades. Figure 24 illustrates the convergence of loads as the number of spanwise quads is varied with one quad used chordwise. Here, the solution using 30 quads brings the predictions to within 1% of the converged results.

### 5.2.2 Effect of the Number of Free Filaments

For these comparisons, a two-bladed version of the generic rotor described above was used. In each case the wake featured two turns of free wake on the inboard filaments and three and a half free turns on the tip filament. Runs were made at a collective pitch of 12° for four, six and eight filaments. The filaments were trailed from the blade so as to keep roughly constant spacing from root to tip. To obtain true, smooth convergence of the load with an increasing number of filaments, it would be necessary to lay out the filaments with considerably more care. The

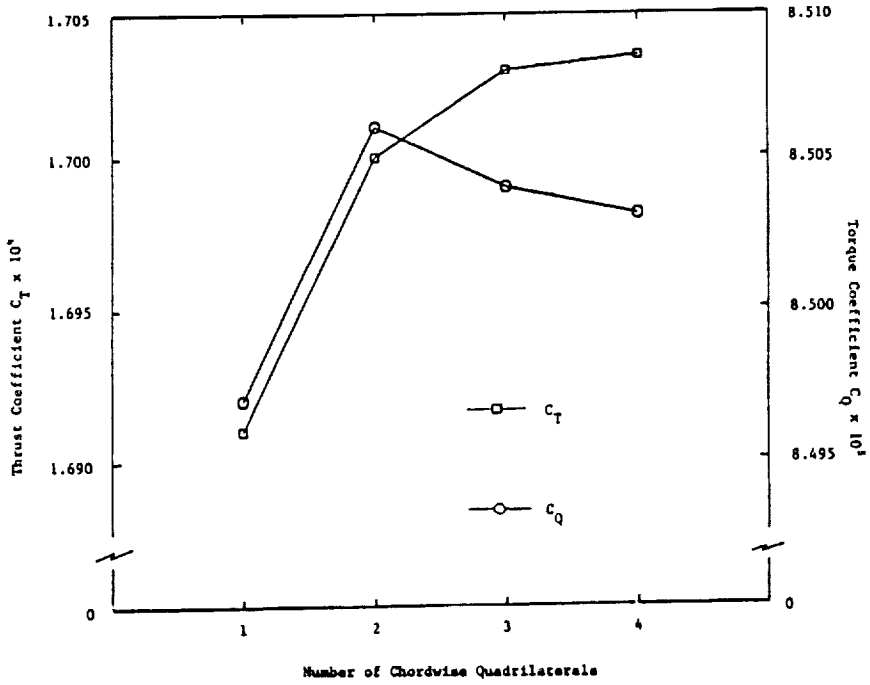


Figure 23. Performance of a one-bladed rotor as a function of the number of chordwise quads.

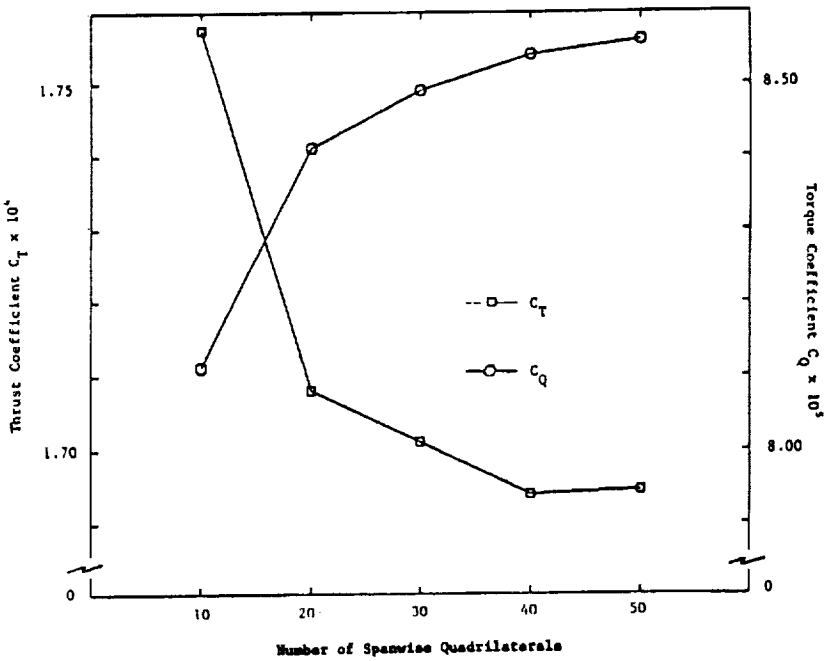


Figure 24. Performance of a one-bladed rotor as a function of the number of spanwise quads.

objective of this exercise was to discover the approximate magnitude of likely changes in the predicted performance for representative cases.

The predicted thrust coefficient on the rotor was found to be 0.002877, 0.002890 and 0.002905 for four, six and eight filaments, respectively. The predicted torque coefficients for these same cases were, respectively, 0.0001721, 0.0001722 and 0.0001725. Clearly, the changes in performance for fixed collective are small. The implication of these results is that relatively simple wake models will often be adequate for obtaining good approximations of rotor performance. However, the small changes observed here will not be realized in all cases, so it is recommended that relatively large numbers (i.e., six to ten) of filaments be used unless computation time is a serious constraint.

### 5.2.3 Effect of the Number of Free Turns

The baseline performance for a one-bladed generic rotor was, as shown in Figure 23, a $C_T$ of 0.001691 and a $C_Q$ of 0.0008497. This result was found to be invariant to four significant figures as long as a minimum of three free turns of wake were used for the tip vortex with two free turns for the inboard filaments. This corresponded to a free wake that extended roughly 1.25 rotor radii below the disk. Such a choice is adequate for lightly loaded rotors like the sample case run here, but, as noted in Appendix C, a conservative choice is to move the free wake/far wake junction roughly a full rotor diameter below the disk. Performance results are almost invariably insensitive to further extensions of the free wake, even for the most highly loaded cases.

## 5.3 Performance Correlations with Experimental Data

To enhance confidence in the generality of the EHPIC code, a wide variety of rotor systems were chosen for experimental correlation studies. The details of the rotor systems are given in the subsections below, along with the references from which the data were drawn. Appendix C gives useful background information on the choices of important computational input parameters. The input parameters for the runs described below are discussed in that Appendix.

### 5.3.1 NACA TN-4357 Full-Scale Rotor

Reference 26 contains thrust and power data for a full-scale, two-bladed rotor. The blades were untapered and had a radius of 8.17 m (26.8 ft) and a chord of 0.58 m (1.91 ft). The blades featured 8° of linear twist and were tested at tip Mach numbers between 0.28 and 0.66. The blades also used the NACA 0012 section across the full rotor span.

These tests were performed at the NACA/Langley Whirl Tower, an installation that featured a tower height of 12.8 m (42 ft). Thus, the ratio of height-to-rotor diameter was 0.78. Typically, for values of

h/D less than unity a ground effect correction must be applied to performance data. No such corrections were noted in Ref. 26, therefore, to insure compatibility, the computational predictions were adjusted using the method outlined on p. 130 of Ref. 27. This was the only data set for which such corrections were judged necessary.

Figure 25 shows the agreement achieved for two tip Mach numbers: 0.28 and 0.62. The agreement is generally favorable over the entire range of performance surveyed, although the computations appear to be slightly pessimistic in power needed for a given thrust. This may suggest that a more refined ground effect correction should be applied.

### 5.3.2 NACA TN-2277 Full-Scale Rotor

Reference 28 gives thrust and power information on a three-bladed rotor with partial span taper. The rotor had a radius of 5.8 m (19 ft) with a constant chord of 0.32 m (1.04 ft) out to 55% of radius, tapering to 0.17 m (0.56 ft) at the tip. The NACA 23015 airfoil section was used across the entire span. The blades used 8° of linear twist.

Such tapered rotors typically produce substantially different load distributions than untapered designs of the same radius; the presence of taper tends to shift the load inboard on the blade, resulting in an altered trailing vortex distribution. For this reason, it was of interest to see if the CDI-EHPIC code could successfully predict the rotor's performance.

Figure 26 shows the correlation achieved for tip Mach numbers of 0.31 and 0.62. Again, the correlation is good even at very high thrust levels.

### 5.3.3 Boeing Vertol Company CH-47B Main Rotor

Performance data on this rotor is found in Ref. 29. This rotor was a three-bladed design with a 9.15 m (30 ft) radius and a constant chord of 0.64 m (2.1 ft). The blades featured 9.14° of linear twist and used a BV 23010-1.58 section across the entire span. The computational predictions are shown along with the data in Figure 27. As is evident, the results are quite satisfactory.

### 5.3.4 Boeing Vertol Company YUH-61A Main Rotor

The performance of a more modern rotor is described in Ref. 30. The data comes from OGE whirl tower tests of the Boeing Vertol UTTAS design. This four-bladed rotor had an untapered planform with a radius of 7.47 m (24.5 ft) and a chord of 0.59 m (1.92 ft). The tip Mach number was 0.66, and the blades featured a nonlinear twist distribution (with a total twist of 9.6°). The blades used three different airfoils across the span: the

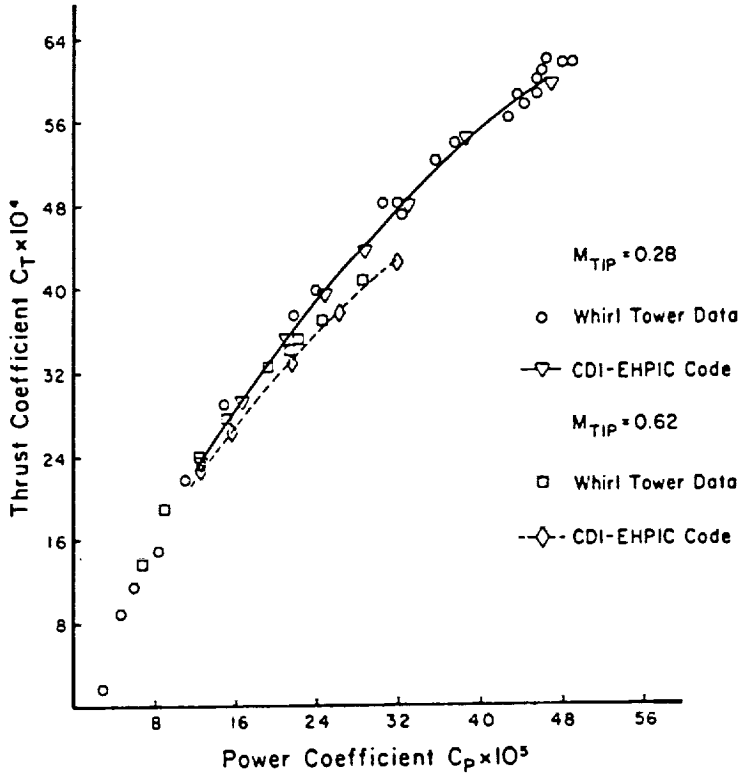


Figure 25. Performance predictions for a two-bladed full scale rotor (data from NACA TN4357).

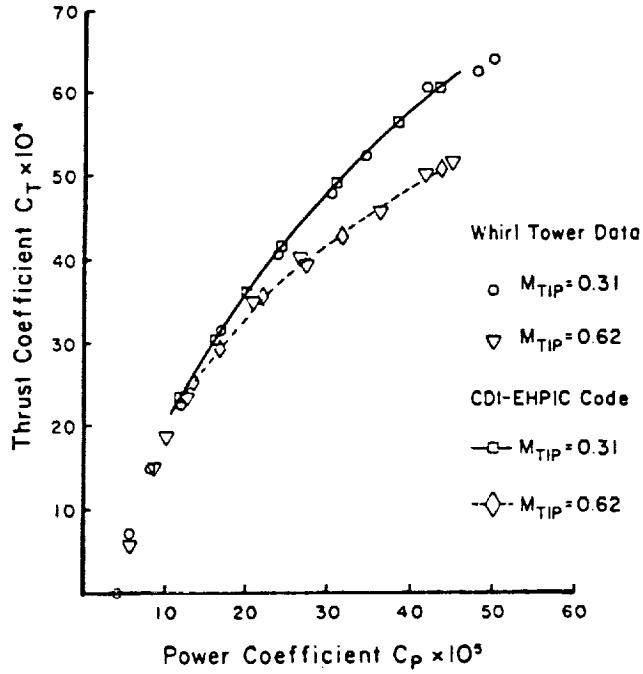


Figure 26. Performance predictions for a three-bladed full scale rotor (data from NACA TN2277).

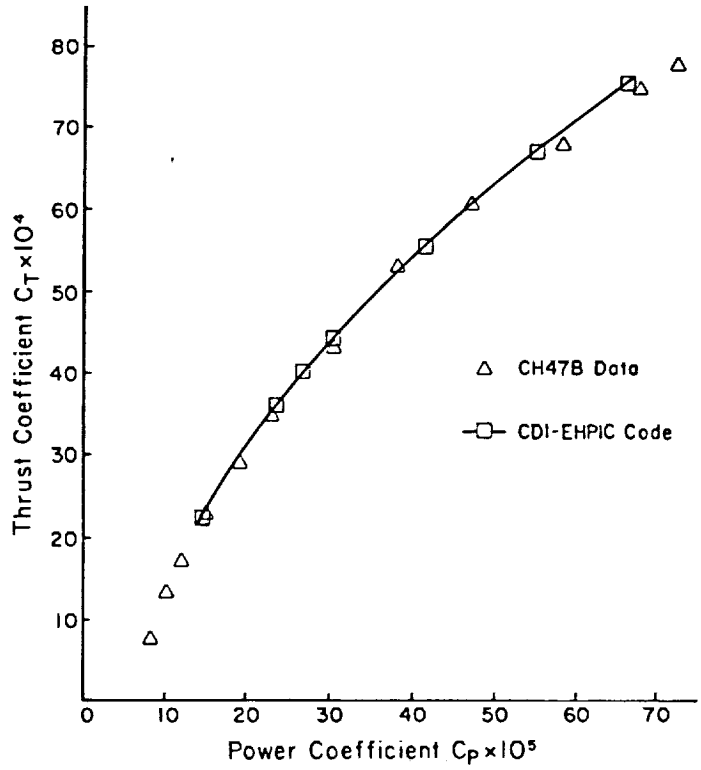


Figure 27. Performance predictions for the CH-47B main rotor.

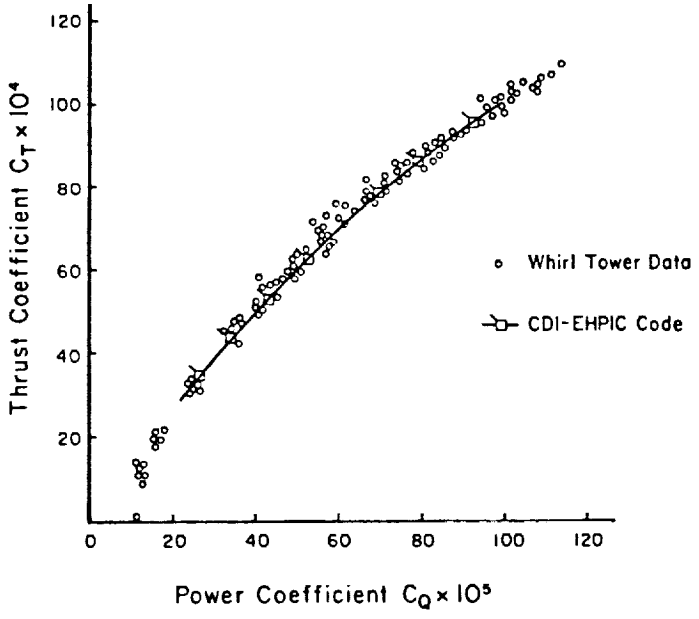


Figure 28. Performance predictions for the YUH-61A main rotor.

VR7 out to the 75% radius station, blending into the VR8 at 91% and finally to the VR9 at the tip. The favorable correlation shown in Figure 28 is an indication of the code's ability to successfully predict performance for modern rotors using advanced airfoil sections.

### 5.3.5 Advanced Technology Rotor Designs

The results discussed above have demonstrated successful correlation with a variety of rotors at a wide range of twist and taper distributions and with a number of different airfoil sections. These calculations serve to validate the basic free wake approach used, as well as the treatments chosen for the compressibility effects and the near wake. It is now of interest to examine the performance of the model when dealing with still more advanced designs. Two contemporary rotors will be examined: the main rotor of the XV-15 research aircraft and a variant of the Advanced Technology Blade version of the XV-15 design. Predicting performance for these rotors presents a particular challenge for current methods. Reference 31 documents the poor correlation achieved using existing prescribed wake methods to predict performance for the variant of the ATB with swept/tapered tips. Reference 31 attributes this to the mismatch between the data base from which these prescribed wake methods were drawn and the actual design of the ATB rotor. Because of the design compromises necessary to produce acceptable forward flight performance in the tilt-rotor, both the XV-15 and ATB designs have very large values of built-in twist (roughly 40° distributed in a nonlinear fashion across the span). Such twist levels were well outside the range contained in the data bases supporting the prescribed wake performance methods cited in Ref. 31. The difficulties encountered in using such codes highlight the attractiveness of using a free wake analysis for analyzing novel rotor designs.

The results of performance predictions for the XV-15 main rotor are shown in Figure 29 (the data are drawn from Ref. 32). This rotor was a three-bladed design, with roughly 40° of built-in, nonlinear twist and a nearly constant chord. The radius of the rotor was 3.81 m (12.5 ft) and the tip Mach number was 0.69. Each blade featured five NACA 64-class airfoils across the span. The agreement shown in Figure 29 indicates a high degree of success in matching the measured full-scale data. This is encouraging evidence of the breadth of applicability of the code, particularly in light of the bound circulation distribution on the blades, which, as Figure 30 shows, is very different from the distribution typically observed on the more conventional designs, such as the CH-47 rotor (Figure 31).

Figure 32 shows the circulation distribution on the square-tip variant of the Advanced Technology Blade (ATB) version of the XV-15 rotor. The ATB results are different from either the XV-15 or the CH-47 distribution. The CH-47 displays the characteristic shape of untapered rotors with moderate twist; low blade loading inboard with a gradual rise to a high peak just inboard of the tip. This fits with the most commonly-used trailing wake model; a single, strong tip filament with a relatively

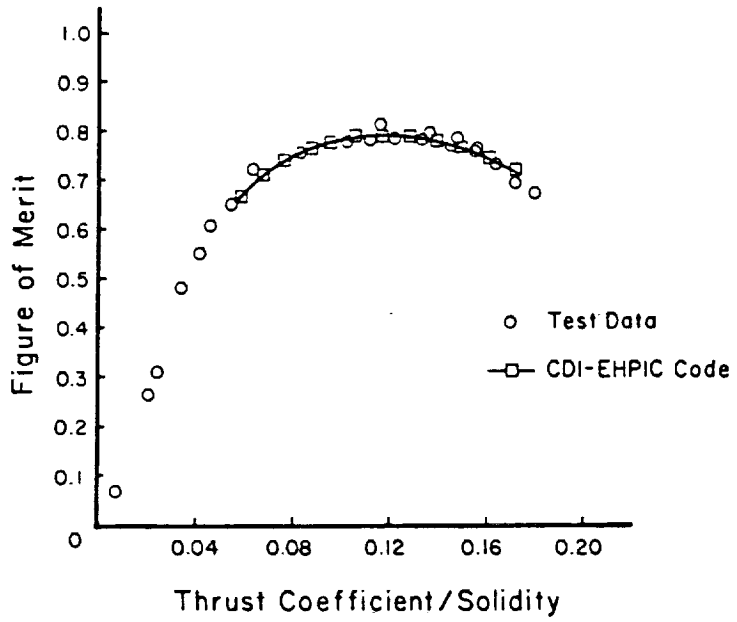


Figure 29. Performance predictions for the XV-15 rotor.

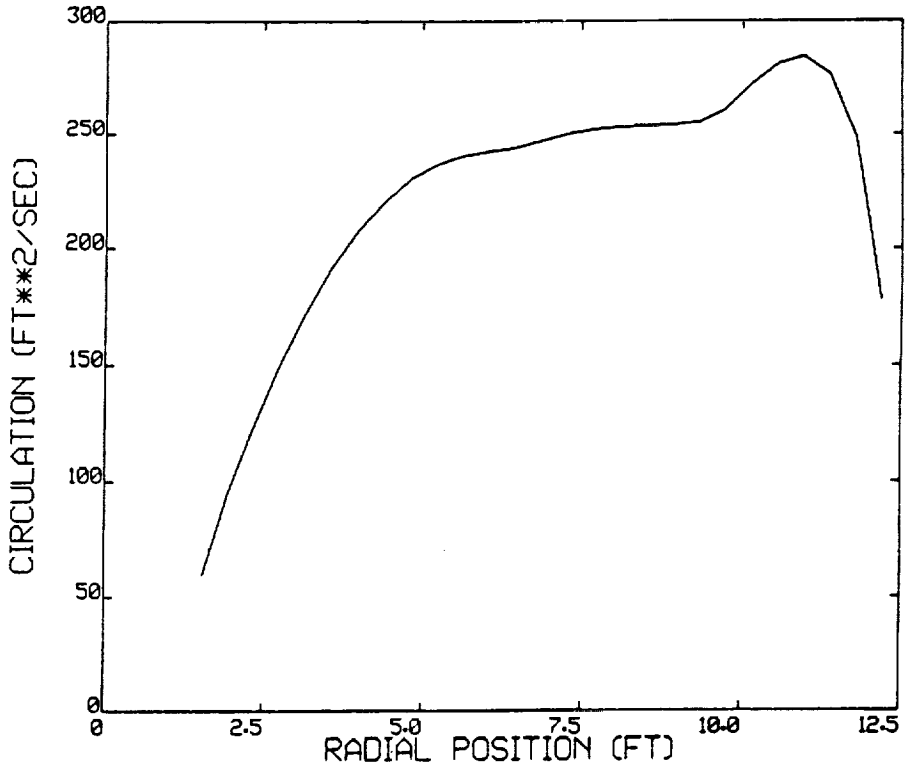


Figure 30. Circulation distribution of the XV-15 for $C_T = 0.0113$ .

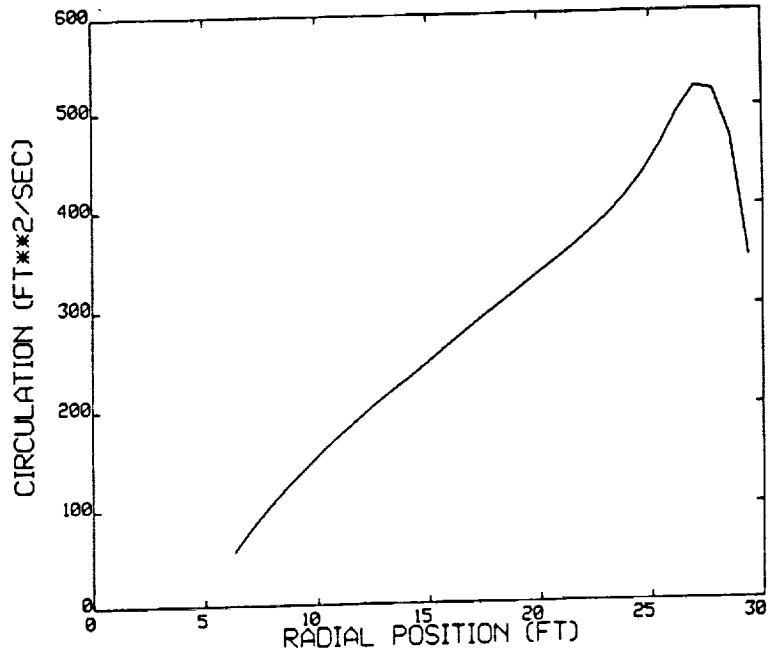


Figure 31. Circulation distribution of the CH-47B for $C_T = 0.0068$ .

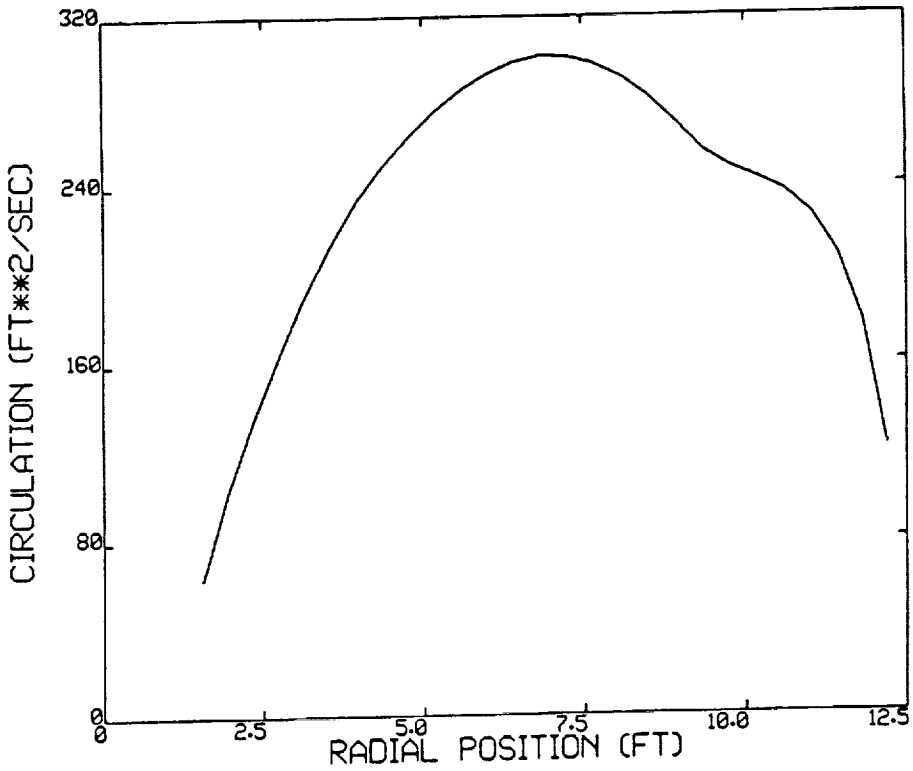


Figure 32. Circulation distribution of the ATB for $C_T = 0.0118$ .

weak sheet trailing inboard (or several filaments modelling the sheet). The XV-15 blade also shows a steep drop near the tip, indicating that a strong tip vortex will be trailed. The wake immediately inboard of the maximum bound circulation will again be relatively diffuse but the high twist inboard leads to a very strong root vortex.

Thus, the XV-15 rotor, in general, fits within what could be called the "conventional" framework of a discrete vortex model; a strong tip vortex with its strength determined by the bound circulation near the tip, combined with a sheet-like wake inboard, albeit with its strength concentrated closer to the root than in conventional designs. The ATB presents quite a different picture. The circulation distribution is far more similar to that of a fixed-wing aircraft than that of a typical helicopter; the taper of the blades causes the load to shift inboard. Although the gradient of the bound circulation is relatively steep very near the tip, it is readily apparent that the appropriateness of a model using a single tip filament is questionable. Same-sign vorticity is trailed from the 55% station out to the tip and this vorticity will roll up more slowly than the wake of a conventional rotor. Thus, the following blades will almost certainly "see" a more diffused wake trailing from the tip region than is assumed in conventional models.

The preferred method for dealing with this situation would be to use a large number of free filaments trailing from the tip region and allowing them to merge downstream. However, as discussed in Section 4.3, vortex amalgamation in three dimensions is difficult to handle within the context of this analysis and is in any case still a subject of research. Therefore, rather than resort to ad hoc merging procedures, it was resolved to keep the current wake structure assumptions. By trailing the tip filament from the centroid of the outermost circulation zone, and by employing a physically well-motivated vortex core model, the correct first-order effects of the rolling-up tip wake will be obtained.

It is interesting in this context to consider the change in the ATB circulation distribution shown for the moderate-thrust case of Figure 32 when the rotor is operated at high or low thrust. The relatively low-thrust case shown in Figure 33 displays an even more gradual fall-off in circulation strength, suggesting a stronger tendency to diffuse wakes in the tip region. However, the high-thrust case shown in Figure 34 shows a pronounced steepening of the bound circulation distribution near the tip. This abrupt drop-off at high thrust could lead to the formation of a strong, discrete tip vortex as envisioned in commonly-used models. This supposition is consistent with the tip vortices visualized in high-thrust ATB tests documented in Refs. 31 and 33.

The final result of performance predictions for the ATB is shown in Figure 35. The accuracy achieved is not quite as good as the results of the XV-15 runs shown previously, but it is nonetheless superior to that reported in Ref. 31 for simulations using prescribed wake models. The underprediction of Figure of Merit at high thrust is an issue already discussed in Ref 31, which suggested that the stall model implicit in two-

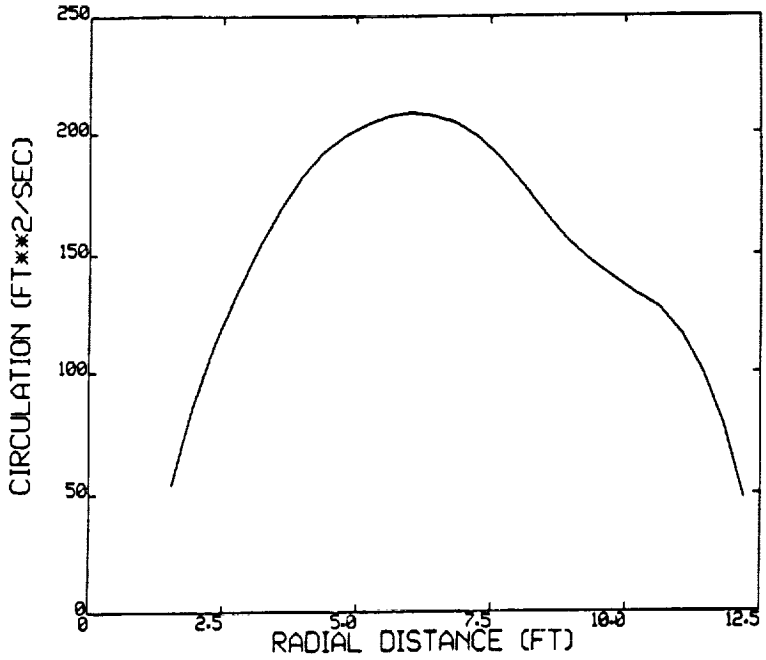


Figure 33. Circulation distribution of the ATB for $C_T = 0.0074$ .

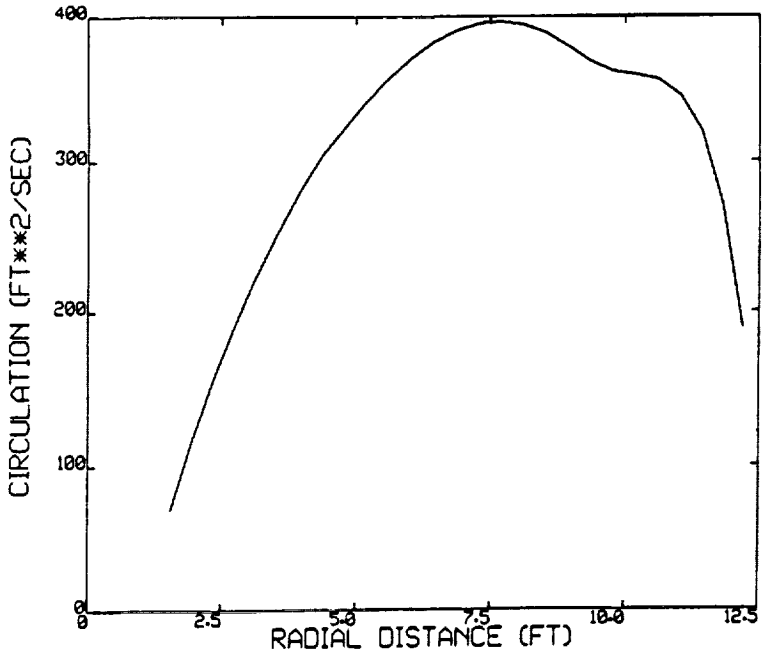


Figure 34. Circulation distribution of the ATB for $C_T = 0.0162$ .

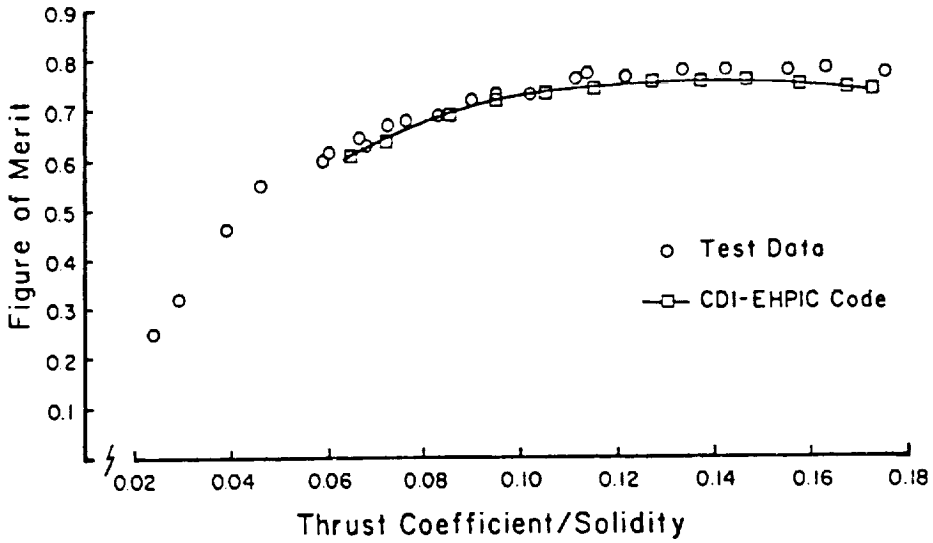


Figure 35. Performance predictions for the Advanced Technology Blade version of the XV-15 rotor (square tip variant).

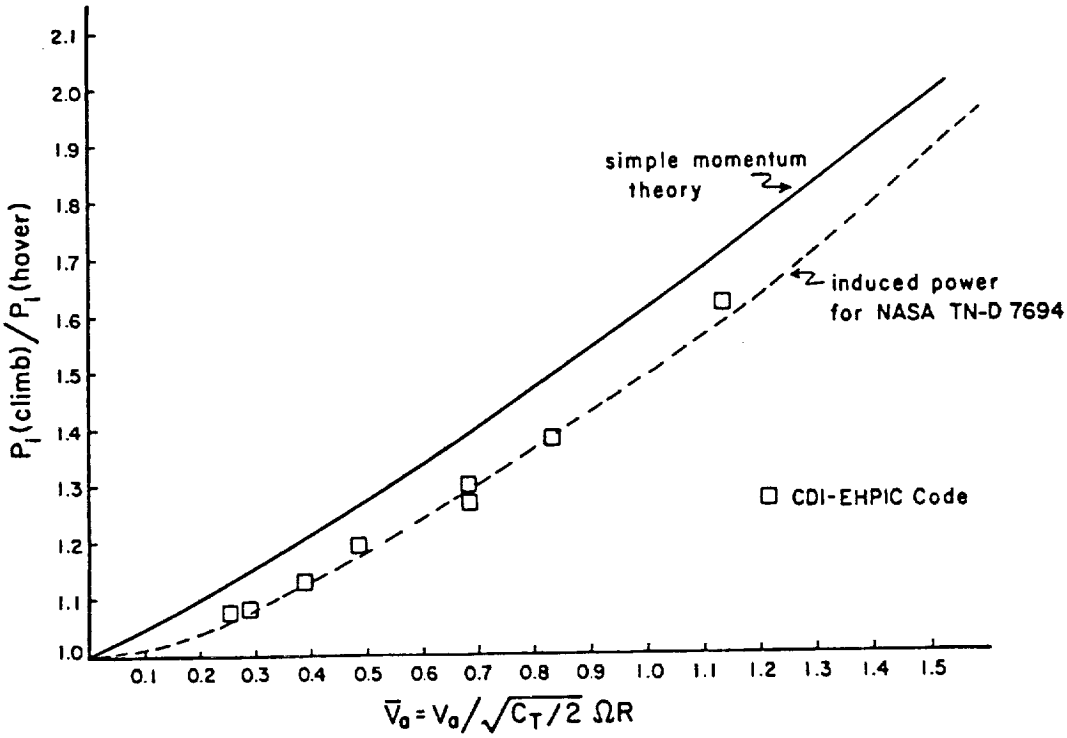


Figure 36. Ratio of induced power in climb to induced power in hover as a function of nondimensional climb rate. The faired data is for a two-bladed model rotor; predictions are made using the EHPIC code and simple momentum theory.

dimensional airfoil data may be inappropriate for use on such heavily loaded rotors which feature strong three-dimensional effects.

## 5.4 Rotor Performance Predictions in Climb

Traditionally, hover power predictions have been more of a concern to the rotorcraft community than climb performance. However, many recent military helicopter competitions (e.g., UTTAS, AAH and LHX) have featured stringent climb performance specifications which have stimulated interest in this topic. Reference 34 points out the inadequacy of the simple momentum theory methods often used to predict climb performance. Harris (Ref. 34) made this point in an analysis of performance data for an isolated tail rotor in lateral flight. By using a curve fit to remove profile power, Harris was able to show that the induced power consumed by a rotor in climb is substantially overpredicted by methods based on momentum theory.

To address this issue, the CDI-EHPIC hover code was applied to the prediction of the performance of the model tail rotor described in Ref. 35. The rotor used in these experiments was a two-bladed design with a radius of 0.64 m (2.1 ft) and a tip Mach number of 0.65. The blades were untwisted, had a constant chord of 0.053 m (0.17 ft) and used an NACA 0015 airfoil section across the entire span. As an initial check before undertaking simulations of climb, the hover performance of the model rotor was correlated. The induced power was predicted to within 1% over the entire range of collectives in the hover experiments.

Figure 36 shows the results of the simulated climb experiments of Ref. 35. The plots show the induced power consumed by the rotor in axial flight. Though there is no direct way of measuring induced power, its value in these experiments was calculated by subtracting an estimate of the profile power from the total power required, as shown in Ref. 34. For this purpose, the total power was assumed to consist of three components: a profile power contribution at zero thrust (which could be measured directly); an additional profile component proportional to the square of $C_T$ ; and an induced component proportional to $C_T^{3/2}$ . Curve fits for the latter two terms were obtained in hover using the assumption that profile power is invariant with climb. Thus, the induced power increment due to climb could be isolated.

As is evident from Figure 36, the calculated levels of induced power match the experimental results closely. (Note that the momentum theory prediction is uniquely determined by climb rate, while the EHPIC calculation depends on climb rate and collective. Thus, different power ratios are possible at a given climb rate.) Furthermore, both the experimental and computational results predict substantially lower levels of induced power than does the simple momentum theory approach. Reference 34 discussed similar results and concluded that the poor performance of momentum theory in predicting induced power near hover was attributable to the lack of an explicit representation of velocity induced by discrete vortex filaments passing near the blades; the assumption of uniform induced velocity in hover was judged to be inadequate for predicting trends in performance in the vicinity of hover.

Reference 36 outlines a method by which a prescribed wake code was modified to include the effects of climb. This modified code enjoyed more success in predicting induced power in climb but, of course, lacked the generality and breadth of applicability of free wake codes like the one developed here. This circumstance coupled with the accurate predictions of data cited above demonstrate that the CDI-EHPIC code is a superior tool for the prediction of performance in axial flight as well as in hover.

## 5.5 Prediction of Spanwise Load Distribution

The results above have focussed on the prediction of integrated performance quantities for rotors. While this is the primary interest of rotorcraft designers, it is also often important to examine the details of the load distribution on a blade. One source of data on this topic is the work of Cardonna and Tung (Ref. 37) which includes information on the spanwise load distribution of an untwisted, two-bladed rotor. This reference gives data on the loads measured by pressure taps at several spanwise stations on the model rotor. The pressures were integrated along the chord and are presented in Figures 37 and 38 along with the predictions given by CDI-EHPIC.

The two cases shown represent moderate- and high-thrust coefficient runs at a tip Mach number of 0.43. The rotor blades were untapered and had a radius of 1.14 m (3.75 ft) and an aspect ratio of 6.0. As is evident from Figures 37 and 38, the predictions capture the essential features of the local distribution along the span with good accuracy. The correlation achieved for these cases (which used thirty spanwise and two chordwise quads) is comparable to that achieved using a substantially more elaborate doublet-based lifting-surface method with ten chordwise panels (see Ref 37).

## 5.6 Rotor Wake Geometry

The sample calculations of rotor wake geometry shown in Section 3 can now be augmented by computations for actual rotors. Typical results for the rotor wake trajectories for high and low thrust are shown in Figures 39 and 40. Figure 39 shows the wake profile for an XV-15 operating at $C_T/\sigma = 0.057$ . As is evident, the filament trajectories are quite smooth as they descend into the far wake. Note also the very low initial descent rate of the tip vortex; the tip vortex in fact lies above the plane of the rotor disk until the first blade encounter. This result is further evidence of the EHPIC code's ability to successfully converge wakes with large numbers of filaments trailing from rotors with several blades. Even the presence of substantial blade/vortex interaction due to the low tip vortex descent rate does not impede convergence.

A similar plot for the same XV-15 rotor at $C_T/\sigma = 0.127$ is shown in Figure 40. The overall results are much the same as those for the lightly-loaded rotor described above, although two features are worthy of note. First, some distortion of the third filament out from the root is evident; this is a consequence of using a small number of free elements on the second

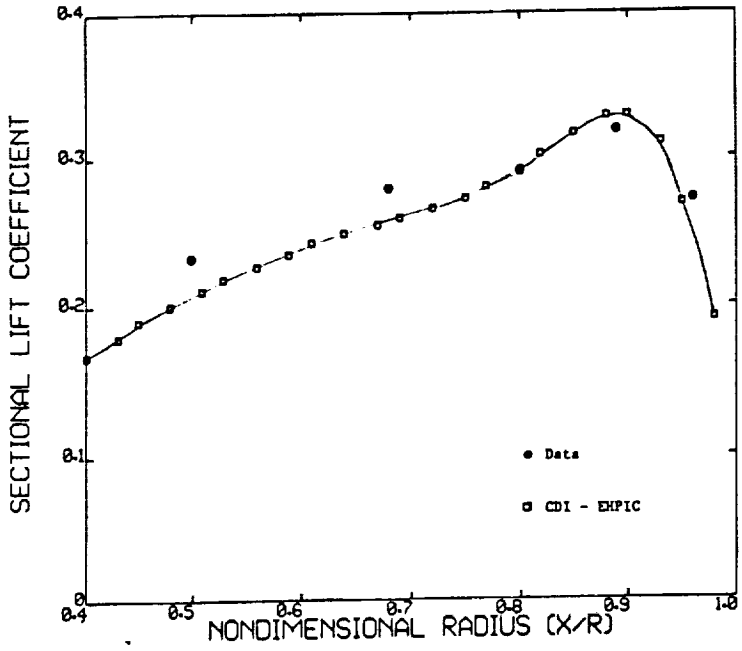


Figure 37. Spanwise distribution of lift for a two-bladed model rotor, $C_T = 0.0046$ .

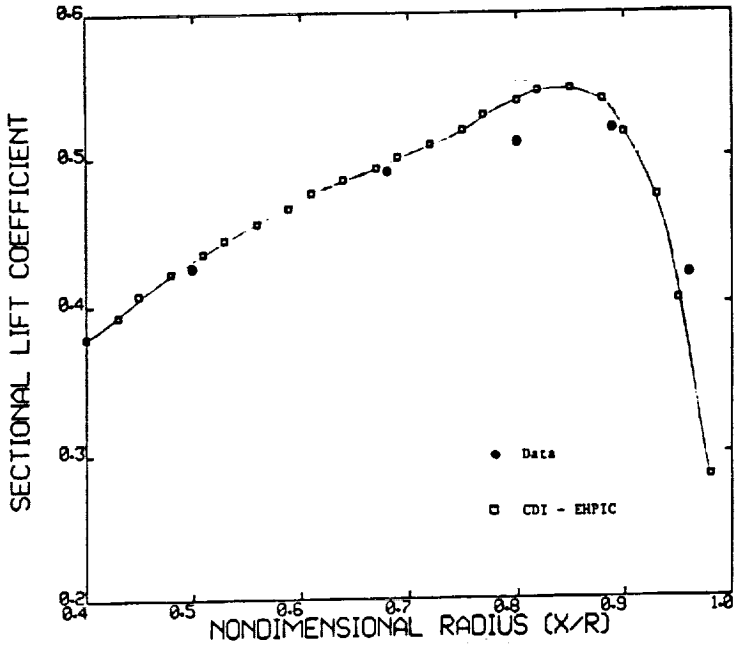


Figure 38. Spanwise distribution of lift for a two-bladed model rotor, $C_T = 0.0079$ .

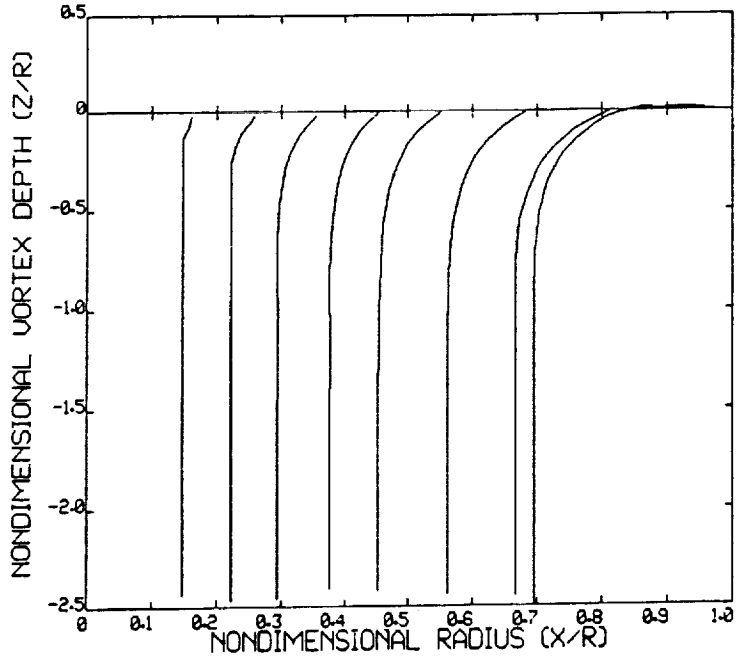


Figure 39. Wake geometry for the XV-15, $C_T$ = 0.0051

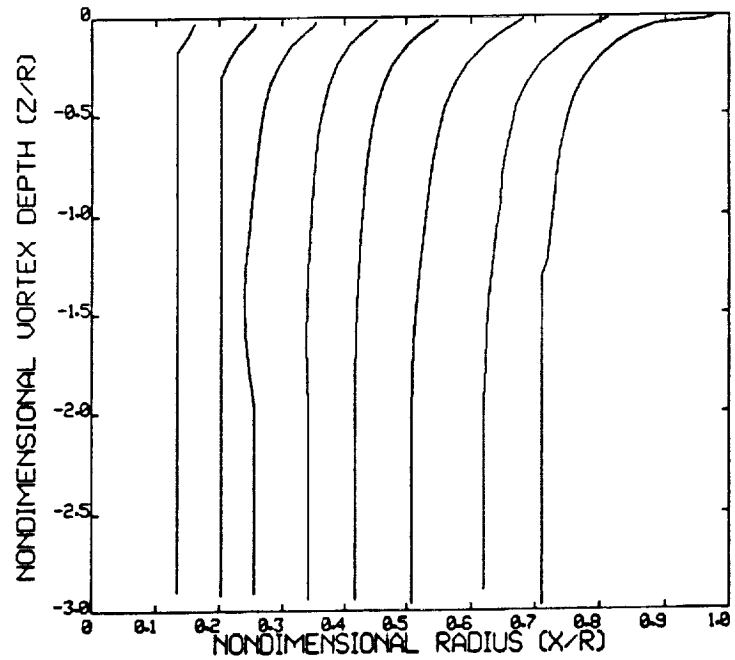


Figure 40. Wake geometry for the XV-15, $C_T$ = 0.0113

filament and could be remedied by increasing the number of free elements more smoothly from filament to filament near the root. Second, a kink is evident in the tip filament at the transition from the free wake to the prescribed wake. This small kink indicates that the calculated geometry of the prescribed wake (which is based on the momentum-theory treatment described in Section 1) is not quite consistent with the free wake spacing at the juncture point. The momentum-based treatment for the tip-vortex prescribed wake is an approximation that can be removed by explicitly tying the prescribed wake spacing to the spacing of the last points in the free wake. Such a technique has been used successfully in demonstration calculations but has not been included in the current version of EHPIC due to problems with obtaining uniformly reliable convergence with this method. This augmented free-wake/far-wake coupling is a strong candidate for inclusion in future versions of EHPIC.

For the moment, this free-wake/far-wake mismatch can be minimized by using a large number of free turns for the tip vortex. Moving the juncture to a distance of one rotor diameter below the disk (as recommended in Appendix C and in the EHPIC users manual) will keep any such kink small and will reduce its effect on the rotor inflow.

Along with the qualitative wake geometry information discussd above, some quantitative data on tip vortex trajectories are available. Comparisons to these data can be made for two of the rotors described in previous sections.

Figure 41 shows the predicted and computed tip vortex trajectory for the two-bladed rotor of Ref. 37 at $C_T = 0.0046$ . Both the computations and the data show the expected trend in axial displacement: relatively low descent rate until the first encounter with the following blade, after which the descent rate increases substantially. The simulation predicts the axial displacement well until the first encounter, when a slightly increased deviation becomes evident. The same can be said of the prediction of contraction shown in Figure 42.

Figure 43 and Figure 44 display similar information for the ATB rotor at a thrust coefficient of 0.0176. As noted in Ref. 31, a distinct tip vortex was visible at this high $C_T$ . Here the EHPIC code captures the major features of both the axial and radial displacements. In particular, the contraction is well predicted, even though the descent rate in the near wake is underpredicted. The appearance of some deviations of this nature is not surprising, given the performance mismatch for the high-thrust cases of the ATB discussed in Section 5.3. Unfortunately, no tip vortex position data were available for the many other cases and rotor configurations for which favorable performance correlations were achieved.

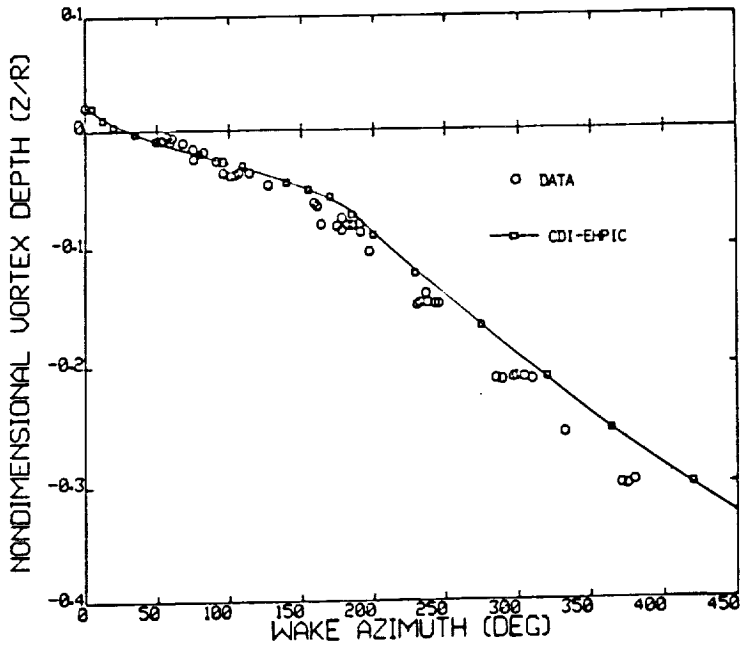


Figure 41. Tip vortex axial displacement for a two-bladed model rotor, $C_T = 0.0046$ .

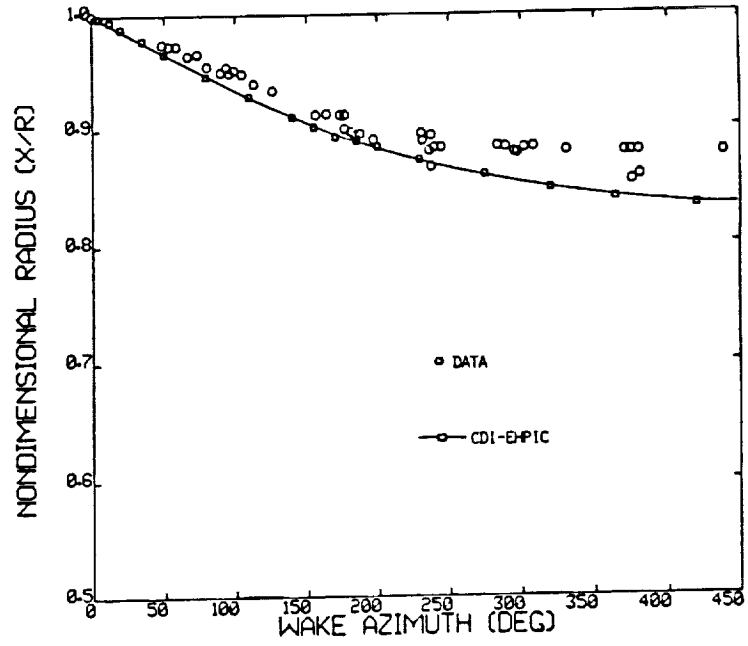


Figure 42. Tip vortex radial displacement for a two-bladed model rotor, $C_T = 0.0046$ .

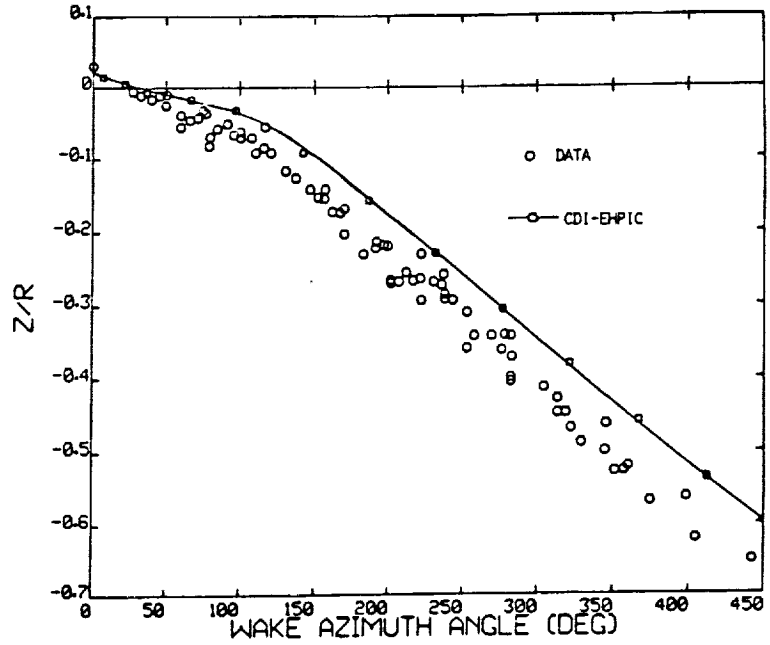


Figure 43. Tip vortex axial displacement for the ATB rotor, $C_T = 0.0176$ .

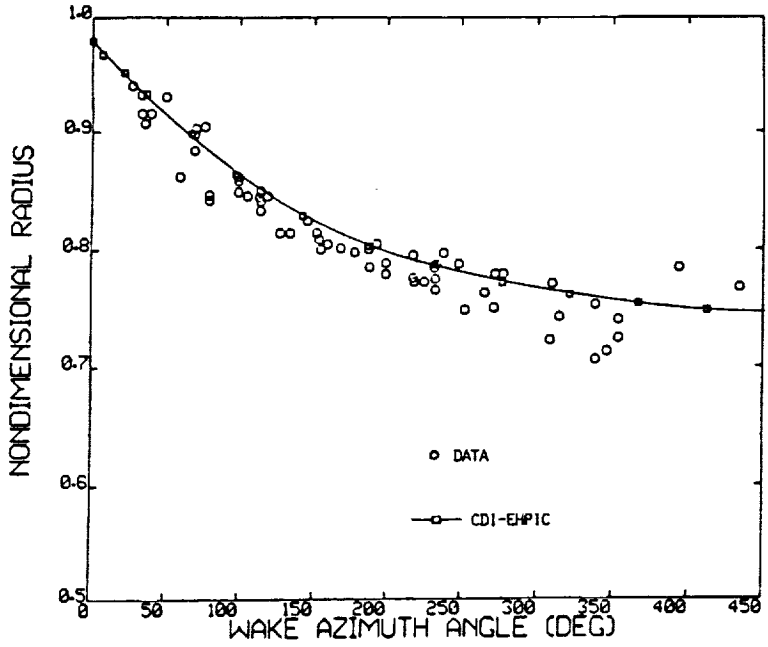


Figure 44. Tip vortex radial displacement for the ATB rotor, $C_T = 0.0176$ .

# 6. CONCLUSIONS

The development of the EHPIC code was an outgrowth of the initial work on the influence coefficient approach to free wake hover analysis described in Ref. 6. The major objective of this effort was to determine if the approach that was successful for the simplified rotor wakes analyzed in Ref. 6 could be extended to handle realistic rotor wakes and to provide reliable performance predictions for rotors in hover and axial flight.

As amply documented herein, this effort has been highly successful. The original model, which featured a single tip vortex trailing from each rotor blade, has been upgraded to include as many as eleven trailing filaments per blade. The wake geometry solution has been coupled to a vortex-lattice lifting-surface model of the blade that relaxes the bound circulation at the same time as the filament trajectories. This coupled relaxation has proven to be robust and flexible, having converged for a wide variety of rotor designs and operating conditions. Finally, the performance calculations undertaken using this free wake model have demonstrated close correlation with several rotors of widely differing design, including rotors for which only poor correlation had previously been obtained using prescribed wake models.

In the process of developing the EHPIC code, additional capabilities of the analysis emerged that made it even more useful and flexible than expected. For example, unlike previous Lagrangian free wake analyses, which featured a rigid coupling between the time step and the wake element length, the EHPIC code proved capable of handling filaments with variable arc size, a feature which allows selective refinement of the wake model in regions requiring high resolution (e.g., near rotor blades). Also, the ability of the code to step directly from solutions at a specified collective to nearby solutions at different collectives proved to be a valuable feature; since relaxation from scratch was not required for every point on a performance curve, "performance sweeps" could be carried out to rapidly fill in an entire curve.

Several features of the EHPIC code could benefit from additional refinement in future development. The computational efficiency of the routine could be enhanced by more systematic use of approximations for curved elements in the far field. A refined far wake model could be implemented to remove the small kinks that occur at the free wake/far wake junction in some operating conditions. Also, the roll-up of the tip vortex and the inboard filaments could be modelled in more detail, with more attention to the sheet-like structure that may be present in some cases, as well as to the effect of incomplete roll-up of the tip vortex on following blades.

Finally, as noted in Section 5, it would be desirable to account for airfoil lift stall explicitly in the performance calculation and eliminate the use of unrealistically high sectional lift coefficients. Although no major problems were observed in this regard in the sample calculations undertaken here, this would remove a potential source of future difficulties.

Even without these refinements, however, the EHPIC code represents a major new development in rotary-wing aerodynamics. Its novel approach to the calculation of the free vortex wakes of hovering rotors has been successfully applied to the prediction of the performance of a wide variety of designs. The results documented in this report have shown it to be a flexible, accurate, and practical tool for the analysis of advanced rotorcraft.

REFERENCES


1. Landgrebe, A. J.: An Analytical and Experimental Investigation of Helicopter Rotor Hover Performance and Wake Geometry Characteristics. USAAMRDL-TR-71-24, June 1971.

2. Scully, M. P.: Computation of Helicopter Rotor Wake Geometry and its Influence on Rotor Harmonic Airloads. Ph.D. Thesis, M.I.T., 1975.

3. Clark, D. R.; and Leiper, A. C.: The Free Wake Analysis: A Method for the Prediction of Helicopter Rotor Hovering Performance. JAHS, vol. 15, no. 1, 1970, pp. 3-11.

4. Saberi, H. A.: Analytical Model of Rotor Wake Aerodynamics in Ground Effect. NASA CR-166533, 1983.

5. Bliss, D. B.; Quackenbush, T. R.; and Bilanin, A. J.: A New Methodology for Helicopter Free Wake Analyses. Paper No. A-83-39-75-0000 presented at the 39th Annual Forum of the American Helicopter Society, May 1983.

6. Bliss, D. B.; Wachspress, D. A.; and Quackenbush, T. R.: A New Approach to the Free Wake Problem for Hovering Rotors. Proceedings of the 41st Annual Forum of the American Helicopter Society, May 1985, pp. 463-477.

7. Bliss, D. B.; Teske, M. E.; and Quackenbush, T. R.: A New Methodology for Free Wake Analyses Using Curved Vortex Elements. NASA CR-3958, 1987.

8. Vortex-Lattice Utilization in Aeronautical Engineering and Aircraft Design. NASA SP-405, 1976.

9. Hess, J. L.; and Smith, A. M. O.: Calculation of Potential Flow About Arbitrary Bodies. Progress in Aeronautical Sciences, vol. 8, 1967, pp. 1-138.

10. Johnson, F. T.; and Rubbert, P. E.: Advanced Panel-Type Influence Coefficient Methods Applied to Subsonic Flows. AIAA Paper 75-50, Jan. 1975.

11. Maskew, B.: Numerical Lifting Surface Methods for Calculating the Potential Flow About Wings and Wing-Bodies of Arbitrary Geometry. Ph.D. Thesis, Loughborough University of Technology, Oct. 1972.

12. Maskew, B.: Prediction of Subsonic Aerodynamic Characteristics: A Case for Low-Order Panel Methods. J. Aircraft, vol. 19, no. 2, 1982, pp. 157-163.

13. Tulinius, J. R.: Theoretical Prediction of Thick Wing and Pylon-Fuselage-Fanpod-Nacelle Aerodynamic Characteristics at Subcritical Speeds. NASA CR-137578, 1974.

14. Kocurek, J. D.; and Tangler, J. L.: A Prescribed Wake Lifting Surface Hover Performance Analysis. JAHS, vol. 22, no. 1, 1977, pp. 24-35.

15. Summa, J. M.; and Clark, D. R.: A Lifting-Surface Method for Hover/Climb Airloads. Preprint No. 79-3, 35th Annual Forum of the American Helicopter Society, May 1979.

16. Summa, J. M.; and Maskew, B.: New Methods for the Calculation of Hover Airloads. Paper No. 15, Fifth European Rotorcraft and Powered Lift Aircraft Forum, Sept. 1979.

17. Falkner, V. M.: Calculation of Aerodynamic Loading on Surfaces of Any Shape. Great Britain Aeronautical Research Council R&M 1910, 1943.

18. Bliss, D. B.; and Miller, W. O.: Vortex Filament Calculations by Analytical Numerical Matching with Comparison to Other Methods. AIAA Paper 89-1962, presented at the AIAA 9th Computational Fluid Dynamics Conference, Buffalo, NY, June 1989.

19. Moore, D. W.: A Numerical Study of the Roll-Up of a Finite Vortex Sheet. J. Fluid Mechanics, vol. 63, pt. 2, 1974, pp. 225-235.

20. Gray, R. B.: An Aerodynamic Analysis of a Single-Bladed Rotor in Hovering and Low Speed Forward Flight as Determined from Smoke Studies of the Vorticity Distribution in the Wake. Princeton University Aeronautical Engineering Dept. Report No. 356, 1956.

21. Bilanin, A. J.; and Donaldson, C. duP.: Estimation of Velocities and Roll-Up in Aircraft Vortex Wakes. J. Aircraft, vol. 12, no. 7, 1975, pp 578-585.

22. Betz, A.: Behavior of Vortex Systems. NACA TM-713, 1933.

23. Batchelor, G. K.: An Introduction to Fluid Dynamics. Cambridge University Press, 1967.

24. Bliss, D. B.: Prediction of Tip Vortex Self-Induced Motion Parameters in Terms of Rotor Blade Loading. Proceedings of the American Helicopter Society National Specialists' Meeting in Aerodynamics and Aeroacoustics, Feb. 1987.

25. Kocurek, J. D.: A Lifting Surface Performance Analysis with Circulation Coupled Wake for Advanced Configuration Hovering Rotors. Ph.D. Thesis, Texas A&M University, May 1978.

26. Carpenter, P. J.: Lift and Profile-Drag Characteristics of an NACA 0012 Airfoil Section as Derived from Measured Helicopter-Rotor Hovering Performance. NACA TN-4357, Sept. 1958.

27. Johnson, W.: Helicopter Theory. Princeton University Press, 1980.

28. Carpenter, P. J.: Effects of Compressibility on the Performance of Two Full-Scale Helicopter Rotors. NACA TN-2277, 1952.

29. Kocurek, J. D.; Harris, F. D.; and Berkowitz, L. F.: Hover Performance Methodology at Bell Helicopter Textron. 36th American Helicopter Society Forum, Washington, DC, May 1980.

30. Rosenstein, H.; and Wiesner, R.: Whirl Tower Investigation of the UH-61A Elliptical Tip Main Rotor, Boeing Vertol Co. Report No. D210-11128-1, Sept. 1976.

31. Felker, F. F.; Maisel, M. D.; and Betzina, M. D.: Full-Scale Tilt-Rotor Hover Performance. JAHS, vol. 31, no. 2, 1986, pp. 10-18.

32. Felker, F. F.; Betzina, M. D.; and Signor, D. B.: Performance and Loads Data from a Hover Test of a Full-Scale XV-15 Rotor. NASA TM-86833, 1985.

33. Felker, F. F.; Young, L. A.; and Signor, D. B.: Performance and Loads Data from a Hover Test of a Full-Scale Advanced Technology XV-15 Rotor. NASA TM-86854, 1986.

34. Harris, F. D.: Rotor Wing Aerodynamics: Historical Perspectives and Important Issues. Proceedings of the American Helicopter Society National Specialists' Meeting on Aerodynamics and Aeroacoustics, Feb. 1987.

35. Yeager, W. T., Jr.; Young, W. H., Jr.; and Mantay, W. R.: A Wind Tunnel Investigation of Parameters Affecting Helicopter Directional Control at Low Speeds in Ground Effect. NASA TN D-7694, 1974.

36. Moffitt, R. C.; and Sheehy, T. W.: Prediction of Helicopter Rotor Performance in Vertical Climb and Sideward Flight. Proceedings of the 33rd Annual Forum of the American Helicopter Society, May 1977.

37. Caradonna, F. X.; and Tung, C.: Experimental and Analytical Studies of a Model Helicopter Rotor in Hover. NASA TM-81232, Sept. 1981.

# APPENDIX A

## Model Problems

The implementation of the solution method discussed in the main text into a hover analysis computer program is a complex process with many interacting parts. To facilitate the understanding of this solution method, the results of two simpler model problems, drawn from Ref. 6, are discussed. The problems were chosen to have physical and mathematical behavior similar to that expected in the full hover analysis. The first of these problems is described in some detail to serve as an illustration of the general approach.

As a first model problem, a two-dimensional inviscid rotational flow problem was solved using the influence coefficient method. The problem, sketched in Figure A-1, involves the motion of two point vortices of the same sign and equal strength imbedded in a constant vorticity (solid body rotation) background flow, with the vorticity of opposite sign from the point vortices. If the vortices are positioned symmetrically on opposite sides of the axis of rotation and at the correct radial distance, they will remain stationary. In effect, this constitutes a steady self-preserving flow solution of the type described in Section 1.1. If this stationary configuration is disturbed, the vortices are unstable in the linear sense and propagate away. The nonlinear motion of the displaced vortices is known for this problem. The centroid of the point vortices, i.e., the point halfway between them, is convected in a circular motion by the solid body rotation background flow. At the same time, the two vortices rotate about their centroid at the rotation velocity they induce on each other. The net motion of the displaced vortices is also shown in Figure A-1.

This model problem was chosen because it has a steady self-preserving solution that is unstable, and because its source of nonlinearity is the interaction between point vortices. In the closely spaced turns of a rotor wake in hover, the local interaction between adjacent vortices also appears nearly two-dimensional. In addition, the presence of the solid-body rotation background flow is loosely analogous to the swirling background flow in a coordinate frame rotating with the rotor blades.

In the model problem, the background flow induces swirl velocities $\Omega r_1$ and $\Omega r_2$ on the two point vortices, where $\Omega$ is the rotation rate, and $r_1$ and $r_2$ are the distances from the origin to two vortices. The vortices induce equal rotation velocities of magnitude $\Gamma/2\pi r_{12}$ on each other, where $r_{12}$ is the distance between the vortices. The vortices will be stationary when $r_1 = r_2$ and $\theta_1 = \theta_2+\pi$ as shown in Figure A-1. Then $r_{12} = 2r_1$, and for equilibrium to be satisfied $\Omega r_1 = \Gamma/2\pi r_{12}$. Therefore $r_1 = (\Gamma/4\pi\Omega)^{1/2}$ when the vortices are stationary.

To solve the problem by the influence coefficient method, the two velocity components induced on each vortex are first expressed in terms of their location in Cartesian coordinates.

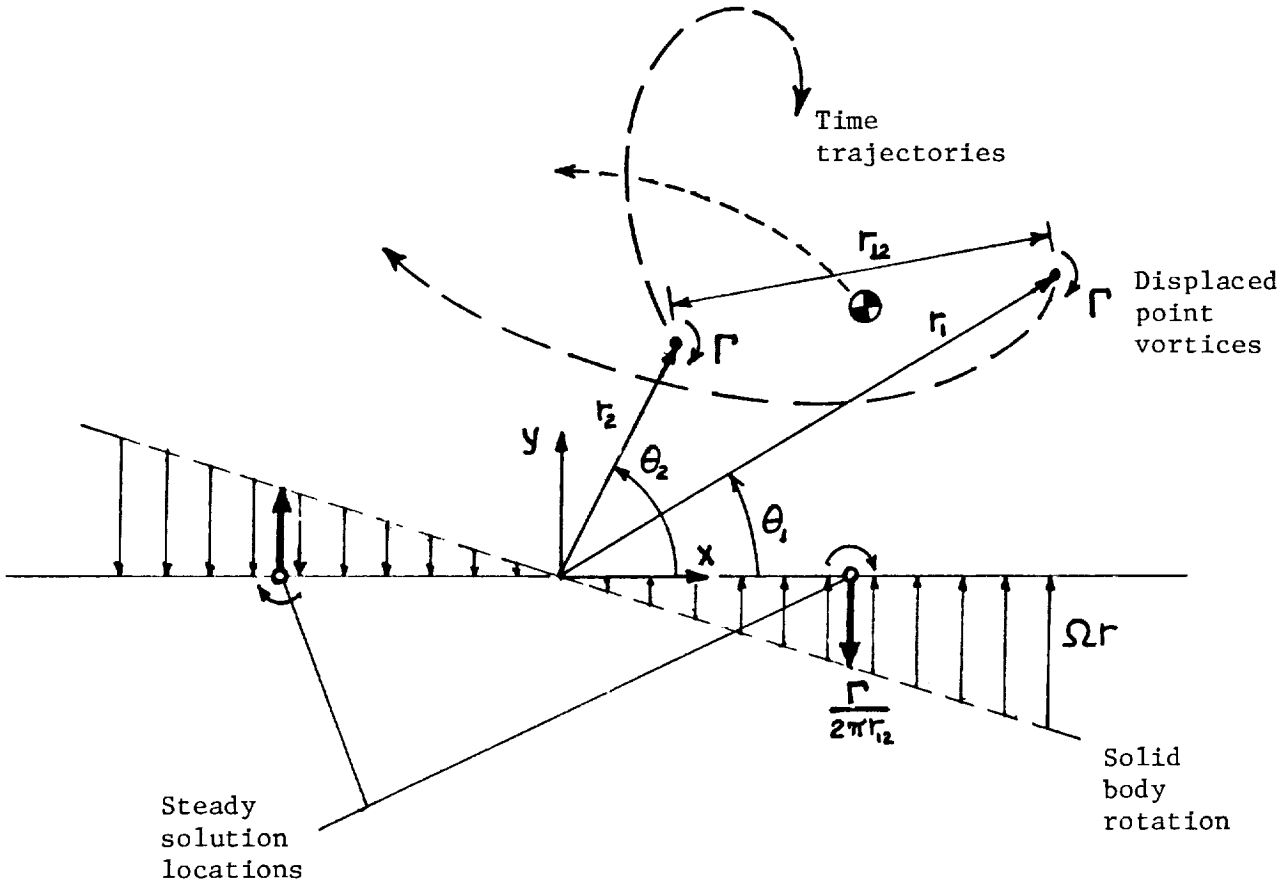


Figure A-1. Model problem involving two point vortices in a solid body rotation field.

$$
\begin{aligned}
u_1 &= U_1(x_1,y_1,x_2,y_2) = \frac{\Gamma}{2\pi}\frac{y_1 - y_2}{(x_1 - x_2)^2 + (y_1 - y_2)^2} - \Omega y_1 \\
v_1 &= V_1(x_1,y_1,x_2,y_2) = \frac{\Gamma}{2\pi}\frac{x_2 - x_1}{(x_1 - x_2)^2 + (y_1 - y_2)^2} + \Omega x_1 \\
u_2 &= U_2(x_1,y_1,x_2,y_2) = \frac{\Gamma}{2\pi}\frac{y_2 - y_1}{(x_1 - x_2)^2 + (y_1 - y_2)^2} - \Omega y_2 \\
v_2 &= V_2(x_1,y_2,x_2,y_2) = \frac{\Gamma}{2\pi}\frac{x_1 - x_2}{(x_1 - x_2)^2 + (y_1 - y_2)^2} + \Omega x_2
\end{aligned}
\tag{A-1}
$$

The effect on $u_1$ of small changes in $x_1, y_1, x_2$ and $y_2$ is then computed

$$
\Delta u_1 = \frac{\partial U_1}{\partial x_1}\Delta x_1 + \frac{\partial U_1}{\partial y_1}\Delta y_1 + \frac{\partial U_1}{\partial x_2}\Delta x_2 + \frac{\partial U_1}{\partial y_2}\Delta y_2 \tag{A-2}
$$

and likewise for the other velocity components. The derivatives serve as influence coefficients to relate changes in velocity to small changes in position, and can be calculated either analytically or numerically in the present simple problem. However, in more complex problems, such as the hover analysis, they must be calculated numerically, as is discussed in the main text.

Velocity vectors are now defined based on the velocity and position coordinates, and their incremental changes,

$$
\begin{aligned}
\vec{Q} &= (u_1, v_1, u_2, v_2) \quad , \quad \Delta\vec{Q} = (\Delta u_1, \Delta v_1, \Delta u_2, \Delta v_2) \\
\vec{D} &= (x_1, y_1, x_2, y_2) \quad , \quad \Delta\vec{D} = (\Delta x_1, \Delta y_1, \Delta x_2, \Delta y_2)
\end{aligned}
\tag{A-3}
$$

By, generalizing Eq. (A-2) to generate an influence coefficient matrix, $\tilde{C}$, the relation between velocity and displacement changes is given by

$$
\Delta\vec{Q} = \tilde{C}\Delta\vec{D} \tag{A-4}
$$

The velocity vector $\vec{Q}$ can be calculated from Eq. (A-1) for vortices located at $\vec{D}$. Then, the steady solution, can be obtained by finding the displacement of the vortices that cancels the velocity $\vec{Q}$, namely

$$\Delta\vec{Q} = -\vec{Q} \tag{A-5}$$

Then using Eq. (A-4)

$$\Delta\vec{D} = -\tilde{C}^{-1}\vec{Q} \tag{A-6}$$

If the problem were linear, this would give the position change required to reach the steady solution, i.e., the coordinates of the steady solution would be $\vec{D} + \Delta\vec{D}$. Since the problem is nonlinear, this process must be repeated several times to find the answer. Note that the coefficient matrix $\tilde{C}$ must be recomputed each time.

Using this method, and the desired solution was obtained after only a few repeated applications of the above procedure, even when the vortices were initially far from their equilibrium locations. Some examples of the solution sequence are shown in Figure A-2. Note that the positions of the vortices after each solution cycle are not related to their time dependent trajectories. These results demonstrate that the method does not require stability of the physical system to find the steady self-preserving solution.

The second model problem was intended to be a two-dimensional analog to the hover problem. Instead of helical tip vortices, a semi-infinite stack of vortex pairs was used to simulate the wake. This approach has the advantage of retaining the physical features of the real problem, although it is mathematically much simpler. The top vortex pair was held fixed to locate the wake and simulate the fixed tip vortex position at the blade. Below the top pair were six free vortex pairs to simulate the free wake. The tipping of crossflow planes, one at the location of each free vortex, was simulated artificially based on the change in position of successive vortices down the stack. The rotating frame velocity was simulated by a uniform stream normal to the wake cross-section. Below the last free vortex pair, was a regularly spaced, semi-infinite stack of vortex pairs to simulate the rest of the wake. The vertical location of this far wake, its width, and the spacing between successive pairs, were each constrained in various ways to study the solution procedure.

Again, it was possible to reach the answer by several repeated applications of the solution procedure, although the convergence process was more sensitive. Convergence was found to proceed in a more systematic manner when the first few solution cycles were used to gain fraction reductions in crossflow velocity. This was achieved by replacing Eq. (A-5)

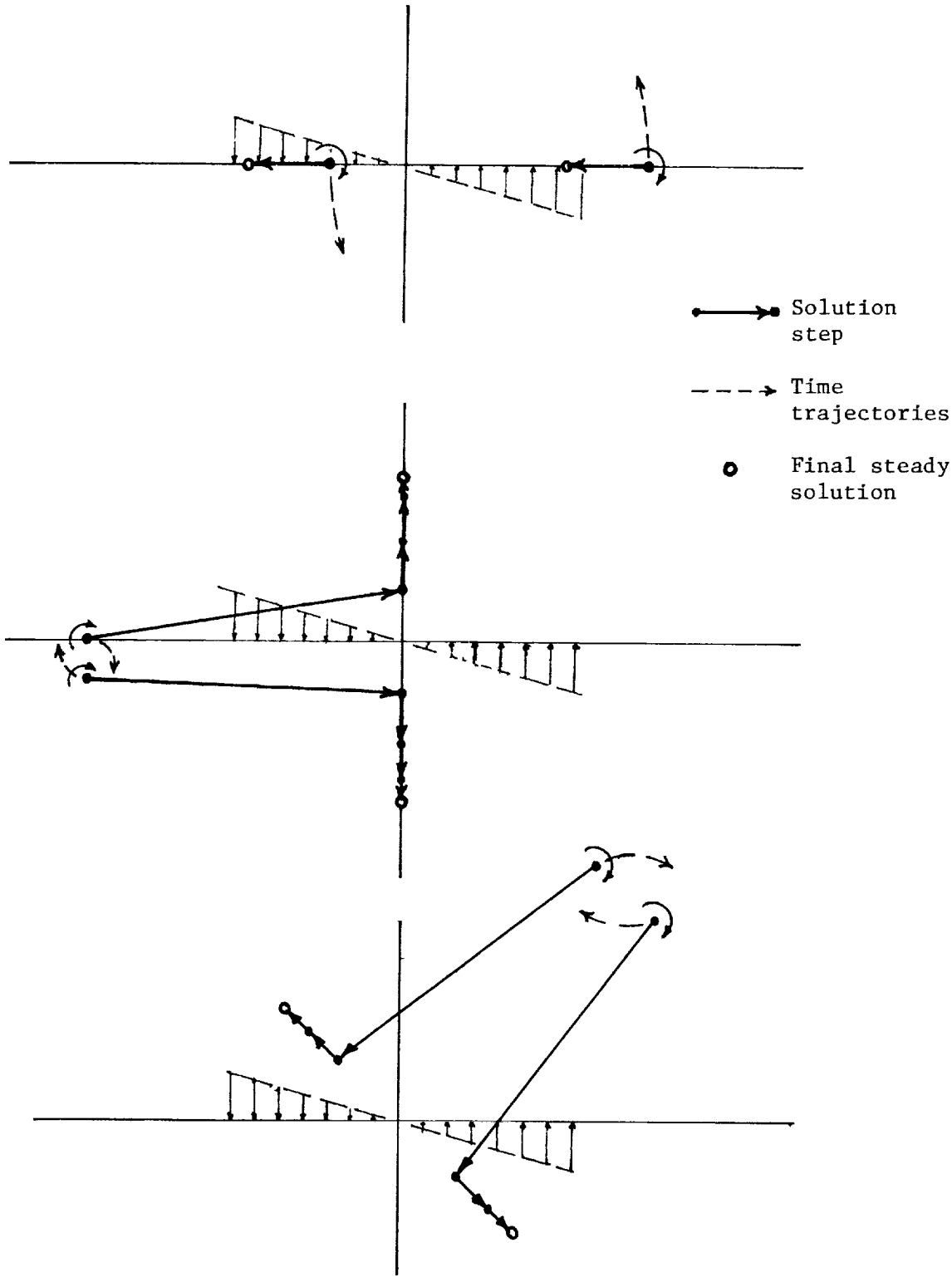


Figure A-2. Three solution sequences for the model problem involving two point vortices in a solid body flow. Each solution step represents an application of the influence coefficient solution procedure.

by $\Delta\dot{\vec{Q}} = -\alpha\dot{\vec{Q}}$ , where $\alpha < 1$ . This approach allows relaxation to the solution in smaller, more nearly linear steps. Converged solutions appeared qualitatively similar to a contracting rotor wake. However, the converged answer, and the convergence process itself, were both sensitive to the far wake model, particularly toward the bottom of the free wake. It was found to be better to let the far wake move and adjust with the bottom free wake pair, while still satisfying constraints on net momentum flux.

These two model problems illustrate the fundamentals of the influence coefficent relaxation method discussed in Section 1. The study of these problems in Ref. 6 provided a great deal of insight into modeling issues for the full hover analysis, including the importance of the far wake and the need to proceed carefully during the first few steps of the analysis to keep the vortex configuration linearly close to the previous solution. The solution procedures and modeling assumptions developed to attack these problems are still evident in the final hover analysis described in the main text.

## APPENDIX B

### Stability Analysis and Temporal Behavior

This appendix describes the results of a study of the stability of solutions found by the influence coefficient method. The linearized stability of converged solutions was analyzed and the temporal evolution of disturbances to these solutions was computed for the case of a single-bladed rotor with constant bound circulation.

The stability of small perturbations to a solution can be addressed analytically using the formulation in Section 1.4 once a converged solution has been obtained. The trajectories of filament displacements in the crossflow planes can be analyzed by solving an eigenvalue problem. The fact that the displaced filament is convected with the corresponding crossflow velocity can be written as

$$\Delta\vec{V}_n = \frac{d\Delta\vec{n}}{dt}$$

$$\Delta\vec{V}_b = \frac{d\Delta\vec{b}}{dt} \qquad \text{(B-1)}$$

where in this context the $\Delta$ denotes displacement from the converged solution. (Note that the blade bound circulation does not appear here or in the matrix equations below, since it is fixed in this demonstration calculation.) Using Eq. (B-1) with Eq. (6), and writing the result as a single matrix equation yields

$$\frac{d}{dt}\begin{pmatrix}\Delta\vec{n}\\ \hline \Delta\vec{b}\end{pmatrix} = \left[\begin{array}{c|c} \tilde{Q}_{nn} & \tilde{Q}_{nb} \\ \hline \tilde{Q}_{bn} & \tilde{Q}_{bb}\end{array}\right]\begin{pmatrix}\Delta\vec{n}\\ \hline \Delta\vec{b}\end{pmatrix} \qquad \text{(B-2)}$$

This form can be solved as a standard eigenvalue problem. Denoting the total displacement vector as $\vec{D}$ and the coefficient matrix as $\tilde{Q}_T$, Eq. (B-2) can be rewritten as

$$\frac{d\vec{D}}{dt} = \tilde{Q}_T\vec{D} \qquad \text{(B-3)}$$

Unless exceptional cases are encountered, the general solution will have the form

$$\vec{D} = \sum_{i=1}^{N} C_i \vec{\xi}_i e^{\lambda_i t} \qquad \text{(B-4)}$$

where the $\lambda_i$'s are the eigenvalues and the $\vec{\xi}_i$'s are the eigenvectors. The eigenvalues, which satisfy $|\tilde{Q}_T - \lambda_i \tilde{I}| = 0$, determine the stability of the system. The occurrence of eigenvalues with positive real parts indicates that the solution is unstable. The eigenvectors, which satisfy $(\tilde{Q}_T - \lambda_i \tilde{I})\vec{\xi} = 0$, determine the mode shapes of the filament motion in the crossflow planes.

The eigenvalue problem was solved numerically for the total influence coefficient matrix $\tilde{Q}_T$ determined from converged solutions. Note that $\tilde{Q}_T$ can be constructed readily from the influence coefficient matrix that arise in the normal solution procedure. A number of cases were analyzed for various values of $\Gamma$, R and $\Omega$, Table B-1 presents some representative results. The eigenvalues revealed several interesting features. Most of the eigenvalues were complex, and many had positive real parts, indicating numerous unstable modes. The time scale for almost all the eigenvalues was related to the rotor rotation speed, $\Omega$. Most of the eigenvalues were extremely insensitive to changes in $\Gamma$ and R, but linearly dependent on $\Omega$. This means the eigenvalues scale with $\Gamma/h_f^2$, where $h_f$ is the final spacing between turns. Using momentum theory, the quantity $\Gamma/h_f^2$ can be shown to depend only on $\Omega$. The evidence suggests that the wake instability arises primarily because of the local interaction between adjacent turns, since $h_f$ is the appropriate length scale in this case.

The above results can be interpreted in terms of the stability of an ideal infinite helix studied by Widnall.[B-1] Three types of helix instabilities were identified, one being associated with a fairly local interaction between distortions in adjacent turns. In a stationary reference frame, such as Widnall used, these distortions wrap around the mean helix position and amplify. Figure B-1 shows a typical instability of this type. These disturbances do not undergo significant propagation along the helix. However, if the same process is viewed in a rotating frame sweeping past the disturbances, as is used in the present hover analysis, the wrapping around of distortions would appear as an oscillatory, or orbiting, motion when seen in the crossflow planes. This explains why complex eigenvalues were obtained. Furthermore, if Widnall's results are renormalized, it is apparent that many of the instability modes really scale with $\Gamma/h_f^2$ (Ref. B-1 normalized results with $\Gamma/R^2$). Three considerations suggest that the hovering rotor wake instability is very closely related to the instability of an ideal infinite helix.

A numerical calculation of the wake motion using a time marching scheme was also performed. A nearly converged solution was allowed to evolve in

TABLE B-1

Eigenvalues of a Total Influence Coefficient Matrix for
Two Runs with Thrust Coefficient Held Constant

| Rotation Speed = 31.8 rad/sec<br>Thrust Coefficient = 0.0029 | | Rotation Speed = 15.9 rad/sec<br>Thrust Coefficient = 0.0029 | |
|---|---|---|---|
| Eigenvalues<br>Real Part | Imag Part | Eigenvalues<br>Real Part | Imag Part |
| 6.568 | 61.763 | 3.289 | 30.948 |
| 6.568 | -61.763 | 3.289 | -30.948 |
| 3.194 | 62.912 | 1.609 | 31.375 |
| 3.194 | -62.912 | 1.609 | -31.375 |
| -4.995 | 62.248 | -0.578 | 31.465 |
| -4.995 | -62.248 | -0.578 | -31.465 |
| -1.767 | 63.017 | -2.500 | 31.097 |
| -1.167 | -63.017 | -2.500 | -31.097 |
| 5.864 | 59.674 | 2.962 | 29.854 |
| 5.864 | -59.674 | 2.962 | -29.854 |
| -4.953 | 59.327 | -2.436 | 29.643 |
| -4.953 | -59.327 | -2.436 | -29.643 |
| 2.896 | 56.583 | 1.374 | 28.256 |
| 2.896 | -56.583 | 1.374 | -28.256 |
| -1.545 | 56.418 | -0.869 | 28.163 |
| -1.545 | -56.418 | -0.869 | -28.163 |
| 2.668 | 52.061 | 1.389 | 26.034 |
| 2.668 | -52.061 | 1.389 | -26.034 |
| -3.050 | 52.252 | -1.362 | 26.307 |
| -3.050 | -52.252 | -1.362 | -26.307 |
| 5.045 | 47.417 | 2.396 | 23.695 |
| 5.045 | -47.417 | 2.396 | -23.695 |
| -5.453 | 48.131 | -2.729 | 23.990 |
| -5.453 | -48.131 | -2.729 | -23.990 |
| 4.373 | 42.716 | 2.286 | 21.499 |
| 4.373 | -42.716 | 2.286 | -21.499 |
| -6.905 | 41.959 | -3.302 | 21.044 |
| -6.905 | -41.959 | -3.302 | -21.044 |
| 2.048 | 37.241 | 0.767 | 18.686 |
| 2.048 | -37.241 | 0.767 | -18.686 |
| -4.184 | 35.426 | -2.179 | 17.640 |
| -4.184 | -35.426 | -2.179 | -17.640 |
| 0.175 | 29.445 | -0.096 | 14.835 |
| 0.175 | -29.445 | -0.096 | -14.835 |
| -4.452 | 30.145 | -2.150 | 15.310 |
| -4.452 | -30.145 | -2.150 | -15.310 |
| 1.351 | 21.076 | 0.803 | 11.064 |
| 1.351 | -21.076 | 0.803 | -11.064 |
| -7.989 | 22.809 | -3.866 | 11.811 |

TABLE B-1 (Cont'd)

| Eigenvalues Real Part | Imag Part | Eigenvalues Real Part | Imag Part |
|---|---|---|---|
| -7.989 | -22.809 | -3.866 | -11.811 |
| 2.116 | 17.050 | 1.438 | 7.987 |
| 2.116 | -17.050 | 1.438 | -7.987 |
| -13.568 | 17.501 | -5.054 | 8.040 |
| 0.715 | 11.473 | -0.273 | 6.213 |
| 0.715 | -11.473 | -0.273 | -6.213 |
| -9.640 | 11.540 | -5.316 | 4.393 |
| -9.640 | -11.540 | -5.316 | -4.393 |
| -5.955 | 5.473 | -2.817 | 2.544 |
| -5.955 | -5.473 | -2.817 | -2.544 |
| -3.529 | 0.0 | -3.435 | 0.0 |
| -8.139 | 0.0 | -2.664 | 0.0 |

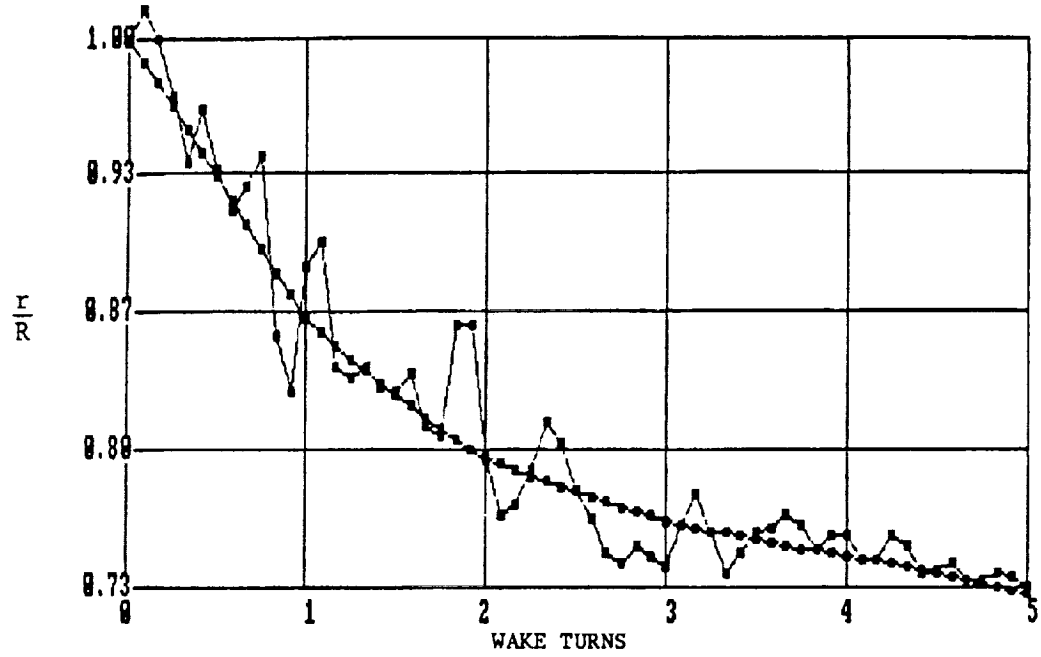


B-1a) Radial location versus number of turns.

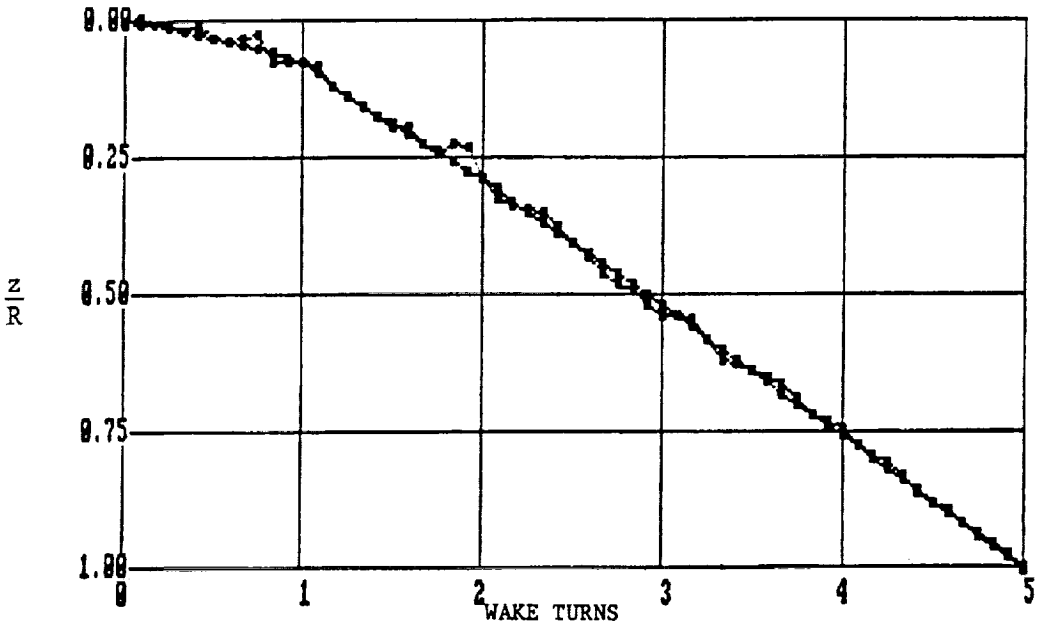


B-1b) Vertical location versus number of turns.

Figure B-1. Unsteady distortions of a five free wake turn, time stepping calculation for a one-blade rotor, $C_T = 0.0029$ . (Results obtained for two blade revolutions after the introduction of a small perturbation. Note vertical scale change between figures.)

time. The calculation was done in the rotating frame by following the time dependent motion of the vortex filament in the crossflow planes. This calculation is somewhat similar to the hover calculation described in Ref. 5, although a number of details are different. The wake motion did not converge to a steady solution. Instead, the tip vortex rapidly developed an instability. The resulting wake shape, after two blade revolutions (72 time steps) is shown in Figure B-1. Roughly speaking, the instability seems to have one or two predominant wavelengths per turn. This wavelength range corresponds to the case of the interaction between disturbances in adjacent turns. In the rotating frame, the strong convective effect of the rotating background flow sweeps these disturbances down the wake. Disturbances having one or two wavelengths per turn would have eigenfrequencies at one to two times the blade rotation rate. Unstable eigenvalues in this frequency range were among those computed in the stability analysis, as shown in Table B-1.

---

Reference:

B-1 Widnall, S.E.: "The Stability of Helical Vortex Filaments," J. Fluid Mechanics, Vol. 54, part 4, 1972, p. 641-663.

## APPENDIX C

### Choice of Computational Input Parameters

In making the correlation runs, it was necessary to select appropriate values for the major parameters of the model, i.e., the number of filaments, the numbers of free wake turns, the initial relaxation parameters (CTINIT and NRELAX), the overlap angle, the size of the wake elements, and the vortex-lattice spacing. The motivation for each of these choices is now outlined.

Number of Filaments - Section 5.2 shows that in representative cases the performance may be well approximated using a relatively small number of filaments, as along as the overlap treatment of the near wake is in place. The correlation runs presented in Section 5 used four trailing filaments in most cases. Representative cases for the rotors were checked using eight or nine free trailers. Comparisons to the four-filament results showed that the changes in predicted performance were sufficiently small to ignore for the purpose of carrying out the broad correlation study documented in Sections 5.3 to 5.5.

Number of Free-Wake Turns - In general, a conservative choice for the extent of the free wake is to use enough free turns to move the free-wake/prescribed-wake junction one rotor diameter below the disk for each filament. The number of turns required to fulfil this criterion will vary with the rotor thrust, but it is usually appropriate to use from two to four free turns on the inboard filaments and from three to five on the tip filament. As a rule of thumb, the tip filament free wake should have at least twice the azimuthal extent of the inboard filaments.

An exception may, in some cases, be made to this rule for the root vortex. It is acknowledged that the single root filament provides a very crude model of the inboard wake, but its presence is required because of the high circulation levels deposited in the wake in the root area. As discussed previously (and further documented in the CDI-EHPIC Users Manual) the root filament may exhibit instabilities if it is given a large number of free turns. Therefore, in many cases, the root filament has been restricted to half of a free turn. This treatment, although it differs from the manner in which the other inboard filaments are handled, improves convergence in many cases.

Initial Relaxation Parameters - The input parameter CTINIT governs the level of artificial climb downwash in the initial relaxation phase. NRELAX specifies the number of steps over which this climb velocity is decremented to the final climb rate. For most cases, it is appropriate to pick CTINIT to be roughly twice the estimated value of thrust coefficient for the rotor in question. Typically, NRELAX values of between 6 and 12 can be used: 6-10 for lightly-loaded rotors ($C_T/\sigma < 0.08$) and 10-12 for heavily-loaded configurations ($C_T/\sigma > 0.08$).

In those cases where short elements (15° or less) are used immediately downstream of the blade, it is sometimes necessary to use higher values of



C-2

CTINIT and NRELAX. In particular, for heavily-loaded, highly-twisted designs such as the XV-15 rotor, CTINIT should be closer to three times the estimated $C_T$ , while NRELAX should be 12-15. These are conservative choices and may even be increased if computational resources are not a problem. The initial relaxation need only be done two or three times (if that) to fill an entire performance curve; as noted in Section 5.1.4 above, "performance sweeps" can be done to rapidly obtain the rest of the curve.

Overlap Angle - The azimuthal extent of the overlap region should, in general, be kept between 7.5° and 15°. Higher values of overlap will introduce spurious results, since the curved trailers extended from the blade do not capture the contraction of the wake; large overlap angles exacerbate this problem. However, extremely small overlap angles require comparably sized free vortex elements immediately downstream of the blade; such very short elements (less than 7.5°) can be used, but they tend to contribute to slow convergence. In the runs performed in Section 5, as a general rule 15° of overlap was used for "conventional" rotors of modest twist and low loading, while the high-thrust, high-twist cases (such as the XV-15 and ATB) used 7.5°.

Size of the Wake Elements - The choice of the overlap region determines the size of the element immediately adjacent to the blade. Downstream of this point, arc sizes should be gradually increased to larger values as less detailed resolution of the flow is required. A typical pattern used in the correlation studies of Section 5 was to use two 15° elements immediately aft of the blade, followed by two 30° elements, then by fourteen 45° elements for a total of two turns of free near wake; adding on one or two additional turns of 60° elements usually provided a smooth transition to the far wake. To reiterate, the tip filaments typically require one or two more free turns than inboard filaments. At least three to five turns should be used on all filaments (except possibly the root vortex) unless computational constraints are serious.

Vortex-Lattice Spacing - The correlation runs of Section 5 typically used between 25 and 32 uniformly-spaced vortex quadrilaterals spanwise and a single chordwise quad. As with the number of free filaments chosen, checks were performed on representative cases using more refined meshes (as many as forty quads spanwise and five quads chordwise) to ensure that these calculations adequately represented the code's reproduction of thrust versus power curves. The current layout program allows essentially arbitrary spacing of the vortex quad edges. However, given that the convergence properties of arbitrarily spaced lattices are not well understood, it was resolved to rely on uniform meshes. Cosine spacing of the mesh edges can be used in the current program, but a program modification would be required to place the control points in a manner consistent with such spacing. Currently, as described in the user's manual, control points are located at the midpoints of the lattice quadrilaterals.

NASA
National Aeronautics and Space Administration

# Report Documentation Page

| 1. Report No. | 2. Government Accession No. | 3. Recipient's Catalog No. |
|---|---|---|
| NASA CR-4309 | | |

**4. Title and Subtitle**
Free Wake Analysis of Hover Performance Using a New Influence Coefficient Method

**5. Report Date**
July 1990

**6. Performing Organization Code**

**7. Author(s)**
Todd R. Quackenbush, Donald B. Bliss, Daniel A. Wachspress, and Ching Cho Ong

**8. Performing Organization Report No.**
A-90091

**10. Work Unit No.**
505-61-51

**9. Performing Organization Name and Address**
Continuum Dynamics, Inc.
P.O. Box 3073
Princeton, NJ 08543

**11. Contract or Grant No.**
NAS2-12148

**13. Type of Report and Period Covered**
Contractor Report

**12. Sponsoring Agency Name and Address**
National Aeronautics and Space Administration
Washington, DC 20546-0001

**14. Sponsoring Agency Code**

**15. Supplementary Notes**
Point of Contact: Fort Felker, Ames Research Center, MS T-042, Moffett Field, CA 94035-1000
(415) 604-6096 or FTS 464-6096

**16. Abstract**

A new approach to the prediction of helicopter rotor performance using a free wake analysis has been developed. This new method uses a relaxation process that does not suffer from the convergence problems associated with previous time-marching simulations. This wake relaxation procedure has been coupled to a vortex-lattice, lifting surface loads analysis to produce a novel, self-contained performance prediction code: EHPIC (Evaluation of Helicopter Performance using Influence Coefficients). The major technical features of the EHPIC code are described and a substantial amount of background information on the capabilities and proper operation of the code is supplied. Sample problems were undertaken to demonstrate the robustness and flexibility of the basic approach. Also, a performance correlation study was carried out to establish the breadth of applicability of the code, with very favorable results.

| 17. Key Words (Suggested by Author(s)) | 18. Distribution Statement |
|---|---|
| Influence coefficients<br>Free wake analysis<br>Rotorcraft hover performance | Unclassified-Unlimited<br><br>Subject Category - 02 |

| 19. Security Classif. (of this report) | 20. Security Classif. (of this page) | 21. No. of Pages | 22. Price |
|---|---|---|---|
| Unclassified | Unclassified | 102 | A05 |

NASA FORM 1626 OCT 86

For sale by the National Technical Information Service, Springfield, Virginia 22161

NASA-Langley, 1990